

Collective phenomena in blood suspensions

Dissertation

zur Erlangung des Grades
des Doktors der Naturwissenschaften
der Naturwissenschaftlich-Technischen Fakultät
der Universität des Saarlandes

Thèse

pour obtenir
le grade universitaire de docteur
Aix-Marseille Université
Spécialité : Mécanique et Physique des Fluides

von/présentée par

Revaz Chachanidze

Saarbrücken/Marseille
2018



Tag des Kolloquiums: 27.11.2018

| | |
|-----------------------|--|
| Dekan: | Prof. Dr. Guido Kickelbick |
| Vorsitzende/r: | Prof. Dr. Albrecht Ott |
| Berichterstatter/in: | Prof. Dr. Christian Wagner Prof. Dr. Thomas Podgorski |
| Akad. Mitarbeiter/in: | Dr. Emmanuel Terriac |
| Weitere Mitglieder: | Prof. Patrick Chabrand Prof. Élisabeth Lemaire Dr. Marc Leonetti |

Abstract

Abstract

This work was carried out in collaboration between I.R.P.H.E. (Institut de Recherche sur les Phénomènes Hors Équilibre), research unit of Aix-Marseille University and University of Saarland, Faculty of Experimental Physics (Naturwissenschaftlich-Technische Fakultät der Universität des Saarlandes) and aims to investigate microcirculatory hydrodynamics of blood *in vitro*. The study is dedicated to better understanding of complex collective phenomena that take place in microcirculation of blood through microfluidic *in vitro* experiments. It mainly focuses rigidity based margination in suspension of RBCs. For this purpose, model experiment was developed to examine margination caused exclusively by contrast of deformability between two sub-populations of RBCs.

Résumé

Ce travail a été réalisé dans l'I. R. P. H. E. (Institut de Recherche sur les Phénomènes Hors Équilibre), unité de recherche de l'Université d'Aix-Marseille en collaboration avec l'Université de la Sarre, la Faculté de Physique Expérimentale. Cette étude est consacrée à une meilleure compréhension de la microcirculation du sang *in vitro*, ainsi que des phénomènes collectifs qui prennent place dans la microcirculation. Il se concentre principalement sur la margination en fonction du contraste de rigidité dans une suspension de globules rouges. L'expérience modale a été développée pour étudier margination, causée exclusivement par le contraste de la déformabilité entre les deux sous-populations de globules rouges: les saines et les rigidifiées.

Kurzzusammenfassung

Diese Arbeit wurde durch die Zusammenarbeit zwischen dem I.R.P.H.E. (Institut de Recherche sur les Phénomènes Hors Équilibre), der Forschungseinheit der Aix-Marseille Universität und der Universität des Saarlandes, Fakultät für Experimentalphysik, ermöglicht und zielt auf die Erforschung der Mikrozirkulations-Hydrodynamik von Blut *in vitro*. Im Speziellen soll diese Studie dem besseren Verständnis komplexer, kollektiver Phänomene dienen, welche in der Mikrozirkulation von Blut in mikrofluiden *in vitro* Ex-

permiente entehen. Ein Hauptpunkt der Studie ist die steifigkeitsbedingte Margination in Suspensionen roter Blutzellen. Zu diesem Zweck wurde ein Modellversuch entwickelt, um die Margination zu untersuchen, welche lediglich durch den Unterschied der Verformbarkeit zwischen zwei Subpopulationen roter Blutzellen entsteht.

Acknowledgments

This thesis was completed thanks to the support of so many people. I consider myself immeasurably fortunate to live this experience. My PhD brought me to places and situations I never thought to find myself in when I started my work. It was a long road of learning and personal growth and I would like to thank all of those I've walked it with.

I would like to express my gratitude to my supervisors, Marc Leonetti and Christian Wagner. My work would have never been possible without your knowledge, support and patience. A student couldn't ask for better advisers. I would like also to thank Stephan Quint and Thomas John for fruitful discussions and their help.

I want to thank Patrick Chabrand, who was there for me since my first days in France. I would have never accomplished what I have without your help and for that you have my lifelong gratitude.

To all my friends, whom I met during these years, Viviana Claveria, Othmane Aouane, Zakaria Boujja, Alex Kihm, Stephan Quint, Rishab Handa, Javad Najafi, Oliver Köhn, François Yaya, Daniel Flormann, Emmanuel Terriac and so many others I extend my gratitude. I've learned a great deal from each and everyone of you and shared with you some of the best moments of my life.

Of course, I want to thank my officemates, Greta Simionato and Asena Abay. For the last two years, you girls have brightened my life.

And above all, I want to thank my parents, who through their sheer force of will and despite my defiant resistance, made me the person I am today. Whatever I have achieved, I hope I made you proud. I love you.

Contents

| | |
|--|------------|
| Abstract | ii |
| Acknowledgments | iii |
| List of figures | vii |
| 1 Introduction | 1 |
| 2 Background | 4 |
| 2.1 Blood: formed elements, plasma and main functions | 5 |
| 2.1.1 Red Blood Cells | 5 |
| 2.1.2 Membrane of red blood cell | 8 |
| 2.1.3 White Blood Cells | 10 |
| 2.1.4 Platelets | 10 |
| 2.1.5 Plasma | 11 |
| 2.2 Microcirculation and angioarchitecture | 11 |
| 2.2.1 Arterioles | 11 |
| 2.2.2 Capillaries | 12 |
| 2.2.3 Venules | 13 |
| 2.3 Microhemodynamics | 14 |
| 2.3.1 Basic information about flow in single microvessels. Poiseuille's law. | 14 |
| 2.3.2 Fåhræus effect | 16 |
| 2.3.3 Fåhræus-Lindqvist effect | 17 |
| 2.3.4 Hydrodynamics interaction of particles in flow. Origin of cross stream migration | 18 |
| 2.4 Margination | 22 |
| 3 Materials and methods | 28 |
| 3.1 Microfluidic fabrication | 29 |
| 3.2 Pressure driven flow | 31 |
| 3.3 Visualization | 32 |
| 3.3.1 Bright field microscopy | 33 |
| 3.3.2 Fluorescence microscopy | 33 |
| 3.3.3 Confocal microscopy | 33 |
| 3.4 Atomic force microscopy | 35 |
| 3.4.1 Cantilever choice | 36 |
| 3.4.2 Force-distance curves | 37 |
| 3.4.3 Experimental procedure | 39 |
| 4 Metrological development | 41 |

| | | |
|----------|--|-----------|
| 4.1 | Blood sample preparation | 42 |
| 4.2 | Rheology | 43 |
| 4.3 | Velocimetry | 46 |
| 4.4 | Image analysis in microfluidic experiments | 50 |
| 4.5 | Characterization of red blood cells with atomic force microscopy | 51 |
| 4.5.1 | Characterization of rigid cells | 51 |
| 4.5.2 | Characterization of healthy cells | 53 |
| 5 | Characterization of individual red blood cells at equilibrium state | 55 |
| 5.1 | Theoretical support | 57 |
| 5.2 | Experimental support | 59 |
| 5.2.1 | Confocal imaging | 59 |
| 5.2.2 | Manual classification | 60 |
| 5.2.3 | Image processing and Fourier analysis | 60 |
| 5.2.4 | Training of artificial neural network | 63 |
| 5.3 | Results of red blood cell shape classification by means of artificial neural network | 65 |
| 5.4 | Classification of red blood cells using self-organizing map | 66 |
| 5.5 | Results of unsupervised classification of red blood cell shapes | 69 |
| 6 | Margination of rigid red blood cells | 71 |
| 6.1 | Margination paths of rigidified red blood cells in different geometries | 72 |
| 6.1.1 | Theoretical background | 73 |
| 6.1.2 | Experimental setup | 74 |
| 6.1.3 | Results | 76 |
| 6.1.4 | Discussion | 78 |
| 6.2 | Dependence of margination on varying velocity and hematocrit | 79 |
| 6.2.1 | Experimental setup | 80 |
| 6.2.2 | Quantitative parameters of margination | 81 |
| 6.2.3 | Results | 83 |
| 6.2.4 | Discussion | 83 |
| 6.3 | Dependence of margination on the traveled distance at different hematocrits | 85 |
| 6.3.1 | Experimental setup | 85 |
| 6.3.2 | Results | 86 |
| 6.3.3 | Discussion | 87 |
| 6.4 | Comparison between experimental and numerical results | 88 |
| 6.4.1 | Numerical method | 89 |
| 6.4.2 | Data analysis in numerical simulations | 90 |
| 6.4.3 | Results | 92 |
| 6.4.4 | Discussion | 93 |
| | Conclusions | 99 |

| | |
|---|------------|
| Bibliography | 100 |
| Index | 115 |
| Notes | 115 |
| ANNEXES | 115 |
| A ANTON Paar MCR 702 rheometer low-torque resolution limit | 115 |

List of figures

| | | |
|------|---|----|
| 2.1 | Generic representation of blood elements. The image was adopted from Medical gallery of Blausen Medical 2014. | 6 |
| 2.2 | Examples of 3D reconstruction based on confocal imaging of 3 main RBCs shape types. The original confocal data was acquired by Greta Simionato and used for 3D reconstruction in this work with her kind permission. A Echinocyte. This abnormal RBC shape is characterized by numerous evenly spaced spicules. B Discocyte. A normal mature red blood cells of a biconcave disc-like shape. C Spherocyte. This abnormal RBCs if shaped as a sphere instead of a regular biconcave disc. D Stomatocyte. A cell loses its biconcave shape and acquires a bowl-like form. | 7 |
| 2.3 | The standard classification of RBC shape classes in use today. The picture adapted from Betticher, Reinhart, and Geiser 1995 | 7 |
| 2.4 | Schematic depiction of RBC membrane and its principal components. The image was adopted from Lux 2016 | 8 |
| 2.5 | A section of membrane which is curved in two planes. The image was adopted from Canham 1970 | 9 |
| 2.6 | Cross-sectional image of typical blood vessels using a relative composition of the vascular wall. Blood vessels are not represented at scale. Picture was taken from R. Greger, (auth.), P. D. R. Greger, et al. 1996 . | 12 |
| 2.7 | Schematic representation of endothelial glycocalyx and its main components. Picture was taken from Tuma, Durán, and Klaus Ley 2008 | 13 |
| 2.8 | Concept for the composition of the endothelial surface layer. The glycocalyx is the thin (50–100 nm) domain adjacent to the endothelial surface which is constituted by glycoproteins and proteoglycans bound directly to the plasma membrane. The main part of the endothelial surface layer (0.5 μm) consists of a complex array of soluble plasma components possibly including a variety of proteins, solubilized glycosaminoglycans, and hyaluronan.. Picture was taken from Tuma, Durán, and Klaus Ley 2008 | 14 |
| 2.9 | Microcirculation <i>in vivo</i> . The figure shows the blood flow through micrvesels in the rat mesentery with inner diameters 7, 12, and 16 μm (top to bottom) . Picture was taken from Tuma, Durán, and Klaus Ley 2008. | 15 |
| 2.10 | Graphical depiction of the tube hematocrit relative to feed hematocrit as a function of a capillary diameter that explains Fåhræus effect. Picture was taken from Tuma, Durán, and Klaus Ley 2008. | 16 |
| 2.11 | Change in relative apparent viscosity of RBC suspensions perfused through glass tubes as a result of Fåhræus-Lindqvist effect. Hematocrit level 45%. Inner diameters of glass tubes are between 3.3 μm and 1,978 μm . Picture was taken from Axel R. Pries, Neuhaus, and P. Gaehtgens 1992. | 18 |

| | |
|---|----|
| 2.12 Basic flow solutions. A Simple shear flow. B Couette flow (shear flow in the presence of a wall). C Poiseuille flow. | 20 |
| 2.13 Schematic representation of two opposite lateral forces acting on a rigid particle in the flow. Picture taken from Hwan Cho, M Godin, C.-H. Chen, et al. 2010 | 21 |
| 2.14 Stages of WBC recruitment. The top picture shows the four distinct adhesion steps that leukocytes must undergo to accumulate in a blood vessel. The bottom part of this image depicts predominant molecular determinants of this process. Picture is taken from Andrian and Mackay 2000. | 23 |
| 2.15 WBC margination in microcirculation. A Snapshot of marginating WBC in numerical simulation. Picture was taken from D. A. Fedosov and Gompper 2014. B Margination of WBC in pseudo two dimensional blood flow. | 24 |
| 3.1 Generic representation of the soft lithography procedure. On a silicon wafer (A) via spin-coating thin layer of photoresist gets applied (B). Through a photo mask, which is designed according to the required design, the coated wafer gets exposed to UV light causing polymerization of the coating. (C). Then, the excessive photoresist is removed by rinsing with a developing solution. This yields the silicon master for subsequent PDMS molding. D . Liquid mixture of silicon elastomer and curing agent needs to be poured on master E . After PDMS is solidified, it gets removed from the wafer. F Completing the fabrication of the microfluidic device, a cover glass is bonded to the PDMS substrate by means of plasma activation. | 30 |
| 3.2 The microfluidic design developed using Clewin software. The circle around the design defines the contour of the silicon wafer with 10 cm diameter. Straight 5 cm long channels highlighted by red rectangle were used for margination experiments. | 32 |
| 3.3 Schematic representation of optics in Yokogawa spinning disc. Image was adopted from Vesely 2007. | 34 |
| 3.4 Main components of atomic force microscope. | 35 |
| 3.5 Images of MLCT cantilevers used in this research. Images were adopted from official web-page of manufacturer (n.d.). | 37 |
| 3.6 Representative force-displacement curve of AFM measurements that was used for the sensitivity calibration of a cantilever. The curve was acquired as a result of interaction between cantilever tip and the ibidi Polymer Coverslip in air and illustrates various stages of AFM measurement. | 38 |
| 3.7 Examples for the conversion of photodetector signals (Volts) into forces (Newtons). Using the JPK data processing software, the position of the AFM head was converted into the position of the cantilever tip. The contact regime between the rigid surface of the dish and cantilever tip is represented by a vertical line, showing no indentation during approach. The curve is slightly tilted as a result of a calculation error (5 nm). | 40 |

-
- 4.1 The results of viscosity measurements of blood solutions at different hematocrits. Rheological measurements were performed for RBCs suspended in PBS. The grey area is the low-torque resolution limit of the ANTON Paar MCR 702 rheometer. The confidence intervals are evaluated for $(1 - \alpha) = 95\%$. 44
- 4.2 Comparison of the velocity profiles estimated for a Newtonian and a shear-thinning fluids in a $50 \mu\text{m}$ wide cylindrical channel. The results demonstrate that a suspension of *washed* RBCs even at 50% concentration shows very little deviation from the velocity profile of a Newtonian fluid 45
- 4.3 The results of viscosity measurements of blood suspensions at different hematocrits. Rheological measurements were performed for RBCs suspended in a media, composed of 65% PBS and 35% OptiPrep™. The grey area is the low-torque resolution limit of ANTON Paar MCR 702 rheometer. The confidence intervals are evaluated for $(1 - \alpha) = 95\%$. 46
- 4.4 Example of a velocity evaluation, $H_t=20\%$, $\Delta P=15$ mbars. **A** "Raw" data acquired via PTV across the section of a microfluidic channel. **B** Theoretical prediction of the velocity profile for water (viscosity $\mu=1 \text{ mPa} \cdot \text{s}$) in the channel of given geometry. **C** Experimental velocity profile which is numerically fitted using the underlying model. **D** Single curve fitting (middle plane, $z=15 \mu\text{m}$) 47
- 4.5 Evaluation of an optimal value for apparent viscosity μ_a as a fitting parameter by minimizing MSE, $H_t=20\%$, $\Delta P=15$ mbars. Figure demonstrates how viscosity is evaluated individually for different planes in Z direction from the bottom to the middle plane of microfluidic channel 48
- 4.6 The viscosity values along z direction obtained by minimization of MSE between measured and theoretical velocity. Example is given for the flow of RBC suspension of $H_t=20\%$ at $v_{\text{mean}} \approx 900 \mu\text{m/s}$. 48
- 4.7 Measured mean velocity of a blood suspension through a microfluidic chamber at different hematocrits. Cross-section of a microchannel $60 \mu\text{m} \times 30 \mu\text{m}$. Experimental data fitted according to linear law $v(\Delta P) = p_1 \cdot \Delta P$, assuming 0 velocity in the absence of driving pressure. 49
- 4.8 A generic representation of a RBC suspension flowing through a microchannel. **A** A bright field image of a blood solution of 10% hematocrit level flowing in $60 \mu\text{m}$ wide microchannel; exposure time 3 ms, scale bar $30 \mu\text{m}$. **B** Snapshot of numerical simulations showing margination of stiff RBCs in a rectangular duct channel. Normal red blood cells are omitted from the figure for clarity and as an analogy to experimental visuals. 50
- 4.9 Main steps in the image processing procedure, $H_t=10\%$, $\Delta P=12$ mbars ($v_{\text{mean}} \approx 600 \mu\text{m/s}$); the image was acquired in the middle plane of a $30 \mu\text{m}$ high microfluidic channel, scale bar $30 \mu\text{m}$. **(A)** The original image. **(B)** The cropped image after smoothing and subtracting background noise. **(C)** The image after erosion and mapping intensity values. **(D)** The binarized image used for cell detection. 51

| | | |
|------|--|----|
| 4.10 | Image of a RBC by means of atomic force microscopy. The cell was fixed in 1% of glutaraldehyde and immobilised on a substrate with an adhesive protein (Corning™ Cell-Tak, BD Biosciences). The image was taken in contact mode on the grid of 1024×1024 pixels over $9 \mu\text{m} \times 9 \mu\text{m}$ square area. | 52 |
| 4.11 | Result of AFM force mapping of a RBC rigidified in 1% glutaraldehyde. Data were acquired in PBS solution, the nominal spring constant of the cantilever is 0.6 N/m, the set-point force is 1 nN. A Set-point height. B Slopes of force-displacement curves | 52 |
| 4.12 | Force-distance curve illustrating the interacting force between cantilever tip and healthy RBC in PBS solution, the nominal spring constant of the cantilever is 0.01 N/m, the set-point force is 0.3 nN. | 53 |
| 4.13 | Results of AFM measurements demonstrate considerable contrast in rigidity between healthy RBCs and cells fixed in 0.1 – 1% of glutaraldehyde. | 54 |
| 5.1 | Schematic representation of an ANN and a single neuron. (A) Artificial neural network architecture. The K input layer neurons are fully interconnected with the L neurons from the hidden layer. While the input layer serves as buffer for input data only, hidden layer neurons perform the non-linear information processing via <i>tan</i> -sigmoid activation function. The hidden layer is fully connected with the linear output layer. (B) Single hidden layer neuron architecture. The activation function is bounded within a range of $(-1, 1)$. | 58 |
| 5.2 | Main shapes of RBCs, reconstructed from confocal images, and magnitudes of their corresponding 3D Fourier images. The spectra magnitudes are plotted in the Cartesian coordinate system, where the axes (u, v, q) are normalized spacial frequencies. A Echinocyte. B Discocyte. C Spherocyte. | 61 |
| 5.3 | Representative example of the spherical averaged 1D spectrum magnitude of the three RBC classes. Spherocytes (green) are radial symmetric and show a sinc-like behavior in the frequency domain with clearly pronounced maxima and minima. Discocytes (red) show a similar behaviour. However, due to their elliptic form, the spectrum is shifted towards higher frequencies compared to spherocytes. Echinocytes (blue) significantly differ from the other types. Their spiculated surface leads to a wide range of spectral components which slowly decreases. | 62 |
| 5.4 | Schematic representation of the idea behind spherical integration. Elements of the 3D matrix that have the same radius vector are coloured in yellow. As the size of a sphere increases the number of elements lying on its surface grows quadratically. | 63 |
| 5.5 | Histogram showing the number of data points in a lattice of the size $256 \times 256 \times 256 \text{ px}^3$ occurring at different radii. The histogram is plotted against radius vector values gridded over 256 points. | 63 |

| | | |
|------|--|----|
| 5.6 | Creation of a training data set elaborated on an dicsocyte. (A) FFT and applying high pass-filter to the Fourier image of a cell. (B) Spherical integration of a spectral magnitude (depicted in logarithmic scale). (C) Each new cell to be introduced to the ANN is positioned differently (slight rotations around axis) but our approach is robust against these rotations. (D) The obtained data-vector has a length of 256 and serves as an input for the ANN. | 64 |
| 5.7 | Training performance of the ANN with respect to the number of training epochs. | 66 |
| 5.8 | Classification of RBCs shapes using ANN. | 67 |
| 5.9 | Visual representation of a SOM. Each radial averaged spectrum is an input vector \mathbf{x}_i that is being broadcast into an array of neurons m_i . The weights of all neurons that are localised in the neighborhood N_i around the best matching one are updated together withing a training step. | 68 |
| 5.10 | Visual representation of the learning process. The euclidean distance between the weight vectors in the input space is represented in colour. As the system gets trained, neurons, initialized randomly, start to spread and cluster in the input space, responding to the similar stimuli. | 69 |
| 5.11 | Output of the SOM for automated cell shape classification. The SDE scale is represented in the form of 21 neurons. The SOM clusters input data without assigning values to the classes beforehand. A illustrates the histogram of neurons individual responses to a classified input data. Results withdrawn from this histogram are fitted with a smoothening function and normalized in order to create a probability density function depicted in B . Striped zones are the areas between first and fourth quantiles of the distributions. | 70 |
| 6.1 | Possible margination paths for leukocytes flowing with whole blood through channels with different cross-sections. The image was adopted from Yang, Forouzan, Burns, et al. 2011. (A) Circular cross section. (B) Slit-like channels, imitating 2D flow. (C) Rectangular channels. | 73 |
| 6.2 | Study of margination in microfluidic channels with rectangular cross-section. (A) General idea behind confocal imaging in microfluidics. In rectangular microfluidic channels, labeled RBCs were tracked in different planes along z axis by means of confocal microscopy. Further the data from different planes were assembled to reconstruct 3D distribution of rigidified cells. (B) Experimental setup. | 75 |
| 6.3 | Study of margination in glass capillaries. (A) General idea behind the original imaging technique. Directions of observation and flow in a capillary are co-oriented making the field of view orthogonal to the axis of symmetry. That allows us to detect rigid RBCs and obtain 3D distribution without confocal microscopy. (B) Experimental setup. (C) Image of the glass capillary extremity. Outer diameter 1 mm, inner diameter 50 μm . Scale bar 100 μm . (D) Example of the image obtained with our technique (scale bar 10 μm). The white outline designates the inner border of the glass capillary. | 76 |

-
- 6.4 Example of typical margination patterns in microchannels with different cross-sections. **(A)** Microchannels with high aspect ratio: to obtain pseudo-2D flow, $8\text{ }\mu\text{m}$ high and $60\text{ }\mu\text{m}$ wide channels were used. The distribution of rigidified RBCs was withdrawn from confocal image sequences. In this example distribution was not corrected by cells velocity and represents number of rigid RBCs passing per unit of cross section area. **(B)** Margination in a rectangular channels of $30\text{ }\mu\text{m}$ in height and $60\text{ }\mu\text{m}$ in width. **(C)** Distribution of rigidified cells in glass capillaries with inner diameter of $50\text{ }\mu\text{m}$. 77
- 6.5 The illustration of the general idea behind *Method B*. **A** A schematic representation of a microchannel cross-section. *Method B* allows us to calculate the density of rigid RBCs as a function of d . The stiff cells, passing through the cross-section in the rectangular region defined by d and the increment Δd are detected. The total number of cells that passed through this region, divided by its area, defines the density at a position d . The contribution of each cell to the result is corrected by the local velocity. The maximal number of steps (15) performed by the piezo limits the resolution in z to 16 different values of d . **(B)** The cross-sectional density of rigid RBCs estimated accordingly to *Method B*; the hematocrit $H_D=20\%$, mean flow velocity $v_{mean} \approx 900\text{ }\mu\text{m/s}$. 82
- 6.6 Effect of a varying velocity on the margination. The solid lines are Bezier curves and serve as eye-guides for the figure. The confidence intervals are evaluated for $(1 - \alpha) = 95\%$. **(A)** *Method A*. **(B)** *Method B*. **(C)** *Method C*. 84
- 6.7 Example of a 3D distribution of rigid RBCs passing through microfluidic channel. The hematocrit $H_D=20\%$, mean flow velocity $v_{mean} \approx 900\text{ }\mu\text{m/s}$. The distributions are corrected by the velocity field. **(A)** The entrance of a channel. **(B)** The distribution of rigid cells 5 cm away from the entrance. 86
- 6.8 The evolution of the margination alongside the microchannel at a different hematocrits. The confidence intervals are evaluated for $(1 - \alpha) = 95\%$ **(A)** Concentration of rigid RBCs in $8\mu\text{m} \times 8\mu\text{m}$ square zones in the corners of microfluidic device (*Method A*), d_s values are 2.54, 0.65 and 0.55 cm for H_D levels of 10, 20 and 40%, respectively. **(B)** The highest wall densities of rigid RBCs (*Method B*), d_s values are 2.65, 0.78 and 0.65 cm for H_D levels of 10, 20 and 40%, respectively. **(B)** The near wall concentration of stiff RBCs (*Method C*), d_s values are 2.72, 0.67 and 0.54 cm. 87
- 6.9 The evolution of margination alongside a microchannel at different velocities. The confidence intervals are evaluated for $(1 - \alpha) = 95\%$. **(A)** Concentration of rigid RBCs in $8\mu\text{m} \times 8\mu\text{m}$ square zones in the corners of microfluidic device (*Method B*), d_s values are 0.71, 0.65 and 1.12 cm for increasing v_{mean} . **(B)** The highest wall densities of rigid RBCs (*Method B*), d_s values are 1.31, 0.78 and 1.16 cm for H_D levels of 10, 20 and 40% respectively. **(B)** The near wall concentration of stiff RBCs (*Method C*), d_s values are 0.53, 0.67 and 1.31 cm. 88

| | |
|---|-----|
| 6.10 A suspension of RBCs flowing through a rectangular duct channel. The blue cells represent the rigidified red blood cells. The capillary number $Ca = 0.2$ and the volumetric fraction of the cells $\phi = 0.3$ (A) The initial configuration. (B) The stationary configuration. | 90 |
| 6.11 The density profiles of rigid RBCs at mean flow velocity in simulations . | 90 |
| 6.12 The density profiles of normal RBC at mean flow velocity in simulations. | 91 |
| 6.13 The intersection of density profiles of normal and rigid RBCs at 2.73% hematocrit level and mean flow velocity $v_{mean} \approx 2000 \mu\text{m/s}$. | 91 |
| 6.14 The margination of rigid cells in rectangular channels in experiments and numerical simulations. (A) The distribution of rigid RBCs at $H_D=20\%$ hematocrit, with the mean flow velocity of $v_{mean} \approx 900 \mu\text{m/s}$ in experiments. (B) The distribution of rigid RBCs at $H_T=20\%$ hematocrit, with the mean flow velocity of $v_{mean} \approx 1300 \mu\text{m/s}$ in simulations. (C) The distribution of rigid RBCs at $H_D=40\%$ hematocrit, with the mean flow velocity of $v_{mean} \approx 2850 \mu\text{m/s}$ in experiments. (D) The distribution of rigid RBCs at $H_T=40\%$ hematocrit, with the mean flow velocity of $v_{mean} \approx 500 \mu\text{m/s}$ in simulations. | 93 |
| 6.15 The evolution of margination obtained from numerical simulations at various hematocrit levels. As a characteristic parameter of margination we chose near wall concentration (<i>Method C</i>) | 94 |
| 6.16 Comparison between the experimental and the numerical results. Margination in experiments is measured for discharge hematocrit $H_D=20\%$ and the mean velocity of rigid cells $v_{mean}=897\pm33 \mu\text{m/s}$. The simulations were performed for tube hematocrit $H_T=21.97\%$ and the mean velocity of rigid cells $v_{mean}=1290 \mu\text{m/s}$. The margination values were obtained accordingly to (<i>Method C</i>) | 94 |
| .17 Measuring system CC20 | 116 |

1. Introduction

Introduction

Blood is a dense biological suspension. Around 40% to 50% of blood volume is represented by red blood cells (RBCs), 0.5-1% is formed by other suspended particles such as white blood cells (WBCs) and thrombocytes (platelets). The medium of the suspension is a Newtonian fluid called plasma. The rheological behaviour of blood is primarily determined by RBCs, whose main biological function is the maintenance of gas exchange in the body. The physiological importance of blood and the complexity of its rheological behaviour has been attracting researches to this field of study for decades.

Among many particular phenomena taking place in hemodynamics, it is margination that causes interest of researches in recent years. Margination can be described as the ability of certain suspended particles to travel from bulk flow to vessel wall. In blood, this phenomenon of cells segregation plays a crucial physiological role. It ensures the presence of leukocytes close to vascular endothelium which allows their adhesion and further migration to the inflammatory sites. Near-wall enrichment of platelets concentration is believed to be associated with fast blood clot formation and endothelial repair. Additionally, in case of certain diseases when mechanical properties of red blood cells were altered, those cells as well show the affinity of lateral migration in flow. Moreover, recent advances in targeted drug delivery arouse the interest in margination of drug carriers. The mechanisms leading to margination are not fully understood and very few experimental works have been performed, especially considering margination in 3D flow.

This thesis is organized as follows. A short overview of the state of the art about margination and the objectives of this work, including a theoretical explanation, are presented in the introduction. The second chapter is dedicated to general materials and methods, that were employed in the course of this study. The third chapter describes techniques designed in order to control experimental parameters of this study. The fourth chapter is dedicated to the several studies about rigidity based margination. In the fifth chapter we discuss an original method of analysing shapes of individual RBCs. The last chapter is dedicated to conclusions where we will summarize the results of this work.

Introduction

Le sang est une suspension biologique dense. Environ 40% à 50% du volume sanguin est représenté par les érythrocytes (ou globules rouges, RBCs), 0,5-1% est formé par les autres particules, tels que les leucocytes (ou globules blanches, WBCs) et les thrombocytes (plaquettes). Le milieu de la suspension est un liquide Newtonienne ap-

pelé plasma. Le comportement rhéologique du sang est principalement déterminée par les RBCs. Leur fonction biologique principale est de maintenir l'échange gazeuse dans le corps. La signification physiologique du sang et la complexité de son comportement rhéologique a attiré les chercheurs dans cet domaine pendant les décennies.

Parmi les nombreux phénomènes particuliers qu'on trouve dans l'hémodynamique, c'est la margination qui est dans le focus des chercheurs ces dernières années. La margination peut être défini comme l'abilité des certaines particules suspendues de traverser le flux vers les parois de canal. Dans l'hémodynamique ce phénomène est notamment important car il veille à la présence de globules blancs proche des parois vasculaires et permet leurs adhésion et migration aux sites inflammatoires. La concentration élevée des plaquettes aux parois vasculaires est associé avec la formation de thrombus et réparation endothéliale. En outre, dans le cas de certaines maladies lorsque les propriétés mécaniques des cellules rouges du sang ont été modifiés, ces cellules ainsi montrer l'affinité de la migration latérale dans l'écoulement. Ailleurs, le progrès récent dans le domaine de distribution des médicaments ciblés cause l'intérêt de la margination des vecteurs. Les mécanismes conduisant à la margination ne sont pas complètement compris et très peu de travaux expérimentaux ont été réalisés, surtout les études qui compte la margination dans l'écoulement 3D.

Ce manuscrit est composée de six chapitres distincts. Dans le premier chapitre est consacré nous allons présenter le support théorique et les connaissances actuelles sur la structure de microcirculation sanguine. Ici nous allons introduire les problèmes étudiés et formaliser les objectifs. Le second chapitre décrit les dispositifs expérimentaux et les méthodes générales utilisés dans cette étude. Dans le troisième chapitre nous allons présenter les techniques mises en œuvre dans ce travail pour contrôler les paramètres des expériences. Le quatrième chapitre décrit les plusieurs études de margination effectuées dans le cadre de ce thèse. La nouvelle méthode consacré à l'analyse des formes de globules rouges individuelles est présentée dans le cinquième chapitre. Enfin, les résultats de ce thèse sont résumés dans le dernier chapitre.

Einführung

Blut ist eine dichte biologische Suspension. Ungefähr zwischen 40 und 50 Prozent des Blutvolumens besteht aus roten Blutzellen und zwischen 0.5 bis einem Prozent besteht aus anderen Schwebstoffen, wie z.B. weiße Blutzellen und Blutplättchen. Das Medium der Suspension ist ein Newtonsches Fluid, welches als Plasma bezeichnet wird. Das rheologische Verhalten des Blutes wird zum Großteil durch die roten Blutzellen bestimmt, deren Hauptaufgabe im Blut die Aufrechterhaltung des Gasaustauschs des Körpers ist. Sowohl die physiologische Bedeutung als auch die Komplexität seines rheologischen Verhaltens lenkt die Aufmerksamkeit vieler Forscher seit Jahrzehnte auf dieses Forschungsgebiet.

Neben vielen anderen speziellen Phänomenen welche in der Hämodynamik auftreten ist es die Margination, welche das Interesse vieler Forscher in den letzten Jahren auf sich gezogen hat. Margination kann als die Fähigkeit von Schwebstoffen verstanden werden, aus dem Massenstrom zur Gefäßwand zu wandern. Im Blut spielt diese Auftrennung von Zellen eine entscheidende physiologische Rolle. Die Auftrennung sichert die Verfügbarkeit von Leukozyten in der Nähe des vaskulären Endothels, was deren Adhäsion und weitere Migration zu Entzündungen erlaubt. Man geht davon aus, dass die Anreicherung der Blutplättchen in der Nähe der Zellwand mit der schnellen Formation von Blutgerinnsel und der Reperatur von Endothelzellen zusammenhängt. Zusätzlich wurde festgestellt, dass bei manchen Krankheiten welche die mechanischen Eigenschaften roter Blutzellen verändern, diese Zellen auch eine Affinität für die seitliche Migration zum Fluss aufweisen. Außerdem haben jüngste Fortschritte in der gezielten Medikamenten-Lieferung zu einem Interesse in der Margination von Medikamenten-Lieferstoffen geführt. Die Mechanismen welche zu Margination führen sind nicht vollkommen verstanden, was wohl durch die geringe Anzahl der zu diesem Thema durchgeführten Experimente – vor allem bzgl. der Margination in 3D – zu erklären ist.

Diese Arbeit ist wie folgt aufgebaut: In der Einleitung werden sowohl ein kurzer Überblick und Ziele dargestellt, als auch eine Zusammenstellung aktueller Marginations-Studien und eine theoretische Erklärung der Physik welche in den Studien genutzt werden, gegeben. Das zweite Kapitel widmet sich allgemeinen Materialien und Methoden welche im Verlauf der Studie angewendet wurden. Im dritten Kapitel werden Techniken beschrieben, welche entwickelt wurden um experimentelle Parameter in dieser Studie zu kontrollieren. Das vierte Kapitel bezieht sich auf verschiedene Studien über die steifigkeitsbasierte Margination. Im fünften Kapitel werden wir die Analysemethoden verschiedener Formen einzelner roter Blutzellen diskutieren. Im letzten Kapitel fassen wir die Ergebnisse der Arbeit zusammen.

2. Background

In this chapter, general information about the subject of the thesis is provided. We discuss the composition of blood and the origins of its non-Newtonian rheological properties. A generic overview of all major blood components is given. We ascent especially the biophysics of RBCs. We briefly discuss mechanical properties of erythrocytes and composition of their cellular membrane.

Further we detail particularities of blood flow in microcirculation and highlight some of the most known and relevant to this work phenomena in this area. After that, we discuss hydrodynamic mechanisms of lateral migration of soft particles and cells in microfluidics. Lift forces acting on both rigid and deformable objects in low and zero Reynolds number flow, typical for microcirculation and microfluidics, are explained.

At the end of the chapter we discuss problem of margination. Current state-of-the-art in this research topic is described. Objectives and purpose of this work will be formulated.

Dans ce chapitre, nous introduirons des informations générales et relatives à ce sujet de thèse. Nous discuterons de la composition du sang ainsi que l'origine de ses propriétés rhéologiques non-Newtoniennes. Les principaux composants du sang seront décrits. Notamment, nous porterons notre attention sur les propriétés des globules rouges. Nous examinerons les propriétés mécaniques des érythrocytes et la composition de leur membrane cellulaire.

De plus, nous détaillerons les particularités liées à un écoulement de sang dans la microcirculation et nous mettrons en évidence les phénomènes les plus connus et pertinents pour ce travail. Les mécanismes hydrodynamiques de migration latérale des particules et cellules en microfluidique seront discutés dans ce chapitre. Nous nous intéresserons à la portance hydrodynamique agissant à la fois sur les particules rigides mais aussi sur celles qui sont déformables, pour de petits nombres de Reynolds, voire nuls, typiques de la microcirculation et de la microfluidique.

Enfin, nous nous attarderons sur le problème de margination. L'état de l'art de ce sujet de recherche sera décrit. Les objectifs et le but de ce travail seront formalisés.

In diesem Kapitel werden grundsätzliche Informationen zum Thema der Arbeit vorgestellt. So wird die Zusammensetzung von Blut und die Ursache seiner nichtnewtonschen rheologischen Eigenschaften erklärt. Weiter wird eine Übersicht über alle

relevanten Komponenten von Blut gegeben. Besonderes Augenmerk wird hierbei auf die biophysikalischen und mechanischen Eigenschaften von roten Blutkörperchen (lat. Erythrozyt) gelegt. Ferner wird die Zusammensetzung der Zellmembran solcher Erythrozyten kurz diskutiert. Weiterhin werden Besonderheiten des Blutflusses in Mikrozirkulation ausgearbeitet und es werden einige der geläufigsten und der für diese Arbeit relevantesten Phänomene hervorgehoben. Im Anschluss werden die hydrodynamischen Mechanismen lateraler Migration weicher Partikel und Zellen in mikrofluidischen Umgebungen diskutiert. Auftriebskräfte von starren und deformierbaren Objekten in Strömungen mit niedrigen und verschwindenden Reynolds-Zahlen, die typisch für Mikrozirkulation und Mikrofluidik sind, werden erklärt. Am Ende des Kapitels werden Probleme der Margination diskutiert und der aktuelle Stand der Forschung in diesem Gebiet kurz zusammengefasst und beschrieben. Im Anschluss werden die Zielsetzung und der Zweck dieser Arbeit formuliert.

2.1. Blood: formed elements, plasma and main functions

Blood is an essential part of connective tissue in humans and animals. This biological fluid is in fact a suspension which can be characterized by its structure (spatial organisation of cells) and its rheology. It is composed of erythrocytes (or RBCs), white blood cells (WBCs) and platelets (or thrombocytes) suspended in a Newtonian fluid called plasma.

2.1.1. Red Blood Cells

RBCs make up the major portion of blood, about 40-50% of its volume. It is the erythrocytes affinity to form so called *rouleaux* that is the main reason for non-Newtonian rheological properties of blood. The cytosol, i.e the intracellular fluid of RBCs, contains hemoglobin molecules that are essential for gas transport in circulation. In normal state RBCs are biconcave discocytes approximately 7-8 μm in diameter and 1-3 μm in height (Fig.2.2D). However, the shape of RBCs varies depending on the osmolality of a suspending media which can be easily demonstrated *in vitro*. In a hypotonic solution RBCs take a monoconcave, cup-like shape and are called stomatocytes (Fig.2.2D). If the medium is hypertonic RBCs take a shape characterized by numerous blunt spicules, known as echinocytes (Fig.2.2A). Such shape can also result as a consequence of: high pH, addition of anionic amphiphilic compounds, ATP depletion, cholesterol addition (Bernhardt and Ellory 2003), glass effect and certain cell membrane staining procedures. The transformations between these shapes are described as stomatocyte-discocyte-echinocyte transition or *SDE sequence* (Fig.2.3). This classification of RBCs shape on the SDE scale is of a qualitative nature and was created via visual inspection of small morphological differences between cell shape types. However, shape transitions from one class to another are occurs in a continuous manner. In fact,

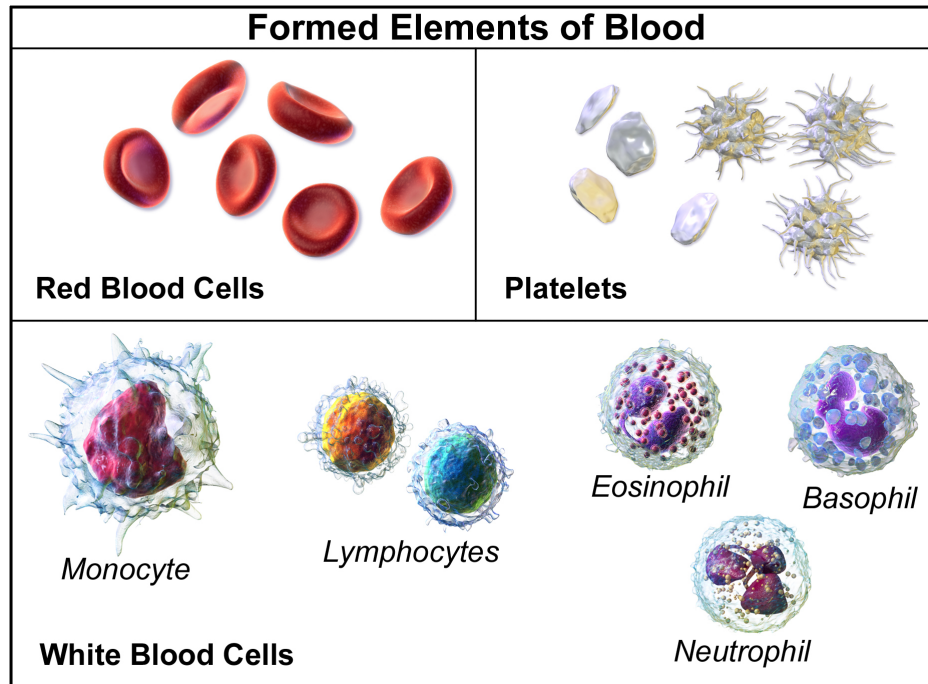


Figure 2.1. – Generic representation of blood elements. The image was adopted from [Medical gallery of Blausen Medical 2014](#).

a symmetry-based nomenclature involving more classes has already been proposed to explain the shape transitions between RBC shapes in more detail ([Lim H. W., Wortis, and Mukhopadhyay 2009](#)). Human erythrocytes don't have a nucleus or any organelles. Such a relatively simple structure gives an opportunity to model them as a membranous sack (vesicles or capsules) containing a solution with higher viscosity than outside in both experiments and numerical simulations.

The main physiological function of erythrocytes is gas exchange. In the respiratory organs hemoglobin binds oxygen and releases it in tissues. Fulfilling such function requires from RBCs passing through channels of micro-circulatory system including capillaries that are smaller in diameter than RBCs.

The morphology of RBCs is altered in multiple diseases (for example spherocytosis and sickle cell disease) and in pathological conditions (([Delaunay 2004](#)), ([Mullins 1950](#)), ([Delaunay 1995](#)), ([Christoph, Hofrichter, and Eaton 2005](#), ([Diez-Silva, Ming Dao, Han, et al. 2010a](#))). Which could lead to the blood flow obstructions and impairment of cell functions ([Byrnes and Wolberg 2017](#)). RBCs have been classified based on optical and electron microscopy images both in healthy and pathological conditions ([Lynch 1990](#)), ([Bessis, Weed. I., and Leblond F. 1973](#)), ([Alvarez, Montague, Marin, et al. 2015](#)). Healthy RBCs undergo shape transitions as a consequence of cytoskeleton and lipid bi-layer rearrangements ([Rudenko 2010](#)).

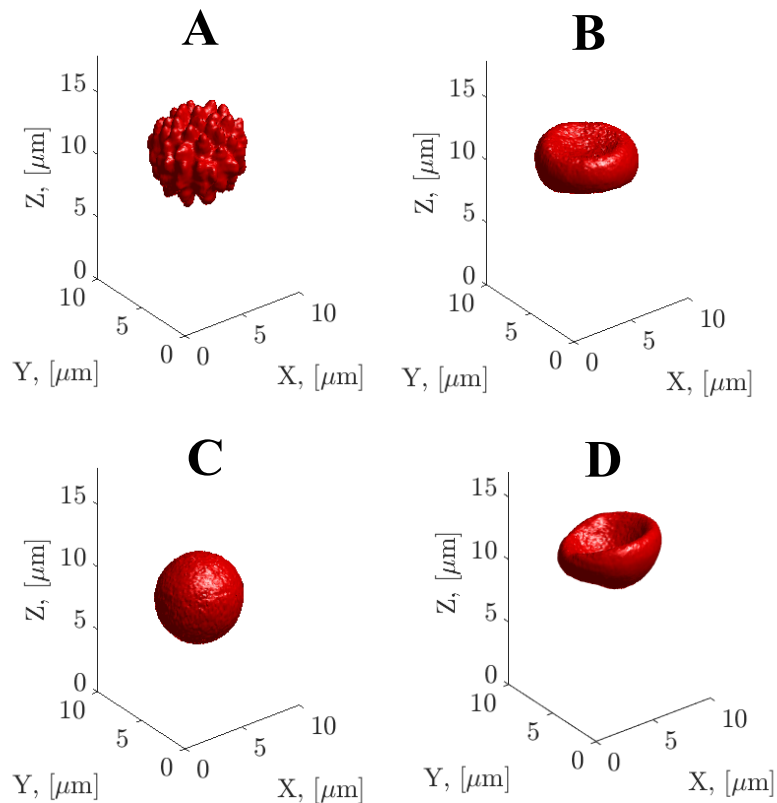


Figure 2.2. – Examples of 3D reconstruction based on confocal imaging of 3 main RBCs shape types. The original confocal data was acquired by Greta Simionato and used for 3D reconstruction in this work with her kind permission. **A** Echinocyte. This abnormal RBC shape is characterized by numerous evenly spaced spicules. **B** Discocyte. A normal mature red blood cells of a biconcave disc-like shape. **C** Spherocyte. This abnormal RBCs if shaped as a sphere instead of a regular biconcave disc. **D** Stomatocyte. A cell loses its biconcave shape and acquires a bowl-like form.

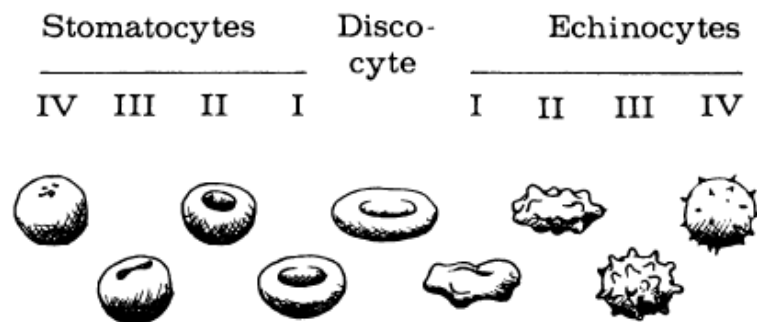


Figure 2.3. – The standard classification of RBC shape classes in use today. The picture adapted from [Betticher, Reinhart, and Geiser 1995](#)

2.1.2. Membrane of red blood cell

The RBCs membrane is composed of a lipid bilayer containing attached and embedded proteins anchored to a two-dimensional triangular spectrin network on the inner side of cells membrane (Fig.2.4). On the scale larger than thickness of the lipid bilayer (or the lattice constant of a spectrin network), the membrane of RBCs could be discussed within limits of classical theory of thin shells (Evans, Bhaduri, Popescu, et al. 2017). The composite properties of the phospholipid bilayer and spectrin network result in a discocyte morphology of healthy RBCs and give the membrane its biorheological properties (Diez-Silva, Ming Dao, Han, et al. 2010b). The lipid bilayer, while having little shear resistance, contributes to a bending resistance and is largely responsible for maintaining the surface area of a cell constant. The spectrin network on the other hand provides an elastic resistance to two-dimensionnal shear deformations and the reference shape. The ability of erythrocytes to repeatedly undergo extreme deformations is a unique feature of RBCs. Dynamic cytoskeleton remodeling of the spectrin network was shown to facilitate this fluidity (J. Li, Lykotrafitis, Ming Dao, et al. 2007). Disruptions between the lipid bilayer and the cytoskeleton are known to result in changes to the spectrin network density, which invariably causes cell morphological changes, membrane fluctuations and reduced RBC deformability for many RBC hereditary disorders.

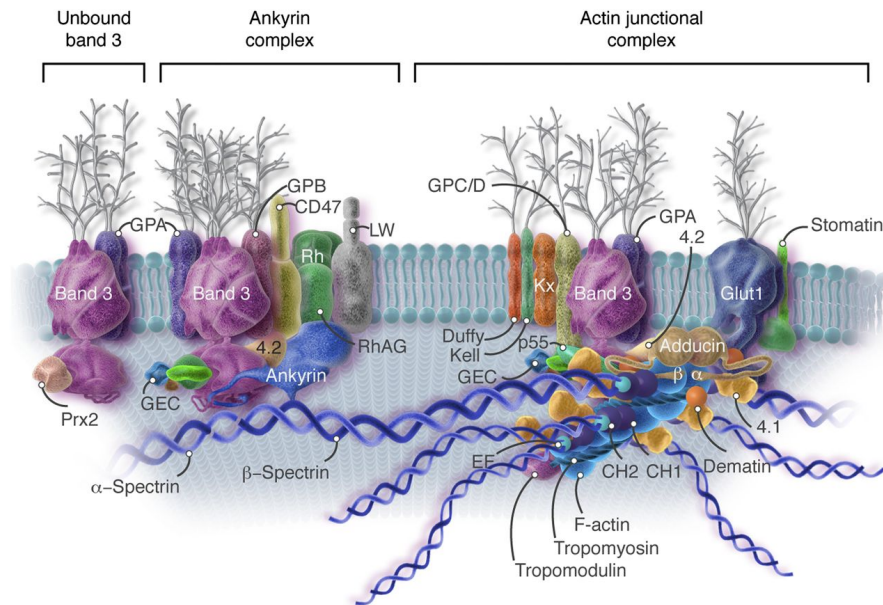


Figure 2.4. – Schematic depiction of RBC membrane and its principal components. The image was adopted from Lux 2016

Unlike liquid drops that obtain their shapes by minimizing surface tension, RBCs are constrained by the volume and surface area. Assuming the membrane as an isotropic material, Canham suggested a simple explanation for the shape of RBC (Canham 1970). The cell shape is obtained via minimization of the bending energy associated with the principal curvatures $c_1 = \frac{1}{R_1}$ and $c_2 = \frac{1}{R_2}$ (Fig.2.5). The total bending energy of the

membrane is given:

$$E_{Canham} = \frac{\kappa}{2} \int_S \left(\frac{1}{R_1^2} + \frac{1}{R_2^2} \right) dA \quad (2.1)$$

, where κ is the bending rigidity.

In 70's Helfrich introduced (in the context of lipid bilayers) spontaneous curvature c_0 reflecting membrane asymmetry (Helfrich 1973, Helfrich 1974). He proposed a model, according to which RBC obtains its shape in rest via minimizing the energy as a quadratic functional of the mean membrane curvature:

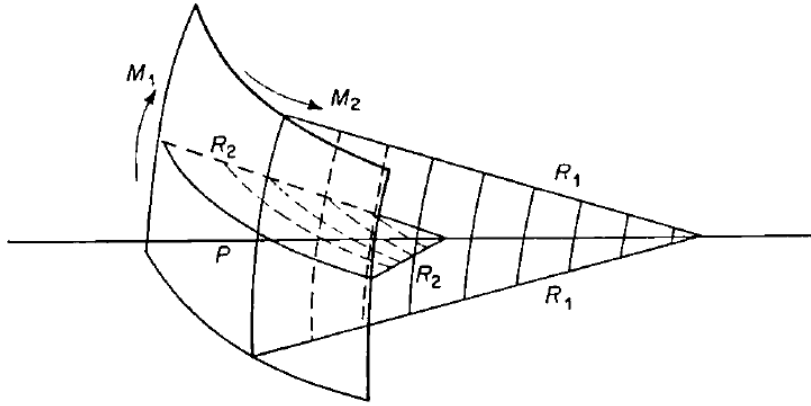


Figure 2.5. – A section of membrane which is curved in two planes. The image was adopted from Canham 1970

$$e_{Helfrich} = \frac{\kappa_a}{2} (c_1 + c_2 - c_0)^2 + \kappa_b c_1 c_2 \quad (2.2)$$

where κ_a and κ_b are elastic bending moduli (associated with mean and Gaussian curvatures respectively) with the dimension of energy, $e_{Helfrich}$ is a bending energy per area unit. The total bending energy requires a surface integral over Equation 2.2. According to Gauss–Bonnet theorem, an integral over the Gaussian curvature $c_1 c_2$ is a topological invariant and thus can be omitted in the equation for the total bending energy. In his simple geometrical model he assumed that most of the energy is stored in the bending modes of the cell membrane (Misbah 2012). Different derivations of the bending energy of lipid bilayer and its applications in numerical algorithms are summarized in Guckenberger and Gekle 2017.

Thus, the RBC shape deviation from an energetically favourable state is governed by the bending rigidity κ . The value of κ is estimated $\approx 70 k_b T$ (Betz, Lenz, Joanny, et al. 2009). In steady state, the RBC membrane experiences thermal fluctuations around its average shape. These undulations, governed by thermal energy, are known as flickering. Exposed to hydrodynamic forces, RBCs also change their shape. Such deformability of erythrocytes is largely responsible for the rheological properties of blood in microcirculation. In fact, the large distribution of cell shapes for a given flow condition is intensively

studied both numerically and experimentally ([Lanotte, Mauer, Mendez, et al. 2016a](#), [Misbah 2012](#)).

2.1.3. White Blood Cells

Unlike erythrocytes, WBCs are made up of a numerous distinct varieties, all of which have a complex cytoplasmic composition, containing nucleus, organelles and a developed cytoskeleton. In normal conditions, the volumetric portion of these cells in blood is approximately 0.1% and has a little impact on bulk blood viscosity. Lymphocytes are the cornerstone of the adaptive immune response and the basis of immunological memory. In order to protect the body – a vast terrain of countless potential targets for infectious agents – lymphocytes must be able to access the many sites where pathogens may appear ([Tuma, Durán, and Klaus Ley 2008](#)). They continually travel through the body carried by the circulatory and lymphatic systems. To carry out their physiological function, leukocytes must adhere to the wall of a blood vessel. Their adherence and further migration to inflammatory sites is a multi-step process that takes place in post capillary venules, where local changes of hemodynamics lead to relatively low shear rates.

2.1.4. Platelets

Platelets or thrombocytes are responsible for the phenomenon of coagulation in blood and the wound repair (hemostasis) along with coagulation factors. They are not cells in a strict sense of this term, but cytoplasmic fragments derived from megakaryocytes. They are smaller than the other blood cells, with no nucleus and have a rather complex inner content. Just as WBCs, to perform their physiological function platelets need to adhere to a vessel wall. In fact, in micro-scale blood flow, platelets were shown to accumulate in near wall regions, opposite to RBCs, which tend to migrate toward a vessel centerline. This lateral movement of thrombocytes in blood flow is believed to be associated with their interactions with erythrocytes and hemodynamic parameters of the flow ([W.-T. Wu, Aubry, Massoudi, et al. 2017](#)). However, while WBCs attachment to the vessel wall is followed by their migration through the endothelium, thrombocytes play a role of surface for fibrin polymerization. And if the WBCs recruitment is mostly restricted to the post-capillary venules, the deposition of thrombocytes on a blood vessel wall can occur even in the arteries. Formation of a blood clot on the inner side of a vessel, called thrombosis, can happen under certain conditions even if no injury took place. It is also a common complication on the artificial surfaces making thrombosis an important issue that needs to be taken into consideration while designing medical devices. Thrombosis can reduce the efficiency and even lead to a malfunction of such apparatuses ([Jaffer, Fredenburgh, Hirsh, et al. 2015](#)).

2.1.5. Plasma

Formed components of blood are suspended in liquid phase called plasma. It has been demonstrated in numerous studies that in shear flow plasma is a Newtonian fluid with a constant shear viscosity of about $1.2 \text{ mP} \cdot \text{s}$ at 37°C . However, a viscoelastic behaviour of blood plasma, attributed to the presence of proteins with elongational properties, was shown in the experiments in a capillary breakup extensional rheometer (Brust, Schaefer, Doerr, et al. 2013). Plasma is mainly composed (90% of its volume) of water and a grand variety of solubles ranging from a few to millions of Daltons in size. Among them can be found organic (nutrients, metabolic residues, hormones, proteins) solubles, ions (mainly Na^+ , K^+ , Ca^{2+} and Cl^-) and respiratory gases. In the normal conditions pH of plasma is slightly basic 7.35 and 7.45 depending of the tissue and osmolality maintained within 275-295 mOsm/kg. In the physiological conditions, large proteins suspended in plasma such as fibrinogen, immunoglobulin G, immunoglobulin M and etc., lead to aggregation of RBCs causing them to form multi-cell linear or branched three dimensional structures. These formations are called rouleaux due to their resemblance to a stacks of coins. Aggregation is a reversible process that commonly takes place at low shear rates or stasis. When a volumetric flow rate increases rouleaux become exposed to shear stresses that overcome aggregation forces and break apart. This reversibility of the rouleaux formation impacts flow dynamics and the viscosity of blood and is the main reason of non-Newtonian behaviour of whole blood especially at low shear rates. In microcirculation, however, aggregates break apart and whole blood rheological properties are largely governed by the deformability and dynamics of RBCs.

2.2. Microcirculation and angioarchitecture

The part of circulatory system that brings blood to the close proximity with parenchymal cells is generally referred to as microcirculation. It consists of arterioles, venules and the capillary system (Fig. 2.6). The inner diameters of these blood vessels vary from $4\text{-}8 \mu\text{m}$ in the smallest capillaries up to few hundreds microns. Microcirculatory vessels are embedded within an organ in a form of large number of closely spaced microvessels, interconnected in a complicated network. Such intricate architecture in a direct communication with parenchymal tissue allows for an adequate oxygen delivery and regulation of the blood flow in individual organs.

2.2.1. Arterioles

Arterioles form a network that consists of series almost cylindrical segments which diameters and lengths are decreasing in qualitative agreement with a power-law (Popel and Johnson 2005). Tree-like morphology of these networks in distal regions were studied in fractal form (Popel and Johnson 2005). On the inside, the arteriolar wall is covered by endothelial cells laying on a basement membrane. Underneath it is a layer

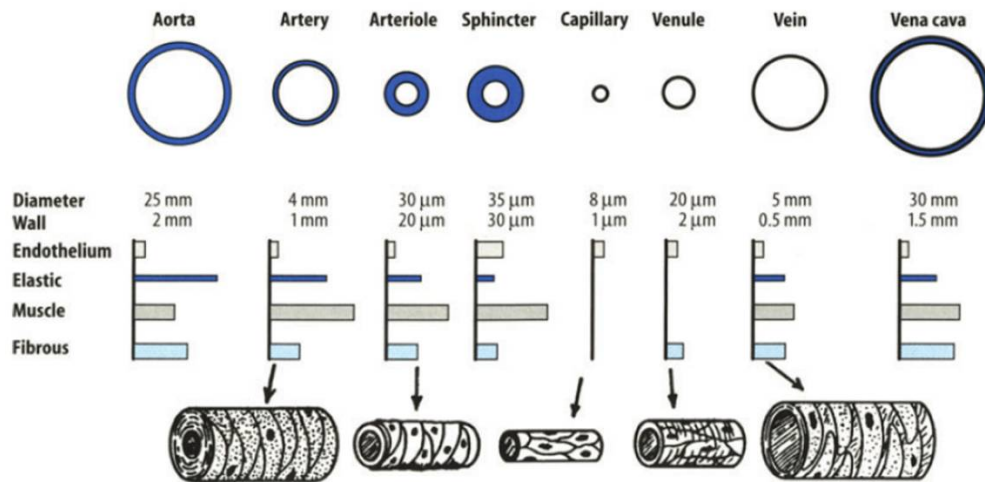


Figure 2.6. – Cross-sectional image of typical blood vessels using a relative composition of the vascular wall. Blood vessels are not represented at scale. Picture was taken from [R. Greger, \(auth.\), P. D. R. Greger, et al. 1996](#) .

of vascular smooth muscles that is connected to the central neural system through sympathetic nerve fibers. If a stimulus applied, the smooth muscles can contract or relax (vasoconstriction and vasodilatation respectively) thus changing the size of arteriolar lumen and thereby regulating the volumetric blood flow.

Despite the pulsatile nature of the blood flow, velocity oscillations, caused by the heart beating, are considerably attenuated in distal parts of the arteriolar network.

Due to their low quantity, WBCs play very small role in arteriolar hemodynamics. As was mentioned previously, adherence of leukocytes usually does not happen in arteriols. However, WBCs interact with endothelium of venules and can create obstruction to blood flow.

2.2.2. Capillaries

Capillaries are the smallest blood vessels in the body, specialized to provide maximal opportunity for gas exchange by minimizing diffusion distance between blood and parenchymal tissue. Capillary wall is deprived of smooth muscle and thus is incapable of active vasoconstriction/vasodilatation. Inner side of capillary is lined with mono-layer of endothelial cells endowed with glycocalyx surface (Fig.2.7), a layer of membrane-bound macromolecules which is typically shown by electron microscopy to be several tens of nanometers thick. However, empirical evidences imply existence of much thicker structure on surface of endothelial cells, consisting of glycocalyx and adsorbed plasma components (Fig.2.8). This structure is referred to as endothelial surface layer (ESL) ([Desjardins and Duling 1990](#), [Henry and Duling 1999](#), [A. Pries, T. Secomb, and P. Gaehtgens 2000](#), [Hans and R. 2000](#)) and its thickness can reach 1 μ m. Studies show, that

blood flow in capillaries can be regulated through modulation of hemodynamic resistance. Specifically, thickness of ESL is shown to be dependent on local shear forces. Presence of this layer may as well have influence on inflammatory processes and ischemia (W. and H. 2004).

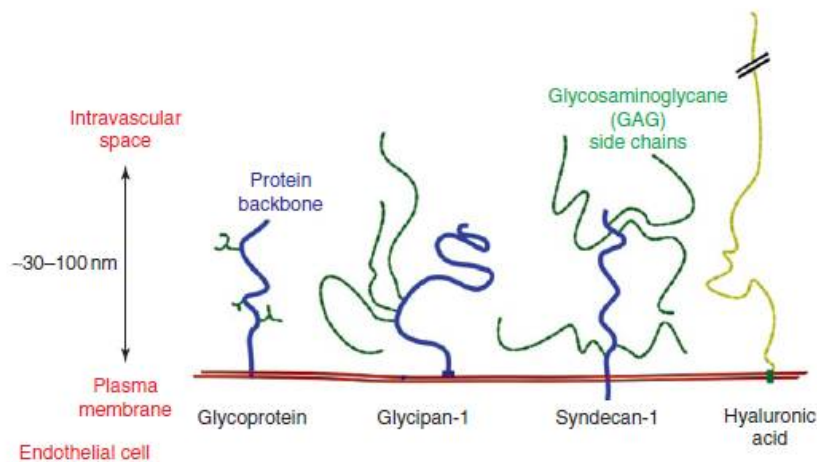


Figure 2.7. – Schematic representation of endothelial glycocalyx and its main components. Picture was taken from Tuma, Durán, and Klaus Ley 2008

Capillary diameter is typically in the range from 2 to 9 μm which is comparable or smaller than the size of the RBC (Lorthois, Cassot, and Lauwers 2011) which means that the flow in microvessels can not be described as a continuum. The flux of RBCs in the capillary network is a direct reflection of the oxygen delivery and can be measured with different approaches: as a transit time through the network, as a number of RBCs passing through the section of a capillary or as individual velocities of cells.

2.2.3. Venules

Post-capillary venules collect de-oxygenated blood and metabolic debris from the capillary network and bring them to veins. The venular network resembles to that of its arteriolar predecessor. However, venular segments are shorter and the branching occurs more frequently. The vessel wall composition resembles as well in both arteriolar and venular networks, though the segments of the latter have thinner walls. Additionally, the smooth muscle layer is entirely absent in the smallest venules connected directly to capillary network.

Due to the relatively low values of shear rate RBCs form rouleaux which impacts the flow resistance in venules drastically. The blood flow in microcirculation is constant and is not effected by the heart induced pulsations. As was mentioned before, the mean blood velocity is lower in venules compared to the velocity in arteriols of the same size (from several dozen to several hundreds microns) and is in the order of 1 mm/s (Popel and Johnson 2005).

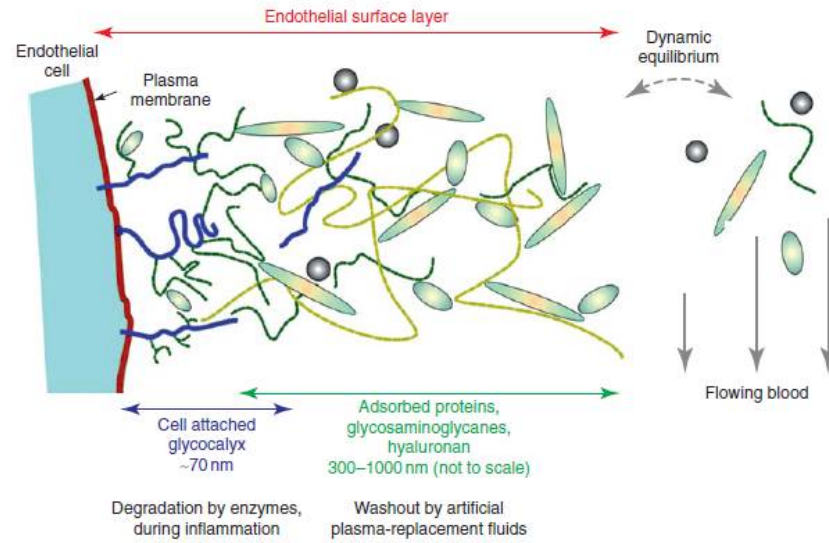


Figure 2.8. – Concept for the composition of the endothelial surface layer. The glycocalyx is the thin (50–100 nm) domain adjacent to the endothelial surface which is constituted by glycoproteins and proteoglycans bound directly to the plasma membrane. The main part of the endothelial surface layer (0.5 μm) consists of a complex array of soluble plasma components possibly including a variety of proteins, solubilized glycosaminoglycans, and hyaluronan.. Picture was taken from [Tuma, Durán, and Klaus Ley 2008](#)

2.3. Microhemodynamics

2.3.1. Basic information about flow in single microvessels. Poiseuille's law.

The main cause that drives blood flow in vessels is the pressure generated by heart contractions. About 80% of the pressure drop takes place in microcirculation. Analogously to the rules of electricity, the relationship between the flow rate and the driving pressure is expressed as:

$$\Delta P = Q \cdot R \quad (2.3)$$

,where ΔP is the pressure difference, Q is the volumetric flow rate and R is the flow resistance. Such parallel remains correct in case of the network of blood vessels. For example, if a set of parallel pathways is subjected to a certain pressure difference, the equivalent flow resistance is a harmonic mean of constituent resistances divided by their number.

In 1830 French physician, Jean-Louis-Marie Poiseuille ([Poiseuille 1830](#)), performed experiments on hydrodynamics of tube flow (direct measurements of the flow in microcirculation were not feasible at a time). From his findings was derived an equation, which eventually became know as Poiseuille's Law:

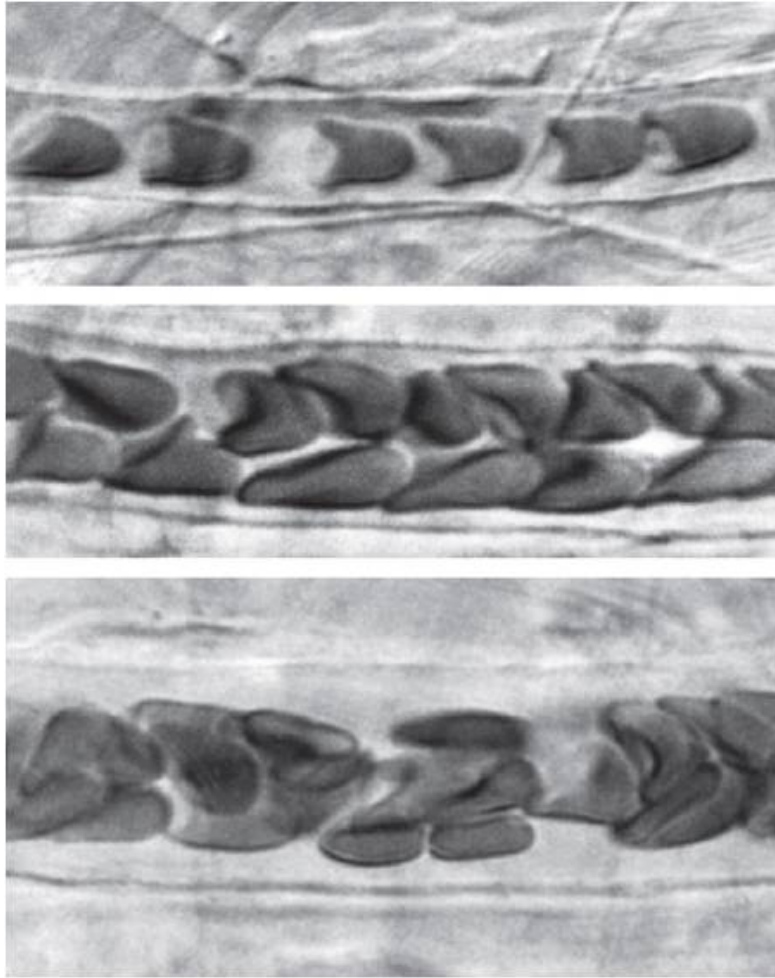


Figure 2.9. – Microcirculation *in vivo*. The figure shows the blood flow through microvessels in the rat mesentery with inner diameters 7, 12, and 16 μm (top to bottom) . Picture was taken from [Tuma, Durán, and Klaus Ley 2008](#).

$$Q = \frac{\pi r^4}{8l\eta} \Delta P \quad (2.4)$$

, where r is the radius of a tube, l its length and η the dynamic viscosity of the fluid.

In the derivation of this law several assumptions have been made:

1. The tube is circular, non-extendable and uniform.
2. The fluid is Newtonian with a constant viscosity.
3. The flow does not vary in time and is assumed to be laminar.

While blood flow, especially at a microcirculatory level, can be considered laminar, other conditions are almost never met when it comes to the blood circulation. However, Poiseuille's law serves as a good approximation and a reference point for analysis when

it comes to hemodynamics. Important feature of the Poiseuille flow is the parabolic velocity profile, reaching its highest value at the centerline of a vessel and dropping to zero at the wall.

2.3.2. Fåhræus effect

A particular implication of the non-continuum nature of blood is the formation of a cell-depleted layer close to the vessel wall. Hydrodynamic interaction between deformable RBCs and the border of a vessel results in the lateral migration of RBCs towards centerline. Consequently, the average velocity of RBCs increases with the respect to the mean flow velocity. The cross stream migration of RBCs leads to a formation of two phases: a viscous flow core consisting mostly of RBCs and cell-depleted region in direct proximity to wall that is commonly referred to as cell free layer (CFL).

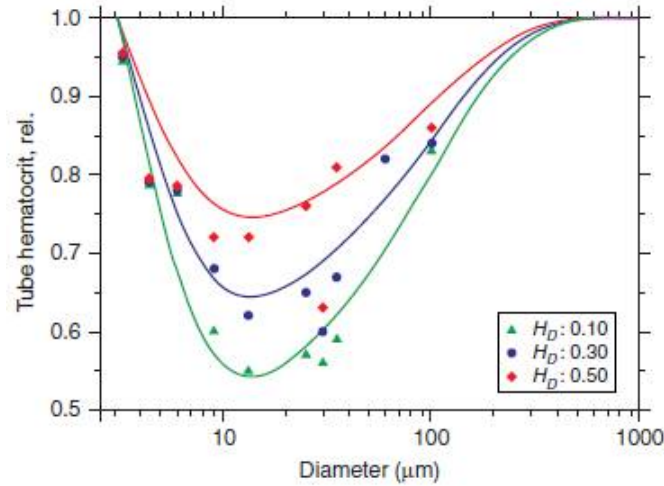


Figure 2.10. – Graphical depiction of the tube hematocrit relative to feed hematocrit as a function of a capillary diameter that explains Fåhræus effect. Picture was taken from [Tuma, Durán, and Klaus Ley 2008](#).

In 1929 Fåhræus ([Robin Fåhræus 1929](#)) demonstrated that the volume fraction of RBCs within a capillary is lower respectively to the fraction in a fluid entering or leaving it. A simple mass-balance analysis shows that this phenomenon, which eventually became known as Fåhræus effect, originates from the discrepancy of the mean velocity of cells and the average velocity of a suspension.

With that in mind, Fåhræus effect can be expressed through the following equation:

$$\frac{H_T}{H_D} = \frac{v_b}{v_{RBCs}} < 1 \quad (2.5)$$

, where H_T and H_D are the hematocrit in a tube and the hematocrit of an entering fluid respectively, v_b is an average velocity of whole blood and v_{RBCs} is an average cell velocity.

Fåhræus effect is directly linked to the formation of the CFL. In tubes with diameters much larger than the size of RBCs the impact of a cell-depleted zone on the blood flow is negligible. But as the diameter of a tube decreases it becomes comparable to the thickness of the CFL and the cell size. RBCs form a core flow in the middle of a microvessel and the discrepancy between the average cell velocity and the velocity of a whole suspension becomes significant. Later Pries et al. performed series of experiments on blood flow in glass capillaries (A R Pries, T. W. Secomb, Gaehtgens, et al. 1990). They derived an empirical equation to describe this phenomenon:

$$\frac{H_T}{H_D} = H_D + (1 - H_D)(1 + 1.7e^{-0.415D} - 0.6e^{-0.011D}) \quad (2.6)$$

, where D is a diameter of a capillary (in μm). Fig.2.10 depicts the results of *in vitro* experiments with blood in capillaries with different diameters. The solid lines are defined by Equation2.6.

2.3.3. Fåhræus-Lindqvist effect

Significant non-Newtonian properties of blood originate from two main reasons. First reason, as was noted before, is that at low shear rates RBCs aggregate which causes higher viscous resistance to flow. As the shear rate increases RBCs disaggregate. Nevertheless properties of blood as a suspension and not a continuous liquid phase start to manifest themselves. Erythrocytes increasingly deform under local fluid forces thus causing further drop in viscosity.

When addressing these properties of blood it is useful to define a so called apparent viscosity. It is a viscosity of a Newtonian fluid that circulates in a vessel with the same geometrical parameters (diameter and length in case of a circular tube) and provides the same volumetric flow for a given pressure difference. According to Equation2.4 the apparent viscosity is defined as:

$$\mu_a = \frac{\pi \Delta P r^4}{8 Q l} \quad (2.7)$$

In the physiological conditions, the cell depleted region serves as a lubrication layer that facilitates blood movement through capillaries, since its viscosity is lower than that of a bulk flow.

In 1931 Fahraeus and Lindqvist were studying blood flow in capillaries of different diameters (R. Fåhræus and Lindqvist 1931). They concluded that in tubes smaller than $300 \mu\text{m}$, due to the formation of a cell depleted layer, the apparent viscosity of blood μ_a decreases and reaches its minimum at diameters of $\approx 5\text{-}7 \mu\text{m}$. This trend is known as Fåhræus-Lindqvist effect. In tubes with diameters smaller than $5 \mu\text{m}$ the inverse effect is observed, as the apparent viscosity of blood rapidly increases. Fig.2.11 depicts the Fåhræus-Lindqvist effect. This image was adopted from Axel R. Pries, Neuhaus, and P. Gaehtgens 1992. In this work authors performed series of experiments with a capillary

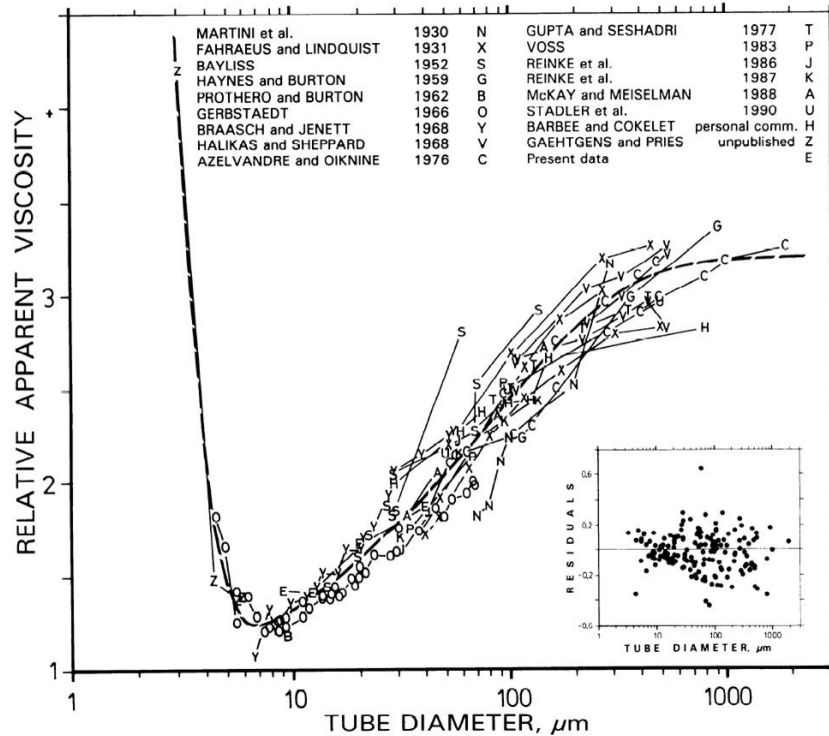


Figure 2.11. – Change in relative apparent viscosity of RBC suspensions perfused through glass tubes as a result of Fåhræus-Lindqvist effect. Hematocrit level 45%. Inner diameters of glass tubes are between $3.3 \mu\text{m}$ and $1,978 \mu\text{m}$. Picture was taken from [Axel R. Pries, Neuhaus, and P. Gaehtgens 1992](#).

viscometer and combined their results with a large amount of literature data available at a time. Three of these studies have been performed with blood from other species than humans. The tube diameters in these reports were scaled to take into account the difference in the mean RBC volume. In different studies RBCs were suspended in different media therefore data were normalized by the medium viscosity and presented in terms of the relative apparent viscosity.

In vivo however, the hemodynamic resistance in microcirculation also depends on the shear rate near a capillary wall, which is influenced by the glycocalyx and associated macromolecules.

2.3.4. Hydrodynamics interaction of particles in flow. Origin of cross stream migration

While the formation of the cell-free layer explained the Fåhræus-Lindqvist effect, reasons causing the cross stream line cell migration yet had no satisfying explanation. Since then an enormous amount of experimental, theoretical and numeric studies on both rigid and deformable objects in different flow conditions has been performed. To

analyze the collective phenomena arising in blood suspensions we first need to address the behaviour of individual particles in flow. First we will discuss basic flow solutions (Fig. 2.12)

To characterize the behaviour of fluids and the relative importance of underlying physical phenomena dimensionless numbers are often used. Most notable among them is the Reynolds number $Re = \frac{\rho l v}{\nu}$, where ρ and ν are the density and the viscosity of fluid respectively and l is the characteristic length of a channel (the hydraulic diameter of a channel D_h or the diameter in case of a circular pipe). This dimensionless quantity measures the ratio of inertial forces to viscous forces. Additionally, some practical variations of Re are distinguished. For example the channel Reynolds number $Re_c = \rho v_{max} l / \mu$ and the particle Reynolds number $Re_p = Re_c (a^2 / D_h)$, where a is the diameter of a particle. Another important dimensionless number is the capillary number Ca . It is a key parameter of RBCs motion and in studies of coupled viscous flow and deformable objects. The capillary number is often used as an expression of a relative strength of the flow. In these studies Ca defined depending on the case. In shear flow, where the behaviour of a deformable particle is mainly governed by its shear modulus G , the capillary number is defined as $Ca = \mu \dot{\gamma} a / G$, where $\dot{\gamma}$ is the shear rate and a is the effective radius of the particle. In Poiseuille flow, where the curvature radius of the flow velocity profile is comparable with the size of a particle, the bending stiffness starts to play a more important role and it's reasonable to define the capillary number as $Ca = \mu \dot{\gamma} a^3 / \kappa$, where κ is the elastic bending modulus.

Fig.2.12A demonstrates a simple shear flow. It can be envisioned as a result fluid motion induces by two plates moving in opposite directions. Plates are moving with a constant speed v^∞ and are separated at a large distance. In Couette flow (Fig.2.12B) one of the boundary plates is stationary. Both these cases impose linear flow velocity profile and, consequently, a constant shear rate $\dot{\gamma}$.

Due to the linearity and reversibility of the Stokes equation, in the limit of $Re=0$, i.e. Stokes flow, lateral migration of a neutrally buoyant particles in shear flow can not occur. The motion of a rigid sphere in a shear flow is caused by a so called drag force $F_{drag} = 6\pi\nu a v$, where ν is the viscosity of surrounding fluid, a and v are the radius and velocity of a sphere respectively. A rigid ellipsoid in shear flow exhibits a solid like rotation - periodical flipping in the direction of the flow. The problem of a spherical particle submitted to a shear flow in close proximity to the wall (Fig.2.12B) was studied by Goldman et al. (Goldman, Cox, and Brenner 1967). Their calculation lead to the establishment of the motion equations defined by the translational and rotational velocities of a sphere. In the limits of Stokes regime no lift force will act on a rigid particle for all cases illustrated on Fig. 2.12.¹

However, in the flow regime, where $Re \gtrsim O(1)$, in addition to the drag force, transverse forces act on the suspended particles causing them to migrate laterally. Rigid

1. The term "lift force" could be misleading in Stokes regime. In fact total force acting on a particle is strictly zero. However, in the manuscript, we will use the term "lift force" as often as in literature.

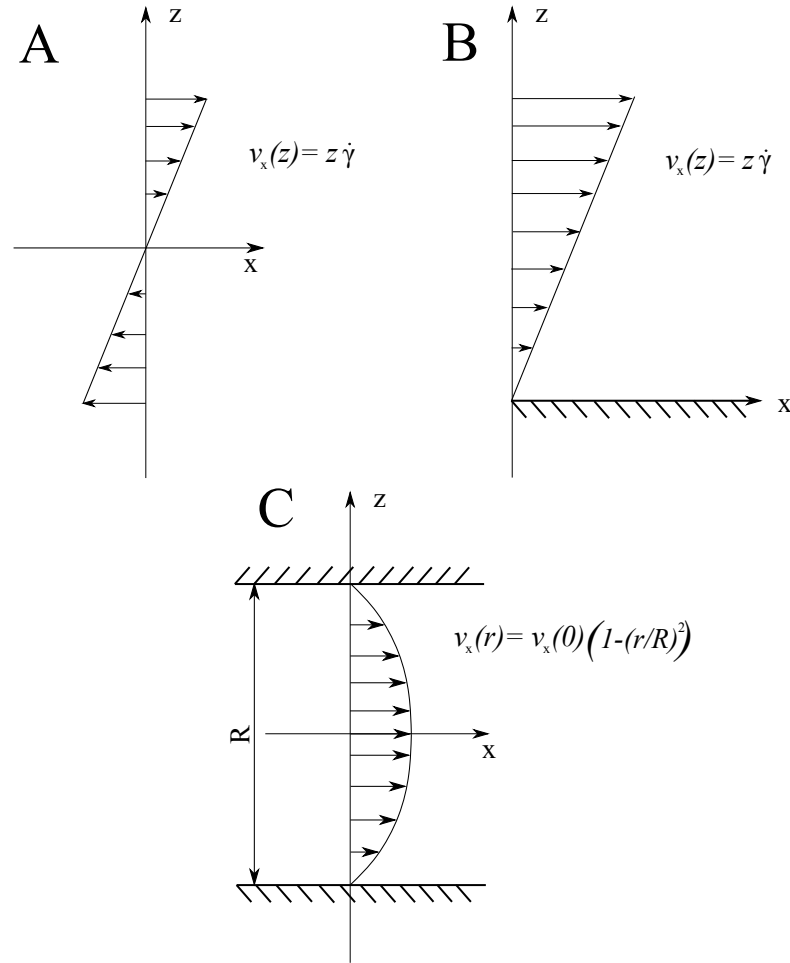


Figure 2.12. – Basic flow solutions. **A** Simple shear flow. **B** Couette flow (shear flow in the presence of a wall). **C** Poiseuille flow.

particles were found to form a thin annular region at a radial position at approximately 0.6 tube radius. This phenomenon was first observed by Segré and Silberberg in 1961 in their experiments with 0.6 and 1.7 mm spheres (SEGRÉ and SILBERBERG 1961). They concluded that to form an annulus, rigid particles that were initially randomly distributed across section must be affected by additional forces. They showed as well this re-arrangement of particles also depends on Re_p and v^2 . Ho & Leal in 1974 in case of Poiseuille flow found the disturbance of the flow field by a particle and the reflection of this disturbance at the wall to cause lateral migration of particles (Ho and Leal 1974). They showed that Segré-Silberberg effect is the result of the balance between the wall effects and the curvature of the flow.

Based on these studies it has been found that on particles in shear flow moving in a straight channel two opposite forces act: (1) the wall repulsion force, causing particles to lift away from the boundary and (2) the shear gradient force arising from the particles interaction with the curvature of the flow and causing it to migrate towards the higher

shear rate regions. The equilibrium position of particles is defined by the balance of these forces. In numeric studies Di Carlo and al. derived the lift force near the wall directed towards channel centerline as:

$$F_{LW} = C_l \frac{\rho v^2 a^6}{w^4} \quad (2.8)$$

, where C_l is a dimensionless coefficient (Di Carlo, Edd, Humphry, et al. 2009). If the particle is far enough from the channel wall force acting on it is directed away from the channel axis and scales as:

$$F_{LS} = C_l \frac{\rho v^2 a^3}{w} \quad (2.9)$$

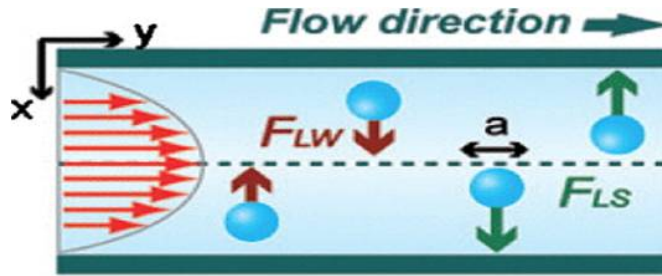


Figure 2.13. – Schematic representation of two opposite lateral forces acting on a rigid particle in the flow. Picture taken from Hwan Cho, M Godin, C.-H. Chen, et al. 2010

Goldsmith & Mason showed that at much smaller Reynolds numbers ($Re \leq 10^{-6}$) no inertial lift of rigid particles takes place (Karnis, L. Goldsmith, and G. Mason 1963).

In contrast to it, deformable particles undergoing shear deformation were shown to migrate towards channel axis. Goldsmith & Mason demonstrated the rate of this migration to increase with the object size and flow rate and claimed this trend to be based on the variation of the velocity gradient along channel cross-section. The cross-stream migration of deformable particles even in the limits of Stokes flow was later experimentally and numerically demonstrated for bubbles, vesicles and viscous capsules. The fluid membrane of vesicles has a bending resistance and is incompressible while the solid membrane of capsules is elastic (see Section 2.1.2). Vesicles cause interest in particular, since they are often used as a simple model for cells, especially RBCs, allowing capturing of basic underlying physics of the latter. Vesicles became subject of an intense research for many years after Helfrich (Helfrich 1973) introduced the concept of the bending energy. It has been shown that shapes of vesicles could be predicted by minimization of the bending curvature energy (Geislinger and Franke" 2014). The dynamics of RBCs and vesicles has been studied in numerous works, both numerical and experimental and several types of motion has been revealed (Kaoui, Biros, and Misbah 2009, Thiébaud and Misbah 2013, Vlahovska, Podgorski, and Misbah 2009).

As was noted previously, due to reversibility of Stokes equation, inertial effects must be accounted to make possible cross stream motion of rigid particles. However, in case of deformable objects, such as RBCs and vesicles, particles symmetry is lost and the lateral migration is possible at Stokes regime without inertial corrections. Multiple different expressions have been proposed in an attempt to quantify the lateral drift velocity, all of them described in terms of distance from the wall d , the shear rate $\dot{\gamma}$ and the effective radius $R = (a_1 a_2 a_3)^{1/3}$.

$$v_L = C_L \frac{\dot{\gamma} R^3}{d^2} \quad (2.10)$$

, where C_L is a dimensionless coefficient depending on the viscosity ratio λ , particle geometrical properties a_1, a_2, a_3 and the reduced volume v . Equation 2.10 is only valid for large distances from the vessel wall. In case of small distances from the wall ($d \approx R$) for neutrally buoyant particles lift velocity scales as:

$$v_L = C_L \frac{\dot{\gamma} R^2}{d} \quad (2.11)$$

This problem was studied experimentally by Abkarian et al. ([Abkarian, Lartigue, and Viallat 2002](#)) where they found the lift force acting on a vesicle both close and far from the substrate to scale as :

$$F_L = \eta \dot{\gamma} \frac{R^3}{h} f(1 - v) \quad (2.12)$$

Vesicles and RBCs always migrate to the axis of a channel. In two-dimensional unbound flow the migration velocity increases with the shear rate $\dot{\gamma}$ and reaches a saturation level above a critical value. This value in its turn depends on the curvature of velocity profile.

2.4. Margination

Margination is the main subject of this work. It is commonly acknowledged that prior to adhesion to the vascular endothelium WBCs undergo the lateral migration within a lumen of a blood vessel ([Schmid-Schönbein, Usami, Skalak, et al. 1980](#); [Bagge and Karlsson 1980](#); [Goldsmith and Spain 1984](#); [Phibbs. 1966](#); [Palmer 1967](#); [Tilles and Eckstein 1987](#); [Perkkio, Wurzinger, and Schmid-Schonbein 1988](#); [Krüger 2016](#)). It is a crucial step in the immune response that facilitates contact between the vessel wall and WBCs and allows their further migration to inflammatory sites ([Ley and Tedder 1995](#); [Alon, Hammer, and Springer 1995](#)). The presence of WBCs near the vascular wall makes possible following stages of extravasation that are illustrated on Fig.2.14. Due to differences in geometrical and mechanical properties between RBCs and WBCs, the radial migration forces arise causing preferential distribution of WBCs near vessel wall (Fig.2.15).

2.4. MARGINATION

First comprehensive study of this phenomenon ([Vejlens 1938](#)) was performed *in vivo* and demonstrated the WBCs lateral migration in the flow to be associated with RBCs aggregation. In physiological conditions this process is typical as well for other than the WBCs blood elements. Near-wall enrichment of platelets concentration is believed to be associated with fast blood clot formation and endothelial repair ([Mehrabadi, Ku, and Aidun 2016](#); [W.-T. Wu, Aubry, Massoudi, et al. 2017](#)).

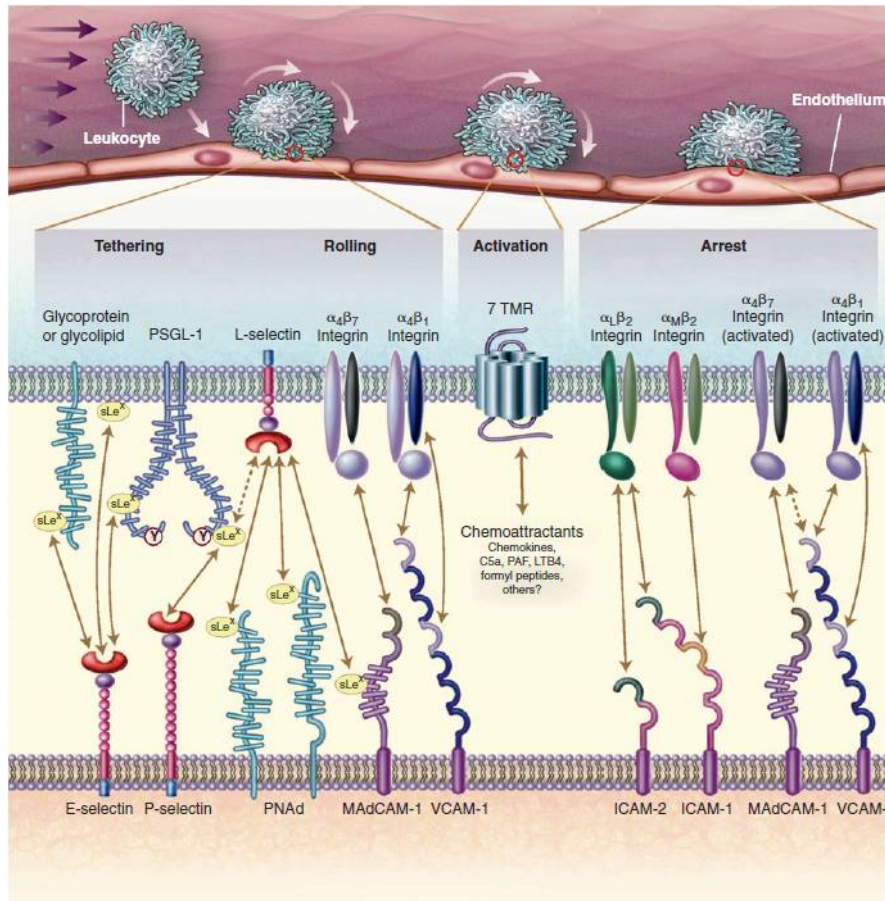


Figure 2.14. – Stages of WBC recruitment. The top picture shows the four distinct adhesion steps that leukocytes must undergo to accumulate in a blood vessel. The bottom part of this image depicts predominant molecular determinants of this process. Picture is taken from [Andrian and Mackay 2000](#).

This ability of certain suspended particles to travel from a bulk flow to vessel walls is known as *margination*. In blood flow it is believed to be mediated by RBCs and assures the role of other blood cells to be fulfilled. Lift forces, described previously, act on deformable RBCs and push them towards the centerline of a channel forcing them to occupy the core of blood flow. RBCs in their turn push other blood components towards the periphery of the flow. In case of certain diseases when mechanical properties of RBCs were altered those cells as well show the affinity of lateral migration in the flow. In case of sickle cell disease, which is accompanied by reduced deformability of sick cells,

those RBCs were reported to marginate as well ([Kumar and Graham 2012a](#); [Kumar and Graham 2012b](#)). Margination, however, is not exclusive to blood flow but can occur in any binary suspension of particles causing two sub-populations to distribute unevenly across channel section.

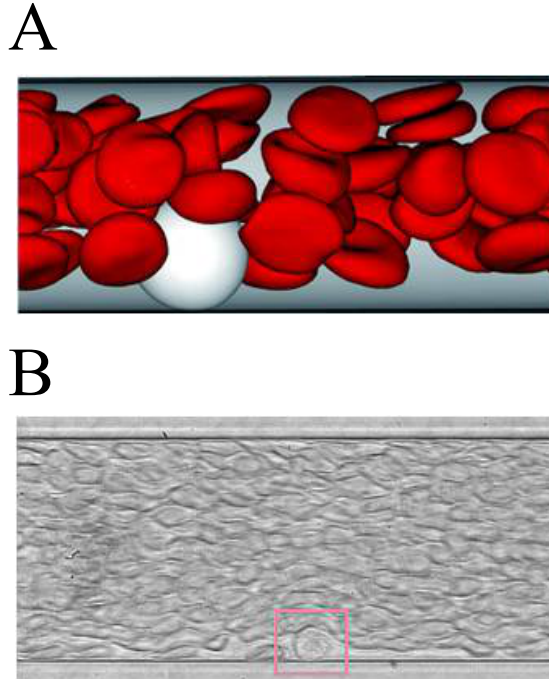


Figure 2.15. – WBC margination in microcirculation. **A** Snapshot of marginating WBC in numerical simulation. Picture was taken from [D. A. Fedosov and Gompper 2014](#). **B** Margination of WBC in pseudo two dimensional blood flow.

A particular interest in margination arises in regard to fabrication of nano- and micro-carriers in pharmaceuticals for targeted drug delivery ([Ferrari 2005](#); [R. K. Jain and Stylianopoulos. 2010](#)). For such applications the presence of drug carriers near a blood vessel wall is highly desirable and is a subject of intense research in the last decade ([Mehrabadi, Ku, and Aidun 2016](#); [E. J. Carboni, Bognet, Bouchillon, Kadilak, Shor, Ward, and Ma 2016](#); [Müller, D. A. Fedosov, and Gompper 2014](#); [Toy, Hayden, Shoup, et al. 2011](#); [Müller, D. A. Fedosov, and Gompper 2016](#); [E. Carboni and Jae-wook Nam and Xiuling Lu and Anson W. K. Ma 2014](#)). Margination depends on the properties of marginating particles, suspending media, on the geometry of microvessel network and on the imposed flow. Among particle properties, the most influential are mechanical stiffness, size, shape and particle surface properties. In nanomedicine these four characteristics are commonly abbreviated as the "4S Parameters", when referring to the nanocarriers in the targeted drug delivery ([Anchordoquy, Barenholz, Boraschi, et al. 2017](#)).

In past few decades margination was extensively studied in numerical simulations due but not limited to its physiological importance. However, very few quantitative ex-

perimental studies have been conducted. In microfluidics margination provides opportunities for cell sorting devices (A. Jain and Munn 2009, Shevkoplyas, Yoshida, Munn, et al. 2005). A simple device can be used for the separation of stiff malaria infected cells marginating in the blood flow (Hou, Bhagat, Chong, et al. 2010).

Despite the extensive research of this phenomenon the precise mechanisms involved in this process remain unclear and largely unexplored experimentally. It appears that margination is a complicated process depending on many parameters such as the size of marginating particles (Toy, Hayden, Shoup, et al. 2011; Müller, D. A. Fedosov, and Gompper 2014; Müller, D. A. Fedosov, and Gompper 2016; E. J. Carboni, Bognet, Bouchillon, Kadilak, Shor, Ward, and Ma 2016; Namdee, Thompson, Charoenphol, et al. 2013), their shape (Müller, D. A. Fedosov, and Gompper 2014; Toy, Hayden, Shoup, et al. 2011; Gentile, Chiappini, Fine, et al. 2008; Tan, Shah, Thomas, et al. 2013; Doshi, Prabhakarparandian, Rea-Ramsey, et al. 2010), the volume fraction of RBCs (Müller, D. A. Fedosov, and Gompper 2014; Müller, D. A. Fedosov, and Gompper 2016; A. Jain and Munn 2009; D. Fedosov, M. Dao, and S. Suresh 2014). However, results of many margination studies are inconsistent and sometimes contradictory partially due to the experimental conditions or assumptions made in these researches (E. Carboni and Jaewook Nam and Xiuling Lu and Anson W. K. Ma 2014). Implications of various factors on margination are summarized in the table E. Carboni and Jaewook Nam and Xiuling Lu and Anson W. K. Ma 2014. After additional actualisation in order to include latest studies on the subject, we present the following outline on the role of various factors in margination:

1. **Particle size:** Many studies indicate that there is an optimal particle size for margination to occur, but there is no consensus on the exact size. Multiple studies suggested that 500 nm and larger spherical particles exhibited marginating behavior, whereas 200 nm and smaller particles became trapped between RBCs in the core of the blood flow, away from the channel walls (*) In Liu, Zhu, R. Rao, et al. 2018 however, multiscale Lattice-Boltzmann Langevin dynamic simulation suggests the favorable margination for nano-particles smaller than 100 nm due to the Brownian motion. In Forouzandehmehr 2018 numerical simulations, the highest probability of forming ligand-receptor bond between marginating particle and the vessel wall was found for $\approx 1\mu\text{m}$ spheres.
2. **Particle shape:** Nonspherical particles with a higher aspect ratio have been found to marginate more readily than spherical particles. Particle rotation seems to be a key factor in aiding margination. (*) In Forouzandehmehr 2018 authors indicate an optimal particle sphericity factor.
3. **Particle density:** Studies are too different to draw any meaningful conclusions on the general behavior (*) Tang, Peng, J. Xu, et al. 2016 claims that golden nano-particles, being nearly twice denser than silver ones marginate faster to the vessel wall.
4. **Particle stiffness:** Conflicting simulation results have been reported for WBCs. Freund found that RBC elasticity had no effect on margination of WBCs, whereas

Kumar and Graham showed that heterogeneous collisions between a stiff and an elastic particle lead to margination. No studies have been conducted on the sole effect of the stiffness on margination (*) [Y. Chen, D. Li, Y. Li, et al. 2017](#) used diamide treated cells for their *in vivo* experiments on mice and showed margination tendency as a result of the increased stiffness. Another *in vivo* study ([Namgung, Ng, Leo, et al. 2017](#)) used glutaraldehyde fixed cells in rats. In [Gutierrez, Fish B, Golinski W., et al. 2018](#), imitating various hematological disorders, was focused on the impact of hardened RBCs on the WBCs adhesion. None of studies, however, were performed exclusively on the role of rigidity in margination.

5. **Shear rate:** The common use of particle adhesion to quantify the degree of margination leads to inconclusive results about the effect of varying shear rate. Particles may have been detached from the wall due to increasing hydrodynamic drag and/or collision with RBCs (*) A slight increment as a function of shear rate was observed in [Craparo, D'Apolito, Giammona, et al. 2017](#) between 10% and 15% hematocrit levels.
6. **Hematocrit and RBC aggregation:** No consensus (*) In [Forouzandehmehr 2018](#) authors demonstrate the decreasing adhesion probability for marginating particles with an increasing hematocrit.

Several numerical and experimental studies were performed in an attempt to define the effect of flow rate and hematocrit on margination. Yet, experimental conditions and techniques vary from one study to another. Consequently, results are often incomplete or contradictory. While some works suggest the increase of margination with a flow velocity ([E. J. Carboni, Bognet, Bouchillon, Kadilak, Shor, Ward, and Ma 2016](#), [D. A. Fedosov, Fornleitner, and Gompper 2012](#)) other showed the expressed margination at a low flow rates ([Müller, D. A. Fedosov, and Gompper 2016](#); [Namdee, Thompson, Charoenphol, et al. 2013](#); [D. A. Fedosov, Fornleitner, and Gompper 2012](#); [Zhao, Shaqfeh, and Narsimhan 2012](#); [Freund 2007](#)).

In our research we study rigidity based margination in a binary suspension of deformable and stiff particles. For this purposes we observe and quantify blood flow consisting of two populations of RBCs – healthy and rigidified with cross-linking agent (glutaraldehyde) – in microfluidic channels in case of different flow rates, hematocrits and vessel geometries. Using such experimental model allows us to examine margination caused exclusively by rigidity contrast between two sub-populations of particles. In contrast to previously performed experimental studies ([Toy, Hayden, Shoup, et al. 2011](#); [Fitzgibbon, Spann, Qi, et al. 2015](#); [E. J. Carboni, Bognet, Bouchillon, Kadilak, Shor, Ward, and Anson 2016](#)) where the imaging of marginating particles was conducted by adjusting the focal plane in the middle of a microchannel, we used confocal microscopy to reconstruct the 3D distribution of labeled cells across the section. In this study we accent following topics: (i) We investigate margination of rigidified RBCs in microchannels of different geometries and we demonstrate possible margination paths in rectangular channels, cylindrical capillaries and confined microchannels, imitating pseudo 2D blood flow. (ii) We show how distribution of rigid cells changes in the channels lengthwise and

2.4. MARGINATION

how margination reaches the saturation for different hematocrit levels. (iii) The effect of varying flow rate was studied for a wide range of values and we conclude a non-linear relationship between the velocity and margination level.

3. Materials and methods

In this chapter we will discuss general materials and methods employed in our studies. Here we will give the description of the tools and techniques that are essential and common between different experiments conducted in this work. The specifics of employed techniques will be given for each study individually in the following chapters. First we will elaborate on microfluidic fabrication. We will present and explain as well the choice of microfluidic design. After that we will present the experimental set-up based on pressure driven flow. In this section, aspects, similar in all microfluidic experiments of this study, will be discussed.

After that, we will focus on the methods of observation. Special accent will be made on the confocal microscopy, mainly on the spinning disc confocal microscope. In the last section we will discuss the application of atomic force microscopy and its relevance to this work.

Dans ce chapitre, nous exposerons les méthodes générales mises en place dans cette thèse. Ici, nous donnerons une description des outils et des techniques essentielles pour cette étude qui sont communes pour les différentes expériences réalisées dans ce travail. Les particularités et les détails des techniques utilisées seront donnés pour chaque étude individuellement dans les chapitres suivants. Dans un premier temps, nous décrirons la fabrication des dispositifs microfluidiques. Nous présenterons et expliquerons nos choix liés à la conception microfluidique. Par la suite, nous présenterons la méthode expérimentale pour laquelle nous utilisons un écoulement induit par différence de pressions. Dans cette partie, les aspects, similaires dans toutes les expériences microfluidiques de cette thèse, seront discutés. Enfin, nous nous intéresserons aux méthodes d'observation. Nous mettrons l'accent sur la microscopie confocale et principalement la microscopie confocale à disque rotatif. Dans la dernière partie, nous discuterons des applications de la microscopie à force atomique et sa pertinence dans ce travail de recherche.

In diesem Kapitel werden die grundsätzlichen Materialien und Methoden, welche in dieser Studie angewendet wurden, besprochen. Desweiteren werden Werkzeuge und Techniken beschrieben, welche zur Durchführung der Experimente in dieser Arbeit wichtig sind, wobei Spezifikationen und Details der angewendeten Techniken in den kommenden Kapiteln für jede Studie individuell angegeben werden. Als erstes gehen wir auf die Fertigung mikrofluidischer Bauteile ein und erklären die Wahl des mikrofluidischen Designs. Danach besprechen wir den experimentellen Aufbau für den

druckgesteuerten Fluss und diskutieren Aspekte, welche in allen mikrofluidischen Experimenten dieser Studie ähnlich sind. Danach besprechen wir Methoden zur Beobachtung und betrachten insbesondere die konfokale Mikroskopie, speziell die Spinning-Disk konfokale Mikroskopie. Im letzten Abschnitt besprechen wir die Anwendung der Rasterkraftmikroskopie und deren Bedeutung für diese Arbeit.

3.1. Microfluidic fabrication

Microfluidics is a technology that allows manipulating fluids on a submillimetre scale. In the past few decades significant interest to this field has risen, especially in biology and medical research. Continuously growing involvement of microfluidics in these areas is justified by compelling advantages it has over traditional assays in the cell biology. Platforms, commonly referred to as miniaturized total analysis systems (μ TAS) and lab-on-chip (LoC), can reduce substantially the sample volume and the trial cost, improve portability and sensitivity, reduce, as highly automated and integrated systems, the human error (Zhang, Yan, Yuan, et al. 2016). Microfluidics has the ability to exploit certain fundamental physical differences between liquids moving at a submillimetre length scale and macroscale. Dominating fluid phenomena are measurably different in these two cases, for example at microscale the surface tension and capillary forces take over the gravity (K Sackmann, L Fulton, and J Beebe 2014). Another very important difference is the absence of turbulences in microfluidic systems. As the flow in these conditions is characterized by low Re fluids do not mix convectively but only diffusively through their interface (G. Whitesides 2006).

Over the years materials and techniques used for fabricating microfluidic devices did undergo changes. First μ TAS were manufactured in by means clean-rooms techniques from silicon and glass. These methods were inconvenient for biological research because of silicon opacity, required non-trivial bonding techniques for closing microfluidic channels and involved expensive and often inaccessible tools. An attractive alternative to glass and Si/SiO_2 based microfluidic systems are polymers. They are less expensive and less fragile comparing to glass and silicon. Additionally, replication based fabrication processes are cheaper and faster. Duffy, McDonald, Schueller, et al. 1998 used polydimethylsiloxane (PDMS) to fabricate microfluidic devices. It made a particularly important contribution to the development of microfluidic systems. PDMS is opaque and permeable for gases, elastic, easy to handle and can be reversibly bond to various materials. Nowadays, "soft-lithography" (Xia and G. M. Whitesides 1998) based on PDMS molding became the most widely adopted technique for microfluidic fabrication in research community. However, this method also has its limitations and for several applications other techniques were developed. In search for alternative matherials, microfluidic community adopted thermoplastics, wax, paper and even cloth. Apart from that, high throughput manufacturing methods cannot be used to process PDMS making

3.1. MICROFLUIDIC FABRICATION

its commercialization complicated. However, PDMS remains the most popular material for microfluidic fabrication in a typical academic laboratory.

Such microfluidic systems became very popular in RBCs research and micro - hemodynamics studies in general. PDMS based microfluidic devices have been used to investigate dynamics of individual RBCs as well as collective phenomena for more than two decades. Due to advantages, provided by this technique, we chose "soft-lithography" to manufacture our microfluidic devices. For our purposes, a simple straight channel geometry was chosen. In this case we are not considering numerous features of angio vasculature, such as bifurcations and curvatures. And while it drives us away considerably from physiological conditions, this approach lets us observe and quantify solely the phenomenon of interest.

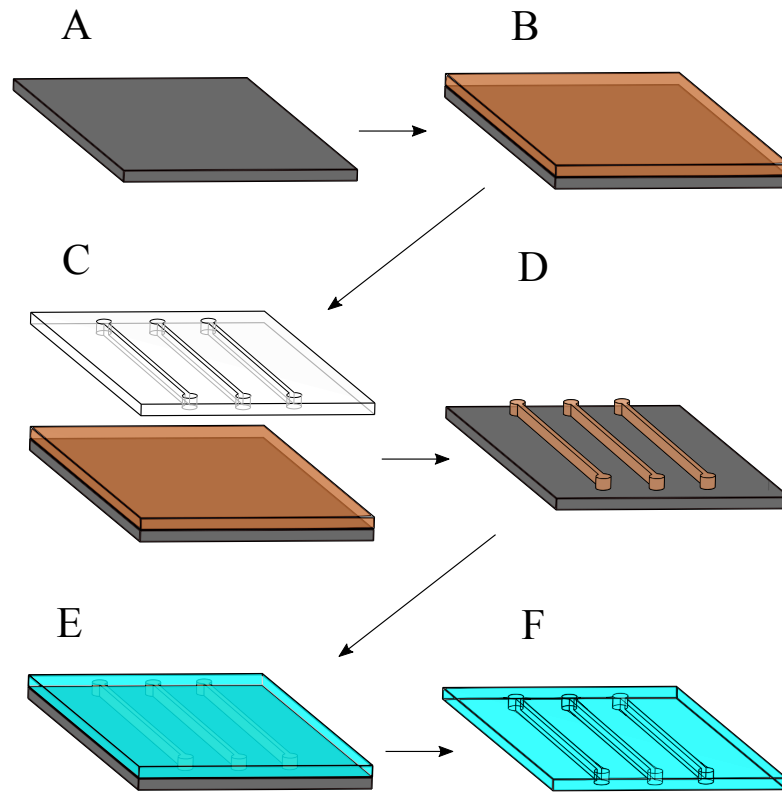


Figure 3.1. – Generic representation of the soft lithography procedure. On a silicon wafer (A) via spin-coating thin layer of photoresist gets applied (B). Through a photo mask, which is designed according to the required design, the coated wafer gets exposed to UV light causing polymerization of the coating. (C). Then, the excessive photoresist is removed by rinsing with a developing solution. This yields the silicon master for subsequent PDMS molding. D. Liquid mixture of silicon elastomer and curing agent needs to be poured on master E. After PDMS is solidified, it gets removed from the wafer. F Completing the fabrication of the microfluidic device, a cover glass is bonded to the PDMS substrate by means of plasma activation.

The required design was created with a computer software, Clewin Layout Software, Wieweb Inc. (Fig.3.2). This design was engraved on a commercially obtained chrome mask which serves as a photomask in optical lithography. First, it is necessary to create a silicon master for future PDMS molding. For that purpose a positive relief of photoresist needs to be cast on a silicon wafer. In our case, the master was created by spin-coating a silicon wafer with a thin layer of SU-8 photoresist applied on top of it. The velocity of spinning varies to obtain a required thickness of photoresist. For this study we aimed to fabricate channels of two different heights: 8 μm to imitate pseudo 2 dimensional flow and 30 μm . After spin-coating is completed, the wafer with the photoresist applied on it is pre-baked for several minutes at 65 °C and 95 °C (the exact conditions depend on a brand of photoresist, its state, a required thickness and etc.). Next, the wafer is exposed to ultraviolet through the mask, which polymerizes photoresist according to the required design. Further, follows another baking step finishing the curing process. Non-polymerized photoresist is washed off in a developing solution which leaves the positive relief and completes the fabrication of a silicon master.

The wafer serves as a mold for future fabrication of microfluidic devices and can be used repeatedly. A silicon elastomer needs to be mixed with a curing agent in ratio 9/1. The resulting mixture is poured into a petri dish over the silicon master. To get rid of bubbles, this petri dish is placed in a vacuum chamber and degassed. Then the workpiece is placed in an oven for at least an hour to solidify the solution. After that, the replica is cut from the wafer and access holes for the microchannels are stamped with a truncated needle.

The PDMS replica is then sealed to a cover glass. For that purpose, the surfaces of two connecting units are exposed to oxygen plasma. After that, activated surfaces are brought into a contact immediately once units are out of the plasma chamber. To finalize the bonding, the device is kept in an oven for at least two hours.

3.2. Pressure driven flow

The flow in the microfluidic device in our experiments was controlled by applying static pressure. Thanks to a convenience of experimental setup and a higher flow stability at low volumetric flow rates, a pressure pump is preferable to a syringe pump (flow-rate-driven flow). In our study we made use of two Fluigent MFCS™-EZ pressure devices with the ranges of pressures up to 1 bar (for experiments in 2D flow) and 300 mbars. The pressure pump is connected to a custom made 1.5 ml tube holder, which hermetically seals the sample. The latter, in its turn, is connected to the microfluidic device via flexible polyethylene tubing. The outlet of a microfluidic channel is also connected to 1.5 ml tube filled with water.

Before an actual experiment takes place, inlets, outlets and microchannels are filled with 20 mg/ml BSA in PBS solution for at least an hour in order to passivate the walls of a microfluidic chamber and decrease adhesion. As a measurement takes place, microflu-

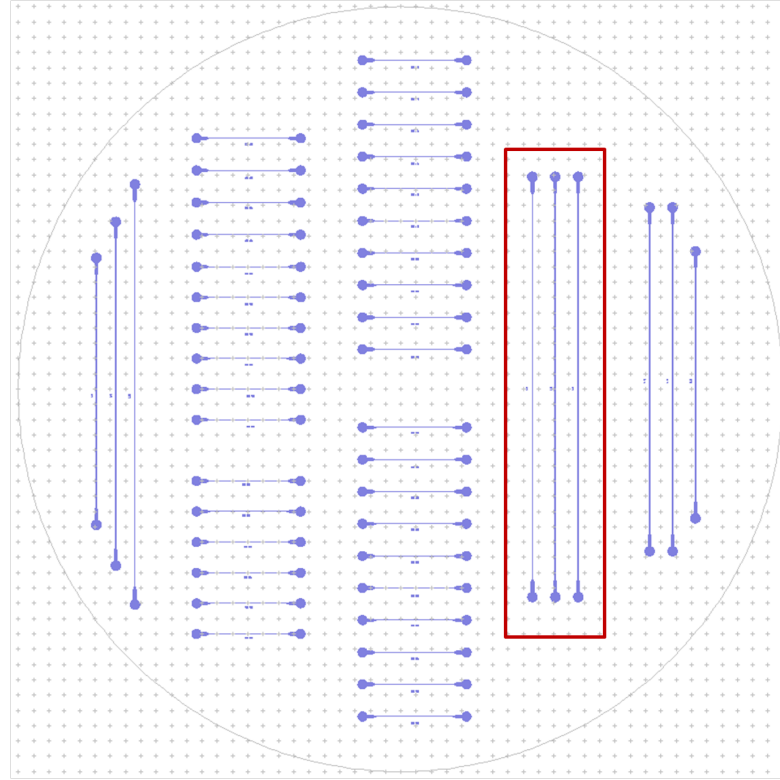


Figure 3.2. – The microfluidic design developed using Clewin software. The circle around the design defines the contour of the silicon wafer with 10 cm diameter. Straight 5 cm long channels highlighted by red rectangle were used for margination experiments.

idic device is connected to a blood sample in such manner, that no bubble formation takes place, in other words the discontinuity of the liquid phase doesn't occur. After the channel is filled completely with a blood solution, the flow is stopped and the sample holder position is adjusted to eliminate hydrostatic pressure.

3.3. Visualization

Since the objects we have been working with are relatively small, it is quite obvious that a microscope is required to observe them. However, different observation techniques were used to fit experimental conditions the best. While generally speaking, blood flow can be visualized by means of conventional transmission microscopy, the distinction between different sub-population of RBCs - healthy and chemically rigidified cells - remains impossible. In the 3D flow, the opacity of RBCs caused by absorption of light by hemoglobin, renders the distinction between cells laying in different plains impossible. To deal with this obstacle, fluorescence microscopy was implemented. To properly characterize the blood flow in channels with low width-to-height aspect ratio we

employed confocal microscopy.

This section is dedicated to a brief description of basic principals behind bright field, fluorescent and confocal microscopy.

3.3.1. Bright field microscopy

Bright field microscopy is the simplest form of imagining. White light from a incandescent source is transmitted through the specimen and the contrast is caused by attenuation of light in more dense areas of the sample which makes specimen to appear bright but darker than the background. In biological research this technique is also used for stained or pigmented samples.

Image formation begins with the light coming from an external/internal source. To create a uniform illumination of a sample, the light passes trough a condenser lens. After that the light passes through the sample and is collected by an objective to create a magnified real image. This image is magnified once again by ocular lenses to produce a virtual image that is seen by eyes.

Comprehensive study using bright field recordings of RBC flow was not realized in this work. Instead high speed image sequences were used in an attempt to estimate hematocrit level in the channel and to visualize RBC movement in pseudo 2D flow.

3.3.2. Fluorescence microscopy

Fluorescence microscopy has become a critical tool in biology and other biomedical sciences. While this technique cannot provide spatial resolution below the diffraction limit, the usage of fluorescence labeling makes possible to identify target molecules. Fluorophores (stains that attach themselves to visible or sub-visible structures), added to a specimen, emit certain wavelength once they are irradiated by the excitation light.

The basic function of a fluorescence microscope is to expose a sample to a specific band of wavelengths, and then to cut the much weaker emitted fluorescence from the excitation light. Only the emission light is supposed to reach the detector so that the resulting fluorescent structures are highlighted on the dark background. The excitation light is typically several hundred thousand to a million times brighter than the emitted fluorescence.

Fluorescence microscopy was used to estimate margination in confined channels imitating pseudo 2D flow.

3.3.3. Confocal microscopy

Conventional optical microscope has a limited spatial resolution since the light in the plane of interest is overlapped with the light diffusing from out of focus planes. In confocal microscopy, on the contrary, out-of-focus light is rejected through the use of a pinhole which improves lateral and axial resolutions.

Today confocal microscopy is commonly used across a wide range of biological sciences and two main types of microscopes are commercially available: point scanning and spinning disc confocal microscopes. First one uses a laser beam to scan a specimen point by point across a grid. The major inconvenience of this method is its low speed. To increase the scanning velocity the signal from each point must be acquired as fast as possible. To compensate for the short illumination of each pixel an intense laser must be used. To overcome the problem of the low scanning velocity, in spinning disc confocal microscope (Fig.3.3) is implemented Nipkow-disk. In this technique the laser beam illuminates an array of microlenses arranged on a (collector) disk. Each microlens has an associated pinhole laterally co-aligned on a Nipkow-disk and axially positioned at the focal plane of the microlenses.

The pinholes (and microlenses) are arranged in a pattern, which scans a field of view defined by the array aperture size and the microscope objective magnification. The scanning laser beam excite fluorescent labels in the specimen. In such manner, this technique allows an array of lines to scan the specimen simultaneously. Additionally, spinning disc confocal microscope uses digital camera as a detector, which can have a very high quantum efficiency.

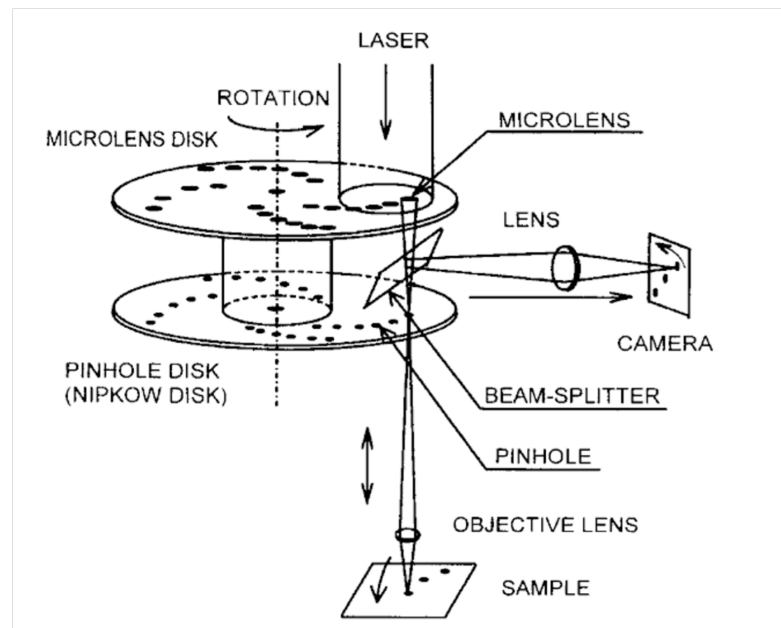


Figure 3.3. – Schematic representation of optics in Yokogawa spinning disc. Image was adopted from [Vesely 2007](#).

However, for our particular study, as we observe moving cells, this method has an inconvenience. Imaging of a traveling object through a pinhole of a rotating disc may result in the stroboscopic effect, if an object moves too fast. In this study all confocal measurements were performed with a spinning disc based confocal head (CSU-W1, Yokogawa Electric Corporation) coupled with an inverted microscope (Nikon Eclipse Ti). A solid state laser ($\lambda = 647 \text{ nm}$, Nikon LU-NV Laser Unit) was used as a light source for irradi-

ation of fluorescently labeled cell. Image sequences were acquired with a digital camera (Orca-Flash 4.0, Hamamatsu Photonics, Hamamatsu City, Japan).

3.4. Atomic force microscopy

Binnig, Quate, and Gerber 1986 introduced atomic force microscopy (AFM) which brought a radical change to biomedical research and imaging of cells. It opened new possibilities for the investigation of biomedical specimens such as 3D mapping of surface based on true topological data with vertical resolution down to the sub-nanometer accuracy. AFM allows examining of any sufficiently rigid surface in a liquid environment or in the air. It combines a higher resolution compared to optical microscopes with an ability to study non-fixed cells, unlike scanning electron microscope.

Fig.3.4 shows schematically the main components of scanned-sample AFM. The tip of the cantilever is brought to the contact with the sample and is used to scan the surface, sense the variations of the specimen, and generate 3D images. Modern cantilevers are usually made from silicon/silicon nitride and are fabricated based on the technological process similar to that used in manufacturing integrated circuits. The choice of a cantilever is mainly based on its spring constant and its resonance frequency.

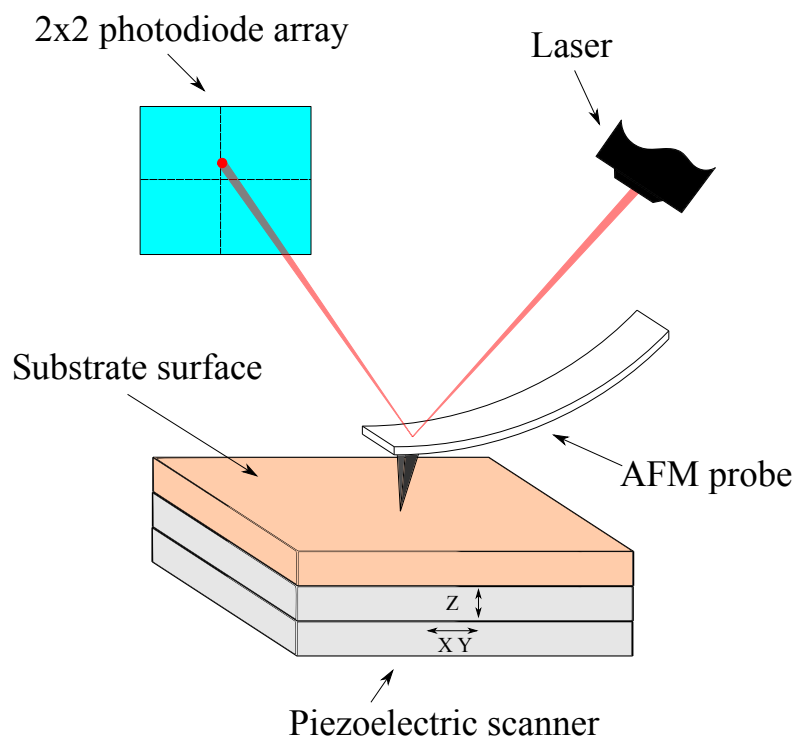


Figure 3.4. – Main components of atomic force microscope.

The deflection of a cantilever, brought into a contact with a specimen, is measured on a principle of an optical level (Braga and Ricci 2004). Laser beam is reflected from

the backside of cantilever onto a position sensitive photodetector, which consist of at least two side-by-side photodiodes (four, if a system provides evaluation of lateral deflection). Distance between cantilever and photodetector is generally 10^3 times larger than cantilevers length. Because of that, deflection of a cantilever gets greatly magnified and could be detected with high accuracy. Piezo electric motors control position of a cantilever in the direction perpendicular to specimen plain. Motors, laser beam and cantilever are set together in a constant feedback loop.

The AFM allows measurement of forces within a pico-Newton range. The instrument can be used to record the amount of force felt by the cantilever as the probe tip is brought close to a sample surface, eventually indent the surface and then pulled away (Braga and Ricci 2004). In this mode, the AFM registers a force-distance curve that provides information about the tip-surface interaction, the elasticity and the stiffness. Acquiring series of force curves, at different points of a grid allows the user to create force maps that represent local mechanical properties of a specimen (map of stiffness for example). Two important points must be taken into consideration while acquiring force-distance curves. The photodetector signal has to be calibrated before starting the measurement and after the calibration it is essential that the laser alignment is left unchanged. Another crucial step is converting the deflection curve into a force curve by using the force constant of the cantilever. As a rule, manufacturers specify the force constant of their cantilevers. However, due to significant variations for individual devices, the direct measurement of the spring constant is required for every experiment.

Despite the fact, that AFM is an extremely powerful asset in biomedical research, it is a challenging technique in numerous aspects and acquired data sometimes are hard to interpret. In this work we characterized the effective Young's modulus of rigidified RBCs via AFM measurements of force-distance curves. Experiments were performed in a liquid environment (PBS) using a JPK Nanowizard 3 AFM coupled to an optical microscope. In this section will be given information about the experimental procedure, the cantilever choice and the force-distance curves analysis.

3.4.1. Cantilever choice

A cantilever is the heart of AFM measurements. The proper choice of one and its calibration largely define the outcome of an experiment. Today, many companies offer convenient solutions for handling cantilevers. An assembly of multiple cantilevers (that could have different resonance frequencies, spring constants, shapes and have different tips) on a chip, big enough to be handled by an operator and fixed in the machine, can be purchased.

There are mainly cantilevers of two shape types available: "V"-shaped triangular and "single-arm" rectangular ones. The later is preferable in lateral force microscopy, when a photodetector measures as well the torsion of a cantilever. The backside of a cantilever is often coated with a thin layer of metal to create a reflecting surface. However, in such case the vertical deflection changes significantly with time, due to the difference

in the coefficients of thermal expansion. The tip shape has a strong influence on the quality of recorded data as well. It's the part of a cantilever that is actually interacting with the surface. Its essential parameter is the sharpness of its vertex. Intuitively, a high resolution image is only possible with a very pointy tip. Nevertheless, sharper tip doesn't always provide better resolution and, in case of scanning living cells, could damage the specimen. A standard cantilever tip is usually a pyramid with an apex radius ≈ 30 nm. There are various cantilever tip types available on the market (cones, cylinders, pyramids, tipless cantilevers and etc.) and, evidently, the indentation of a sample during a measurement is related to the size and shape of a tip.

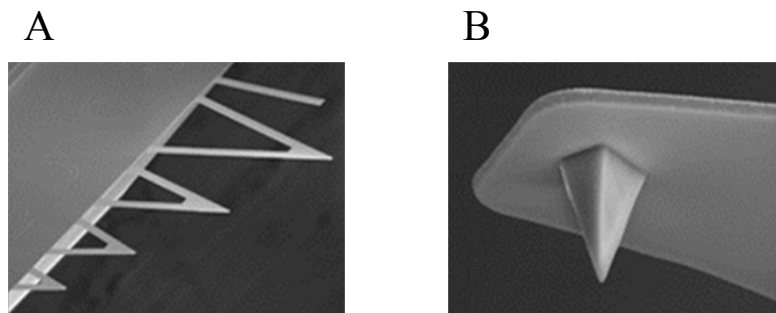


Figure 3.5. – Images of MLCT cantilevers used in this research. Images were adopted from official web-page of manufacturer ([n.d.](#)).

It is crucial to choose a cantilever with a proper spring constant and resonance frequency. Softer cantilevers are used for softer samples and more rigid cantilevers for stiff specimens. Ideally, one should aim for equal deflection of a cantilever and indentation of a sample. In our study, Bruker MLCT cantilevers were used (Fig.3.5). Before taking a large amount of data, samples were tested with different cantilevers and measurements were checked, to make a proper choice of a cantilever.

3.4.2. Force-distance curves

AFM can be used to record the force, cantilever is afflicted by, as the probe tip is brought into a contact with a specimen surface, indents it and gets pulled back. Once close to the surface of a sample, the cantilever tip experiences superposition of various attractive and repulsive forces often described with Lennard-Jones potential, that reaches minimum $-\epsilon$ of a potential well at $r = r_m$:

$$V_{LJ} = \epsilon \left(\left(\frac{r_m}{r} \right)^{12} - 2 \left(\frac{r_m}{r} \right)^6 \right) \quad (3.1)$$

Fig.3.6 shows a typical force curve of cantilever deflection vs. z -piezo. When the probe approaches the surface, at the beginning, the cantilever remains in a non-interacting equilibrium state (if a long distance attractive or repulsive force is active, a portion of the force curve will reflect it). In close distance from the surface, the probe starts to experience various attractive forces and the cantilever bends. With further approach

probe jumps-to contact. After that cantilever deflects until it reaches applied force. The slope of this curve depends on the elastic modulus and the geometries of the tip and the sample. During the retract, adhesion or bonds formed while in contact with the surface cause the adherence between the sample and the tip. As the withdrawal continues, at some point the cantilever stiffness overcomes adhesion forces, the tip detaches from the surface (often referred to as "snap off") and the cantilever returns to a non-deflected state. In order to obtain a plot of tip-sample interaction forces vs. tip-sample distance, one must know the cantilever deflection δ_c and its spring constant k_c . Then deflection can be conveniently converted into force according to well known Hooke's law:

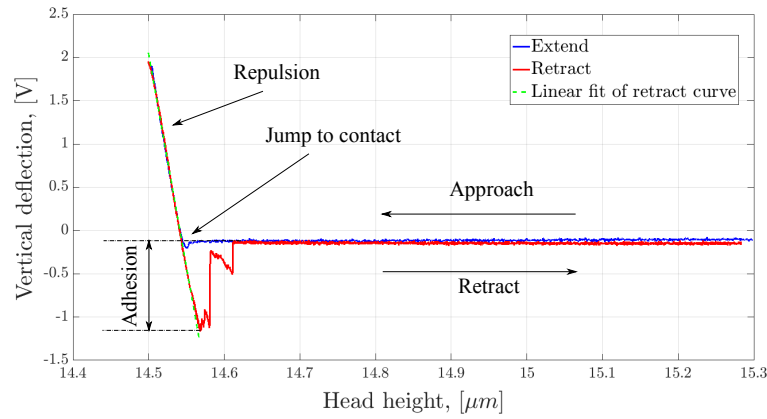


Figure 3.6. – Representative force-displacement curve of AFM measurements that was used for the sensitivity calibration of a cantilever. The curve was acquired as a result of interaction between cantilever tip and the ibidi Polymer Coverslip in air and illustrates various stages of AFM measurement.

$$F = -k_c \delta_c \quad (3.2)$$

However, it is important to mention, that the distance controlled during a measurement is the displacement of piezo motors, cantilever deflection δ_c and the sample deformation are unknown in advance. Therefore, the raw curve obtained by AFM should be called "force-displacement curve" rather than "force-distance curve". This latter term should be employed only for curves in which the force is plotted versus the true tip-sample distance, that has been previously calculated from raw data (Butt, Cappella, and Kappl 2005).

From force-displacement curves in contact region it is possible to obtain a detailed information about mechanical response (elasticity, viscoelasticity, plasticity) at selected points on the cell surface (H. W. Wu, Kuhn, and Moy 1998). In our study, in order to characterize the rigidity of RBCs (healthy ones as well as chemically rigidified) we determined the elasticity (i.e., Young modulus) of cells via by AFM force mapping. Let the sample and cantilever tip to be continuous elastic media (neglecting plastic deformations). The elastic constant of the sample k_s depends on the Poisson ratio ν_s , the Young

modulus E_s and the radius of a contact area a according to:

$$k_s = 2a \frac{E_s}{1 - \nu_s^2} \quad (3.3)$$

Multiple theories, which are summarized in [Butt, Cappella, and Kappl 2005](#), were developed in order to establish the relation between the radius of contact area a , the force and the penetration depth. In cases when surface forces could be neglected, Hertz theory can be invoked ([Hertz. 1896](#)). [Sneddon 1965](#) modified Hertz theory for a rigid probe interacting with an elastic surface:

$$F = \frac{3}{2}Ka \int_0^1 \frac{x^2 f'(x)}{\sqrt{1-x^2}} dx \quad (3.4)$$

, where $f(x)$ is the function describing the profile of a probe and K is a reduced Young modulus given by:

$$\frac{1}{K} = \frac{3}{4} \left(\frac{1 - \nu_s^2}{E_s} + \frac{1 - \nu_i^2}{E_i} \right) \quad (3.5)$$

In [3.5](#) E_s, E_i and ν_s, ν_i are the Young modulus and the Poisson ratios of the sample and indenter respectively. This leads to the equation, used by JPK software for the data analysis in case pyramidal probes:

$$F = \frac{1}{\sqrt{2}} \cdot \frac{E_s}{1 - \nu_s^2} \cdot \tan(\alpha) \cdot \delta^2 \quad (3.6)$$

, where α is a face angle of a four-sided regular pyramid and δ is sample indentation.

3.4.3. Experimental procedure

As was mentioned before, although manufacturers provide the information about spring constants of their cantilevers, the system has to be calibrated every time a probe is mounted on the AFM. To convert the voltage, measured by a photodetector, into a force-displacement curve two calibration steps are necessary ([Fig.3.7](#)). First, one must measure the sensitivity of the system. For that purpose, a user measures the deflection of a cantilever against very hard substrate for a given movement. The repulsive region after the contact of resulting force curve is linear and a software uses it define a factor of converting Volts into nanometers. There are several methods to measure the cantilever spring constant: deriving spring constant from cantilevers geometry, using a reference cantilever, measurement using thermal noise. The latter method, is included in JPK software as a built in routine.

AFM is a complex system and one should be careful processing and interpreting data acquired with this technique. Artifacts, that could be recorded during AFM measurements, originate from entirely different physical interactions than in conventional

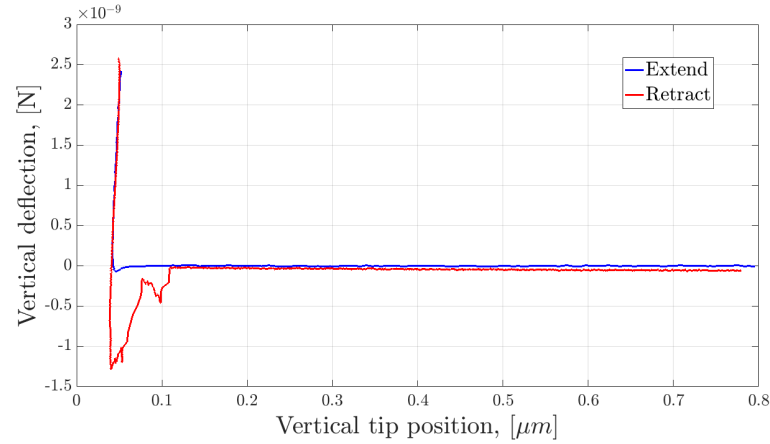


Figure 3.7. – Examples for the conversion of photodetector signals (Volts) into forces (Newtons). Using the JPK data processing software, the position of the AFM head was converted into the position of the cantilever tip. The contact regime between the rigid surface of the dish and cantilever tip is represented by a vertical line, showing no indentation during approach. The curve is slightly tilted as a result of a calculation error (5 nm).

microscopy. In our study, a special attention should be paid to artifacts arising from the glass substrate effect (for healthy RBCs) and the cell geometry (rigidified RBCs). When force-distance maps of rigid RBCs were recorded, in order to characterize their elasticity, the results for Young modulus depend strongly on the position of a cantilever/point of measurement. Force-distance curves appear to be qualitatively different from the cell periphery to the center which might mean inhomogeneity in the Young modulus spacial distribution (Ciasca, Papi, Di Claudio, et al. 2015). It appears though, that it is a result of particularity of AFM measurements related to the cell geometry. When a cantilever gets in contact with a cell in zones with high curvature a tangential force component occurs and alters the measurement, a cell slips from under the probe, resulting in the decrease of measured Young modulus. Because of that, data were extracted only from a circular zone on the surface of cells, normal to the approaching probe.

4. Metrological development

In this chapter we will describe the methods designed in order to control experimental parameters of this study. Here we describe the development of all the necessary techniques required to properly conduct our measurements. In the following we explain how we characterize and quantify the parameters essential for this study. Hence, this chapter is separated from the general description of materials and methods used for this work. We start with blood sample preparation technique. We will provide short analysis of rheological properties of a blood suspension. We will elaborate on the velocity measurement in microfluidic experiments. We will describe the image analysis employed in the margination studies and elucidate the main steps of data processing.

Ce chapitre détaille les méthodes développées pour contrôler les paramètres des expériences dans cette étude. Ici, nous décrivons le développement de toutes les techniques nécessaires pour mener à bien nos mesures. Nous y expliquons comment nous avons caractérisé et quantifié les paramètres essentiels de la présente étude. A cause de ça, ce chapitre est séparé de la description générale des matériaux et des méthodes exposées dans le précédent chapitre. Nous commençons avec la technique de préparation des échantillons du sang. Nous y présentons une courte analyse des propriétés rhéologiques du sang. Nous expliquons aussi la procédure pour mesurer la vitesse dans les expériences microfluidiques. Nous décrivons le traitement d'images mis en place dans les études de margination et expliquons les étapes principales de traitement de données.

In diesem Kapitel werden die Methoden, welche zur Kontrolle der experimentellen Parameter in dieser Studie genutzt werden, sowie die Entwicklung aller nötigen Techniken beschrieben, um die Messungen ordnungsgemäß durchzuführen. Im Folgenden wird erklärt, wie die essentiellen Parameter dieser Studie charakterisiert und quantifiziert werden. Daher ist dieses Kapitel von der generellen Beschreibung der Materialien und Methoden dieser Studie getrennt. Wir beginnen mit der Technik zur Vorbereitung von Blutproben und analysieren kurz die rheologischen Eigenschaften einer Blutsuspension. Wir gehen auf die Geschwindigkeitsmessung in mikrofluidischen Experimenten ein, beschreiben die Bildauswertung, welche in der Marginations-Studie angewendet wurde und erläutern die Hauptschritte der Datenverarbeitung.

4.1. Blood sample preparation

Initially, blood samples (containing ethylenediamine tetraacetic acid (EDTA)) for our study were ordered from Etablissement Francais du Sang (EFS). Samples were received the day after intake from the donor and were kept in the fridge at 4°C throughout the week. To separate RBCs from other blood components, lymphocyte separation medium was used (Histopaque-1119 density gradient solution, Sigma Aldrich). After red blood cells were washed 3 times in phosphate buffered saline (PBS). PBS was prepared using soluble tablets (phosphate buffered saline, Sigma Aldrich). To increase density of solution, and thus decrease sedimentation of RBCs during microfluidic experiments, 10 mg/ml of Dextran 40 was added to the solution. In order to inhibit adherence of RBCs to cover glass and PDMS, we used as well 10 mg/ml of bovine serum albumin (BSA, Sigma Aldrich) in our solution.

Unfortunately, this protocol proved itself ineffective in time. First of all, reliance on external supply of blood samples was inconvenient. Blood storage throughout the week undermined quality of results. Even when sample was stored at 4°C, number of echinocytes increased drastically within 2-3 days ([Makhro, Huisjes, Verhagen, et al. 2016](#)). Stock solution prepared by dissolving PBS tablets did not hold osmolarity and pH after addition of BSA and Dextran 40. Though, density of suspending media was increased by adding Dextran 40 to solution, hematocrit level during experiments was constantly rising due to sedimentation.

Gradually, new protocol was developed in order to overcome these obstacles and results of this study were acquired according to following procedure. For microfluidic experiments relatively "large" volumes of blood (several milliliters) were required in comparison to the study of individual RBCs. Whole blood was taken from healthy volunteers via venipuncture and collected into vacutainer tubes containing EDTA. First, blood was centrifuged (Hermle Labortechnik GmbH Z36HK) at 1400 g for 10 minutes to separate RBC from plasma and other blood components, which were carefully piped out. After that, RBC pellet was thoroughly washed 3 times in PBS (Gibco Life Technologies), acquired as stock solution and not pills, containing 10 mg/ml of BSA and 5.5 mM of glucose (Sigma-Aldrich). Washed cells were finally resuspended and adjusted to required hematocrit in isodense iodixanol based solution (OptiPrep™, Sigma-Aldrich). Suspending media used for blood samples prevented RBCs from sedimentation and contained 35% v/v concentration of OptiPrep™ in PBS, 10 mg/ml of BSA and 5.5 mM of glucose. The necessary RBCs concentration was achieved by carefully pipeting a required volume of washed RBCs pellet. The hematocrit level of a blood sample was verified with micro-hematocrit centrifuge. Small portion of RBCs (<1%) was rigidified with glutaraldehyde (Sigma-Aldrich, Saint Louis, USA) for 1 hour, thoroughly washed and then fluorescently labeled with CellMask™ Deep Red Plasma membrane stain (Molecular Probes Life Technologies). Labeled stiff cells were added to the sample to create a binary suspension with two populations of cells with different rigidities. Fixed cells were kept as a stock solution at 4°C for indefinite period of time in PBS containing 20 mg/ml of BSA in order to pas-

sivate any residuals of glutaraldehyde. Blood collection and realization of experiment took place the same day.

In microfluidic experiments, hematocrit values correspond to the volumetric concentration of RBCs in the sample (i.e. hematocrit of the entering fluid, see Section 2.3.2). Hence, these hematocrit values will be further referred to in this work as *discharge hematocrit* H_D . To make correction for the Fåhræus effect we calculated expected values of RBCs in the microchannel (*tube hematocrit* H_T) using equation 2.6. In these calculations instead of capillary diameter the hydraulic diameter of a microchannel $D_h = \frac{2ab}{a+b} \approx 40 \mu\text{m}$ was used. The corresponding H_T values are:

$$\begin{aligned} H_D = 10\% &\rightarrow H_T = 6.52\% \\ H_D = 20\% &\rightarrow H_T = 13.82\% \\ H_D = 40\% &\rightarrow H_T = 30.72\% \end{aligned} \tag{4.1}$$

To prepare the samples for the study dedicated to morphology of individual RBCs, not more than a few drops of whole blood were required. Blood was drawn from three healthy volunteers via finger prick into the tubes containing 5 μl of EDTA 1.6 mg/ml. 10 μl of each sample was therefore resuspended in 1 ml of different concentrations of NaCl solution: 0.9 % NaCl was used to keep discocyte shape and 0.4 % NaCl to induce sphero-stomatocytes formation. Intermediate shapes were obtained by suspending cells in 0.5 % NaCl (stomatocytes type I and II) and 2.5 % NaCl (echinocytes type I and II) solutions.

400 μl of each cell suspension was fixed in 1 ml of 1 % glutaraldehyde solution in NaCl. In order to fix cells with the desired shape, each glutaraldehyde solution was prepared to have a total osmolarity equal to the osmolarity of the NaCl solution used to induce each shape. Fixed cells were placed in a rotator-mixer (Grant-bio PTR-35, Grant Instruments, Cambridge, England) at room temperature overnight. Samples were later centrifuged at 4000 g for 5 minutes (Eppendorf Micro Centrifuge 5415 C, Brinkmann Instruments, NY, USA), washed three times with 1 ml of each respective NaCl solution used to induce the different shapes and eventually resuspended in 1 ml of the same solution. 5 μl of CellMask™ Deep Red plasma membrane stain 0.5 mg/ml (Thermo Fisher Scientific, Oregon, USA) was added to each sample for 30 minutes at room temperature. Afterwards, cells were washed three times as described before. Echinocytes type III were created from with healthy cells by exploiting the glass effect: first 10 μl of blood were suspended in 1 ml of PBS and labelled with CellMask™ Deep Red. For this reason, cells were washed, resuspended in PBS and finally placed on a glass slide for confocal microscopy.

4.2. Rheology

We have performed several experiments to determine the viscosity of our blood solution with ANTON Paar MCR 702 rheometer (Fig. 4.1). For these measurements we

were using counter-rotating cylinders (the CC20 Taylor-Couette geometry) in order to minimise the sedimentation effect. The data were acquired for six hematocrit values between 5-50%, 4-5 blood samples each value. As a frame of reference, additional viscosity data for the whole blood were included to demonstrate the shear-thinning behaviour of unwashed suspension of RBCs. In this case the formation of aggregates (rouleaux) due to the presence of plasma proteins leads to the pronounced shear-thinning. In contrast to it, viscosity measurements of a suspension of rigidified RBCs with a volumetric fraction of 5% show an indisputable Newtonian behaviour. The data for the latter measurements was adopted with the permission from Asena Abay of Experimental Physics group in Saarland University. The samples were pre-sheared for one minute at $\dot{\gamma} = 100 \text{ s}^{-1}$ before acquiring data. The viscosity was measured in the range of shear rate values between $0.1 - 500 \text{ s}^{-1}$ at the grid of 21 points on logarithmic scale. The experimental data was acquired while gradually increasing shear-rate. To fit the data, we used the constitutive model of Herschel-Bulkley without yield-stress. In this case, the apparent viscosity μ is:

$$\mu = m\dot{\gamma}^{n-1} \quad (4.2)$$

, where n is the flow index. and m is the consistency index. If $n = 1$, the fluid is Newtonian. In case of $n < 1$, the fluid is shear-thinning. If $n > 1$, the fluid is shear-thickening.

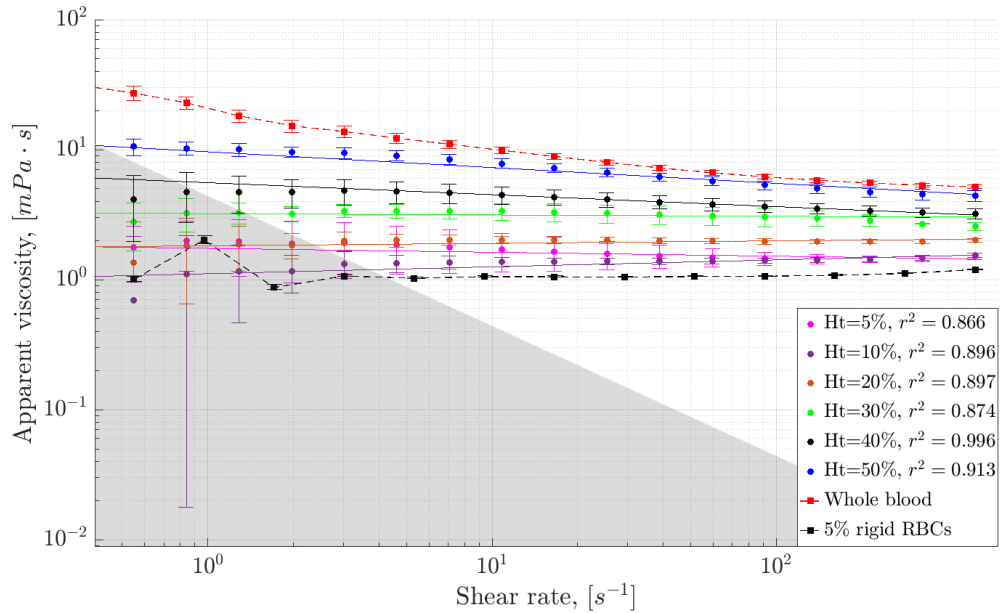


Figure 4.1. – The results of viscosity measurements of blood solutions at different hematocrits. Rheological measurements were performed for RBCs suspended in PBS. The grey area is the low-torque resolution limit of the ANTON Paar MCR 702 rheometer. The confidence intervals are evaluated for $(1 - \alpha) = 95\%$.

In Fig.4.1 are depicted the results of viscosity measurements of healthy RBCs suspended in PBS at different volumetric fraction. Taking into account the dispersion of data Equation 4.2 gives a very good fit. Even for high hematocrit level we obtain high value for parameter n (0.85 at $H_D=50\%$) which shows low shear-thinning properties of solution. The washed suspensions of RBCs at a volumetric fraction below 30% demonstrate Newtonian behaviour in a shear flow within confidence intervals. To estimate the degree of shear-thinning we compared the velocity of $H_t=50\%$ solution (washed cells in PBS) with Newtonian liquid in a cylindrical channel of $50\ \mu\text{m}$ in diameter assuming Poiseuille flow. The velocity of a shear-thinning liquid is estimated as :

$$v(r) = \left(\frac{\sigma_R}{m}\right)^{1/n} \frac{R}{\frac{1}{n} + 1} \left(1 - \left(\frac{r}{R}\right)^{\frac{1}{n}+1}\right) \quad (4.3)$$

, where n and m are parameters from Equation 4.2, R is a radius of a cylindrical channel, σ_R us a shear stress at the walls of a capillary ($\sigma_R = \frac{R\Delta P}{2L}$). The comparison of the velocity profiles is illustrated in Fig. 4.2. Both curves are depicted after normalization by a maximal velocity v_{max} for the qualitative comparison. As we can see, velocity profile of a suspension of washed RBCs even at high concentration, shows marginal deviation compared to Newtonian fluid. Based on this conclusion, we developed techniques to characterize the velocity field of a RBCs suspension in microfluidic channes, that we will described in the next section.

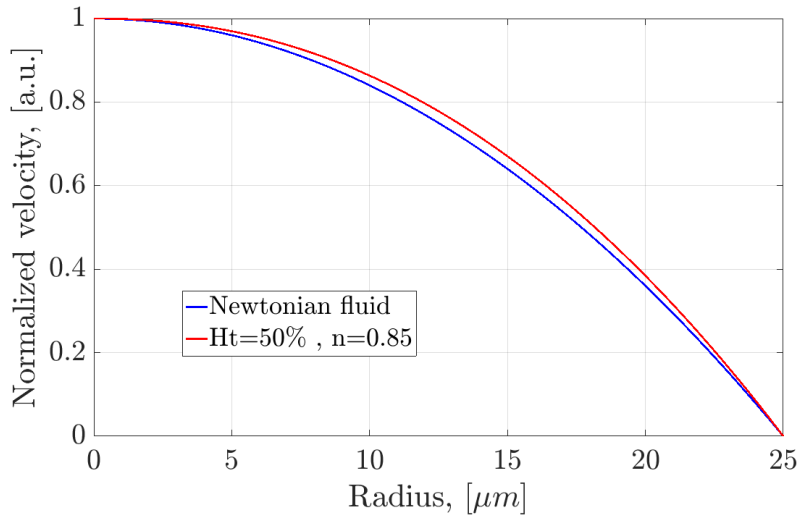


Figure 4.2. – Comparison of the velocity profiles estimated for a Newtonian and a shear-thinning fluids in a $50\ \mu\text{m}$ wide cylindrical channel. The results demonstrate that a suspension of *washed* RBCs even at 50% concentration shows very little deviation from the velocity profile of a Newtonian fluid

As was described previously in Section 4.1, for microfluidic experiments RBCs are suspended in isodense solution based on OptiPrep™. In order to quantify the rheological properties of RBCs suspension in another media, additional experiments were per-

formed. The experimental protocol for these viscosity measurements is similar to the one described in the beginning of this section. The results are depicted in Fig. 4.3. The OptiPrep™ solution demonstrates no additional shear-thinning behaviour. However, the viscosity values are slightly elevated, compared to PBS based suspensions.

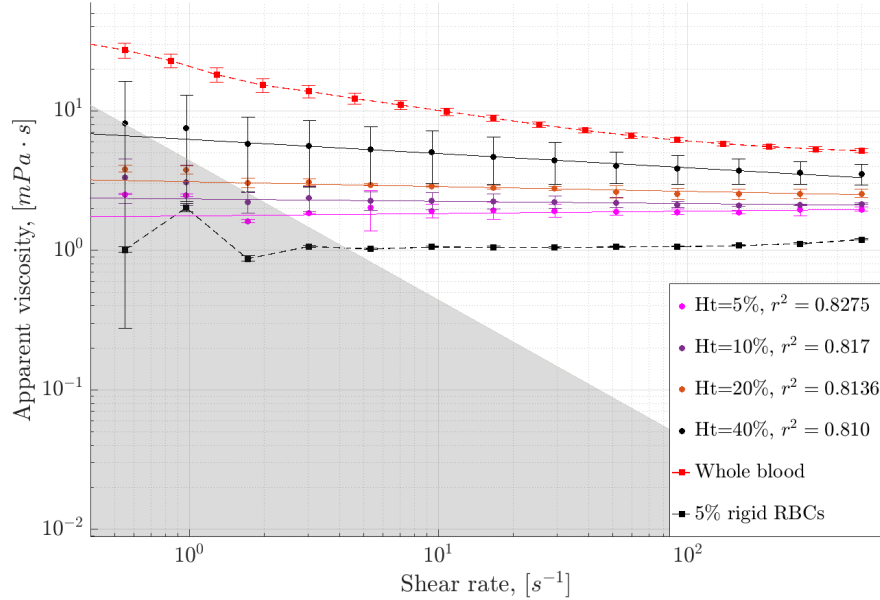


Figure 4.3. – The results of viscosity measurements of blood suspensions at different hematocrits. Rheological measurements were performed for RBCs suspended in a media, composed of 65% PBS and 35% OptiPrep™. The grey area is the low-torque resolution limit of ANTON Paar MCR 702 rheometer. The confidence intervals are evaluated for $(1 - \alpha) = 95\%$.

4.3. Velocimetry

In our margination studies, in order to describe quantitatively the cross-sectional migration of rigid RBCs away from the centerline of a channel, the distribution of stiff cells in the flow must be known. The results obtained by counting number of cells passing through the section of the microchannel do not directly reflect the density of cells, since these results are altered by velocity (higher velocity in the centre of the channel comparing to the velocity near walls leads to higher cell count). To make a correction for that, cells contribution to the final probability density function needs to be readjusted by the local velocity.

To estimate theoretically the velocity of the flow we used the model based on solution of Stokes equation in rectangular channel :

$$v_x(y, z) = \frac{4h^2\Delta P}{\pi^3\mu L} \sum_{n, odd} \frac{1}{n^3} \left[1 - \frac{\cosh(n\pi\frac{y}{h})}{\cosh(n\pi\frac{w}{2h})} \right] \sin\left(n\pi\frac{z}{h}\right) \quad (4.4)$$

, where h , w and L are the height, width and length of the microchannel, ΔP the applied pressure and μ the apparent viscosity.

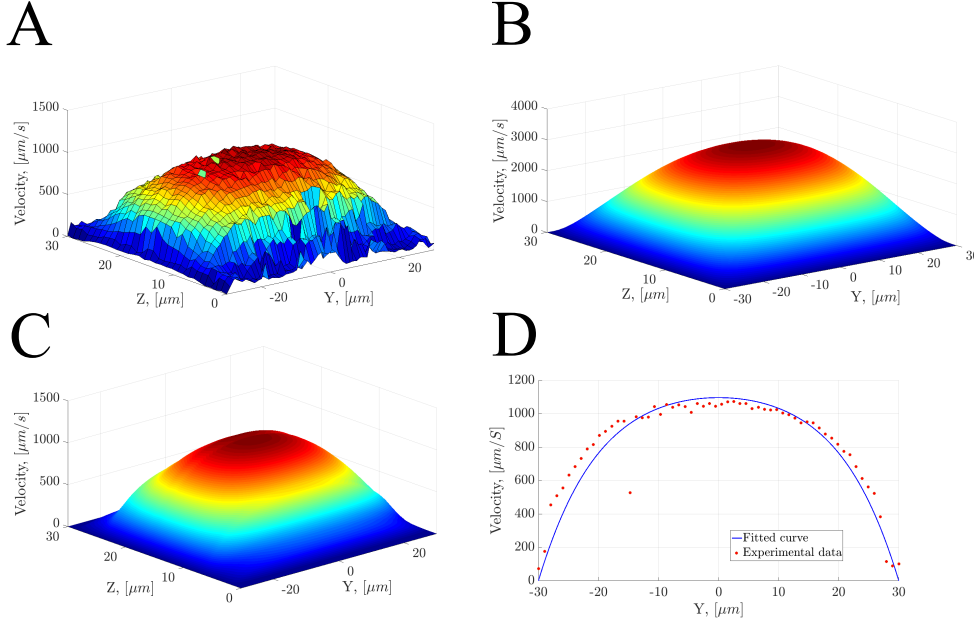


Figure 4.4. – Example of a velocity evaluation, $Ht=20\%$, $\Delta P=15$ mbars. **A** "Raw" data acquired via PTV across the section of a microfluidic channel. **B** Theoretical prediction of the velocity profile for water (viscosity $\mu = 1 \text{ mPa} \cdot \text{s}$) in the channel of given geometry. **C** Experimental velocity profile which is numerically fitted using the underlying model. **D** Single curve fitting (middle plane, $z=15 \mu\text{m}$)

Velocity is determined experimentally by tracking individual fluorescently labeled rigid cells (Fig.4.4). For that purpose, a simple custom written particle tracking velocimetry (PTV) routine was employed. In case of measurements in $30 \mu\text{m}$ high microchannels, PTV was performed at every step of piezo-motors (meaning Z direction) and then experimental results were fitted in each plane with theoretical predictions by minimizing mean squared error (MSE) using the apparent viscosity μ as a fitting parameter.

In the Fig.4.5 is given an example of MSE calculation. In each plane z_i of a microfluidic channel, the measured velocity is fitted with the theoretical prediction $v_x(y, z_i)$ defined by Equation 4.4. The minimum of $MSE(\mu)$ determines the viscosity value μ for velocity fitting in that particular z plane. The Fig.4.6 shows the viscosity values obtained via this approach. In this example, the velocity field was measured in a rectangular microfluidic channel $30 \mu\text{m}$ in height and $60 \mu\text{m}$ in width.

The viscosity values around the middle plane match the ones measured in the rheometer for the same hematocrit level. However, the z planes close to the bottom and the top of a microfluidic chamber show the elevated viscosity. The velocity is measured by tracking fluorescently labeled individual *stiff* RBCs. Close to the top/bottom of a microchannel, rigid cells may interact with the surface and get slowed down. This decrease in the

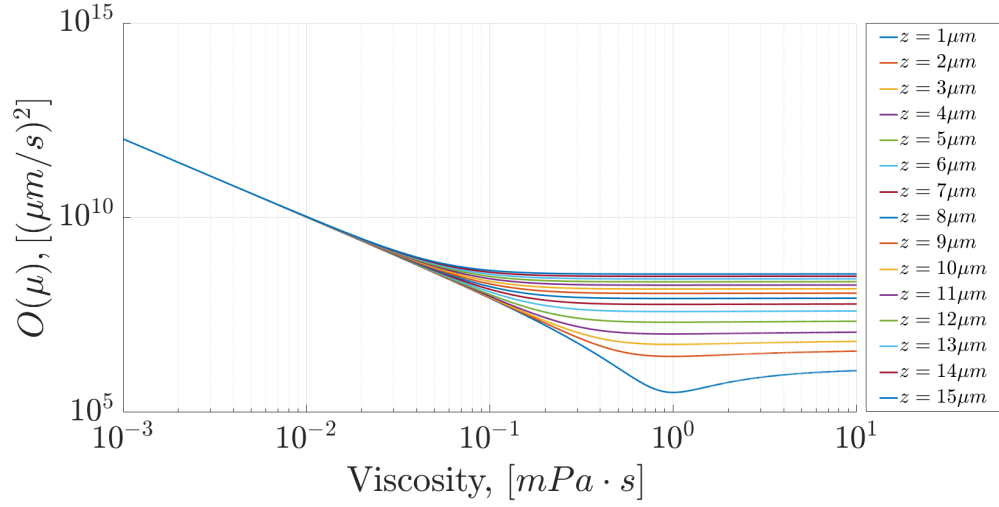


Figure 4.5. – Evaluation of an optimal value for apparent viscosity μ_a as of a fitting parameter by minimizing MSE, $Ht=20\%$, $\Delta P=15$ mbars. Figure demonstrates how viscosity is evaluated individually for different planes in Z direction from the bottom to the middle plane of microfluidic channel

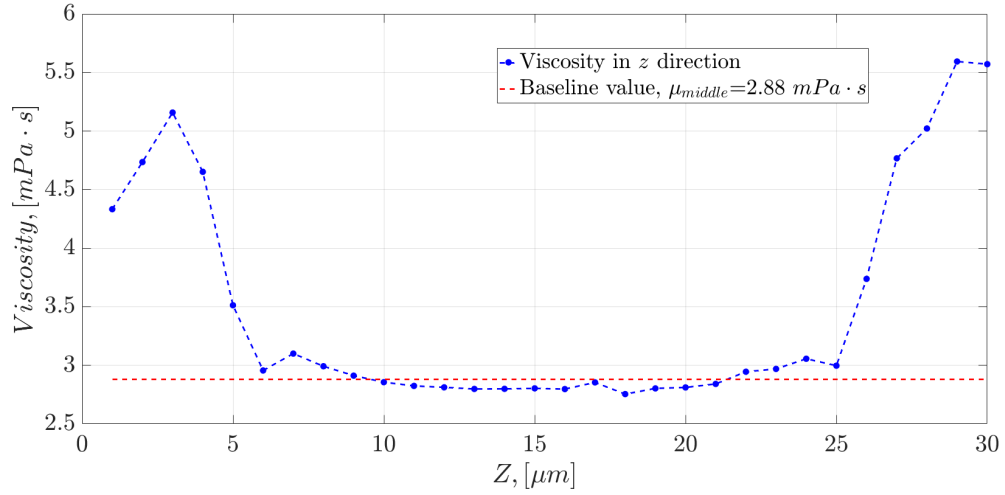


Figure 4.6. – The viscosity values along z direction obtained by minimization of MSE between measured and theoretical velocity. Example is given for the flow of RBC suspension of $Ht=20\%$ at $v_{mean} \approx 900 \mu\text{m/s}$.

mean velocity results in the overestimation of viscosity values.

To obtain a reliable measurement of cell velocity via PTV, the same cell needs to appear in the field of view at least five times. Consequently, the velocity measurement at high pressure drops requires either shorter exposure times (which, in its turn, lowers the signal-to-noise ratio) or the application of a different measurement technique. In cases, when the maximum velocity $v_x^{max} > 5000 \mu\text{m/s}$, instead of PTV we employed a technique based on the measurement of lengths of the fluorescent traces.

The relationship between the maximum velocity v_x^{max} and the mean velocity v^{mean} is defined as:

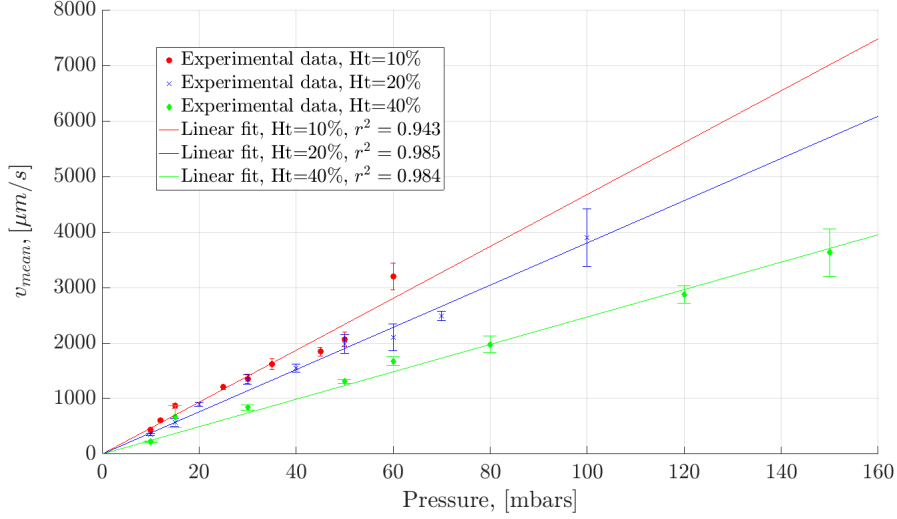


Figure 4.7. – Measured mean velocity of a blood suspension through a microfluidic chamber at different hematocrits. Cross-section of a microchannel $60 \mu\text{m} \times 30 \mu\text{m}$. Experimental data fitted according to linear law $v(\Delta P) = p_1 \cdot \Delta P$, assuming 0 velocity in the absence of driving pressure.

$$v_x^{max} = v_x\left(0, \frac{h}{2}\right) = \frac{4h^2\Delta P}{\pi^3\mu L} \sum_{n,odd} \frac{1}{n^3} \left[1 - \frac{\cosh(0)}{\cosh(n\pi\frac{w}{2h})}\right] \sin\left(n\pi\frac{1}{2}\right) \quad (4.5)$$

$$\Rightarrow v_x^{max} \approx 3.53 \frac{h^2\Delta P}{\pi^3\mu L} \quad (4.6)$$

$$Q = 2 \int_0^{\frac{w}{2}} dy \int_0^2 v_x(y, z) dz \approx \frac{h^3 w \Delta P}{12\mu L} \left(1 - 0.63 \frac{h}{w}\right) = 0.69 \frac{h^3 w \Delta P}{12\mu L} \quad (4.7)$$

$$v^{mean} = \frac{Q}{A} = 0.69 \frac{h^2\Delta P}{12\mu L} \quad (4.8)$$

$$\Rightarrow v^{mean} = v_x^{max} \frac{0.69\pi^3}{12 \cdot 3.53} \approx 0.5 v_x^{max} \quad (4.9)$$

, where the height-to-width aspect ratio of microchannel $\frac{h}{w} = 0.5$.

Fig.4.7 shows the dependence of the measured mean velocity of cells as a function of the applied pressure. The linear relation shows Newtonian properties of the suspension discussed in Section 4.2.

4.4. Image analysis in microfluidic experiments

Margination experiments, performed within the frames of this study, require an elaborate image processing. To do so, we used MATLAB™ (MathWorks, MA, USA) computing environment. Apart from the velocity calculation of labeled cells, described previously, this custom developed MATLAB software was used to evaluate the coordinates of moving cells, their distribution and to compute margination parameters.

While the behaviour of healthy and stiff cells in the flow is entirely different, they are visually indistinguishable in the bright field imaging (Fig.4.8). To calculate the velocity field in the microfluidic channel by tracking cells in the bright field is also a challenging problem, even if it is a slit channel, imitating pseudo 2D flow. To overcome this obstacle, we employed fluorescent labeling of the cells. RBCs rigidified with 1% glutaraldehyde, are fluorescently labeled with CellMask™ Deep Red Plasma membrane stain (Molecular Probes) and then added to the sample. By doing so, we can easily detect single flowing cells in a slit-like microchannels by means of conventional fluorescent microscopy, or in a rectangular duct channels, using a spinning disc confocal microscope. However, in this case healthy cells can not be detected.



Figure 4.8. – A generic representation of a RBC suspension flowing through a microchannel. **A** A bright field image of a blood solution of 10% hematocrit level flowing in 60 μm wide microchannel; exposure time 3 ms, scale bar 30 μm . **B** Snapshot of numerical simulations showing margination of stiff RBCs in a rectangular duct channel. Normal red blood cells are omitted from the figure for clarity and as an analogy to experimental visuals.

Image processing consists of two main cycles. During the first cycle of the program we estimate the average intensity value of each pixel in the field of view throughout the image sequence to calculate the background and subtract it afterwards. By calculating and subtracting the background intensity we can reveal heterogeneities of illumination and increase the signal-to-noise ratio.

During the second cycle an actual image processing is being performed (Fig.4.9). The image is smoothed by applying the Wiener filter, the contrast is increased by mapping intensity values, an erosion is performed to get rid of high intensity artifacts in the the image. At the end, the processed grey scale image is binarized. Centroids of labeled objects are calculated as they pass through an imaginary line (usually in the middle of the field of view) drawn across the channel for further evaluation of margination.

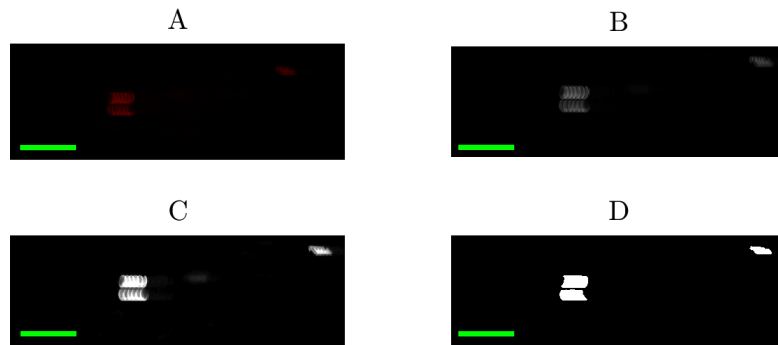


Figure 4.9. – Main steps in the image processing procedure, $H_t=10\%$, $\Delta P=12$ mbars ($v_{mean} \approx 600 \mu\text{m/s}$); the image was acquired in the middle plane of a $30 \mu\text{m}$ high microfluidic channel, scale bar $30 \mu\text{m}$. (A) The original image. (B) The cropped image after smoothing and subtracting background noise. (C) The image after erosion and mapping intensity values. (D) The binarized image used for cell detection.

4.5. Characterization of red blood cells with atomic force microscopy

In order to quantify the rigidity contrast between two sub-populations of RBCs in margination experiments we employed AFM (Fig.4.10). The effective Young's modulus of cells was measured through the recording of force–distance curves. AFM measurements were performed in a liquid environment (PBS) using a JPK Nanowizard 3 setup coupled to an optical microscope.

The data were acquired from a small circular zone at the highest points and in the center of a cell in order to exclude artifacts related to the motion of a cell and the interaction with a substrate.

4.5.1. Characterization of rigid cells

We investigated the rigidity of RBCs rigidified with a cross-linking agent (gluteraldehyde). Cells were fixed (rigidified) with a range of gluteraldehyde concentrations in order to quantify the dependence of cells' rigidity on the cross-linking agent. The variety of cantilevers with various nominal spring constants as well as different indentation forces were tested in order to find proper measurement conditions for each gluteraldehyde concentration. Prior to the measurements cells were immobilized on a substrate with an adhesive protein (CellTak). Force mapping was performed for 3-5 cells of each population on a grid of 32×32 points, corresponding to $10 \mu\text{m} \times 10 \mu\text{m}$ map (Fig.4.11). Force-distance curves were acquired at the indentation rate of $5 \mu\text{m/s}$. Curves were analysed according to Hertz model, implemented in JPK software. The Poisson ratio was set

4.5. CHARACTERIZATION OF RED BLOOD CELLS WITH ATOMIC FORCE MICROSCOPY

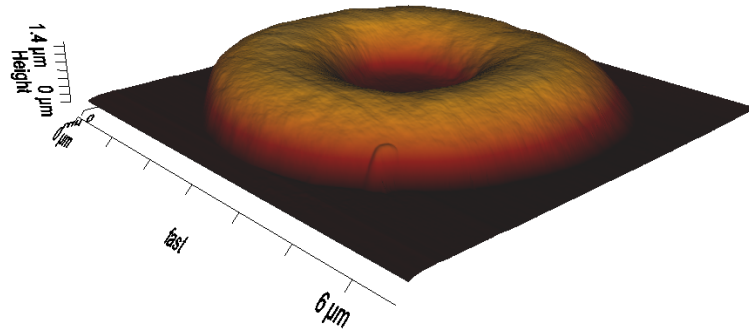


Figure 4.10. – Image of a RBC by means of atomic force microscopy. The cell was fixed in 1% of glutaraldehyde and immobilised on a substrate with an adhesive protein (Corning™ Cell-Tak, BD Biosciences). The image was taken in contact mode on the grid of 1024×1024 pixels over $9 \mu\text{m} \times 9 \mu\text{m}$ square area.

to 0.5.

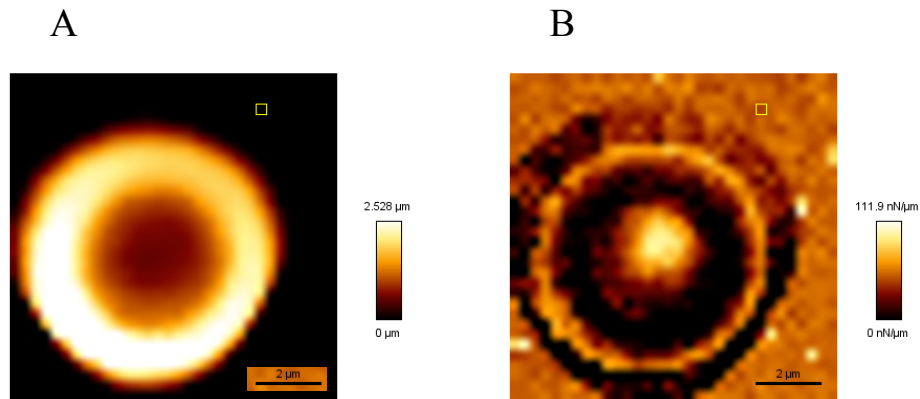


Figure 4.11. – Result of AFM force mapping of a RBC rigidified in 1% glutaraldehyde. Data were acquired in PBS solution, the nominal spring constant of the cantilever is 0.6 N/m, the set-point force is 1 nN. **A** Set-point height. **B** Slopes of force-displacement curves

Additionally to the statistical variation of results, the outcome of AFM measurements depends highly on parameters of the experimental setup (cantilever spring constant and set-point force value). In case of rigidity measurements, these parameters had to be adopted for cells with different rigidities. This brings inconsistency in the analysis of results, which could signify, that in our case, the classic force-distance mapping of a cell is not an optimal approach for quantitative analysis of cells rigidity. Qualitatively, however, our results demonstrate a significant rigidity contrast between healthy RBCs and erythrocytes treated with 1% of glutaraldehyde. Cells fixed at such concentration can be considered as non-deformable solid objects in our microfluidic experiments in comparison to healthy RBCs.

4.5.2. Characterization of healthy cells

When a force curve is measured on a hard substrate (like glass), the cantilever deflection is proportional to the relative sample position resulting in a linear slope in the part of the curve for which the tip and the sample are in contact. When soft samples like erythrocytes are investigated, the recorded cantilever deflection as a function of the relative sample position is not linear due to RBC deformation (Dulińska-Molak, Targosz, Strojny, et al. 2006).

The calculated value of Young's modulus can vary as a function of the indentation depth. To avoid the effect of a substrate over which cells are placed it is recommended to indent the sample during AFM measurements at a distances lesser than 10% of the total thickness of the specimen (Dimitriadis, Horkay, Maresca, et al. 2002). However, according to our results the theoretical curve fits the experimental data for larger distances (Fig.4.12).

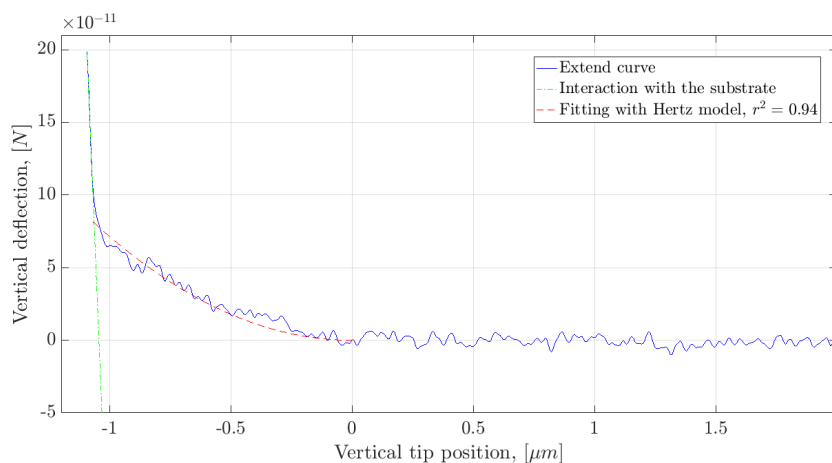


Figure 4.12. – Force-distance curve illustrating the interacting force between cantilever tip and healthy RBC in PBS solution, the nominal spring constant of the cantilever is 0.01 N/m, the set-point force is 0.3 nN.

The force-distance mapping of healthy RBCs was performed with the same experimental protocol as rigid cells. It is possible that immobilization of healthy RBCs on a substrate with CellTak could result in a residual stress on the cell membrane. Nevertheless, within the limits of the qualitative comparison of fixed and healthy cells it is a justified assumption to consider this effect negligible.

The Fig.4.13 shows the combined results of AFM measurements for rigid and healthy RBCs. In this figure, five histograms, based on the accumulative data from 3-5 cells for each populations, represent the distribution of rigidity values in healthy and fixed cells. From these results, we can conclude, that RBCs fixed in 0.1-1% of glutaraldehyde can be regarded as solid objects compared to healthy RBCs. Surprisingly, the increment of rigidity seems to be controllable by treatment with the low concentrations of glutaraldehyde. However, highly dispersed and overlapping distributions of cells rigidities make

4.5. CHARACTERIZATION OF RED BLOOD CELLS WITH ATOMIC FORCE MICROSCOPY

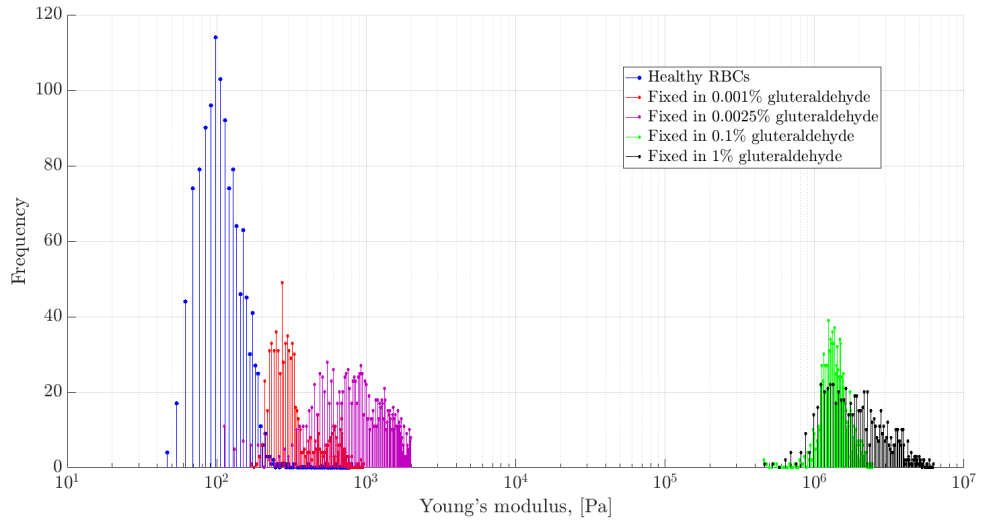


Figure 4.13. – Results of AFM measurements demonstrate considerable contrast in rigidity between healthy RBCs and cells fixed in 0.1 – 1% of glutaraldehyde.

it complicated to create two sub-populations with low contrast of stiffness. Because of that we restrained our margination studies to the case in which marginating cells can be considered as non-deformable. The dependence of margination on the varying rigidity contrast is not covered in this work.

5. Characterization of individual red blood cells at equilibrium state

Several blood disorders are correlated with alterations of RBCs shape. The analysis of cell morphology can be used as a diagnostic tool for these diseases. However, the existing classification is qualitative and requires tedious verification by hand. The transitions on SDE sequence (see Section 2.1.1) occur continuously and a manual classification between several distinct cell classes does not allow an operator to account small morphological transformations. In the following chapter we describe an approach for 3D cell shape recognition of RBCs in stasis. The verification of cell shape types was implemented by an artificial neural network (ANN). The ANN was trained to recognize three distinct shapes of healthy RBCs (further referred to as *main shapes*): spherocytes, discocytes and echinocytes type III (see Fig. 4.10). Intermediate states were defined as a superposition of the main RBCs shapes. As input vectors for ANN we used Fourier spectra of cells. This makes the technique invariant against translations, rotations and size variation of the cells and allows for a continuous unbiased classification. The Fourier analysis was performed for 3D volume data based on confocal image stacks. To significantly decrease the amount of processed data, 3D Fourier images of cells were downgraded to one dimensional vector via spherical integration. We demonstrate that an averaged spectrum of RBC contains all the essential features for the proper verification of a cell shape.

This study was carried out in collaboration with other researchers from Saarland University. Confocal imaging of fixed RBCs for their later morphological analysis was carried out by Greta Simionato and these images are included in the present manuscript with her kind permission. The innovative method for 3D shape recognition of microscopic objects was proposed by Dr. Stephan Quint and was implemented under his supervision.

Plusieurs maladies du sang sont en corrélées avec des altérations de forme des globules rouges. L'analyse de la morphologie des cellules peut être utilisé comme un outil diagnostique de ces maladies. Néanmoins, la classification actuel est qualitative et nécessite une pénible vérification à la main. Les transitions SDE (voir la Section 2.1.1) se produisent de manière continue et la classification manuelle entre les différentes classes de cellules distinctes ne permet pas à un opérateur de compter les petites transformations morphologiques. Dans le chapitre suivant, nous décrirons une approche pour la classification des globules rouges en 3D au repos. La vérification des formes des cellules a été réalisé par un réseau de neurones artificiels (ANN). ANN a été entraîné pour reconnaître trois formes distinctes de globules rouges saines: spherocytes, discocytes et echinocytes de type III (vois Fig. 4.10). Les états intermédiaires ont été définis comme une super-

position des formes principal des globules rouges. Nous avons utilisé le spectres Fourier des cellules comme les données d'entrée pour l'ANN. Cette approche a l'avantage d'être indépendant par rapport aux translations, rotations et variation de la taille des cellules et permet de classifier les formes des cellules en continu. L'analyse spectrale a été réalisée à partir des images confocales. Pour faciliter le traitement des données, les spectres 3D des cellules ont été réduites à des vecteurs 1D via l'intégration sphérique. Nous démontrons que les spectres moyennes contient toutes l'information essentielle pour la vérification de formes des cellules.

Cette étude été réalisé en collaboration avec les autres chercheurs de l'Université de Saarland. Les images confocales des globules rouges fixées pour l'étude morphologique ont été pris par Greta Simionato et sont utilisés dans cette manuscrit avec sa permission. Le concept novateur de reconnaissance de formes des objets 3D microscopiques a été proposés par Stephan Quint et été réalisé sous son direction.

Mehrere Bluterkrankungen hängen mit der Veränderung der Form roter Blutkörperchen zusammen. Die Analyse der Zellmorphologie kann als Analysemethode für diese Krankheiten genutzt werden. Jedoch ist die existierende Klassifikation qualitativ und verlangt eine umständliche manuelle Verifikation. Die Übergänge von SDE-Sequenzen (siehe Abschnitt 2.1.1) treten kontinuierlich auf und eine manuelle Klassifikation zwischen mehreren verschiedenen Zellklassen erlaubt es dem Beobachter nicht, kleine morphologische Veränderungen zu erkennen. Im folgenden Abschnitt wird eine Methode zur 3D-Zell-Erkennung roter Blutkörperchen in Kanälen beschrieben. Der Nachweis der Zellform-Klassen wurde mittels eines artifiziellen, neuronalen Netzes (ANN) vorgenommen. Das ANN wurde darauf trainiert, drei verschiedene Typen gesunder roter Blutkörperchen zu erkennen: Sphärozyten, Discozyten und Echinozyten Typ III (siehe Abbildung 4.10). Zwischenzustände wurden als die Überlagerung der drei Formern der Hauptzustände roter Blutkörperchen definiert. Als Eingangsvektor für das ANN nutzten wir das Fourier-Spektrum der Zellen. Das macht die Technik invariant gegenüber Verschiebungen, Rotationen und der Größenvariation der Zellen und erlaubt eine kontinuierliche, unvoreingenommene Klassifikation. Die Fourier-Analyse wurde für 3D-Volumen-Daten basierend auf den konfokalen Bilderstapeln durchgeführt. Um die Menge der bearbeiteten Daten signifikant zu verringern, wurden die 3D-Fourier-Bilder der Zellen durch sphärische Integration zu einem eindimensionalen Vektor reduziert. Wir konnten zeigen, dass ein gemitteltes Spektrum roter Blutkörperchen genug wesentliche Merkmale zur genauen Feststellung der Zellform besitzt.

Diese Studie wurde in Zusammenarbeit mit anderen Forschern der Universität des Saarlandes durchgeführt. Die Aufnahme der Bilder fixierter roter Blutzellen durch das Konfokalmikroskop für die spätere morphologische Analyse wurde durch Greta Simionato durchgeführt und die entsprechenden Bilder wurden netterweise durch ihre Er-

laubnis in das aktuelle Manuskript aufgenommen. Die innovative Methode zur 3D-Formbestimmung mikroskopischer Objekte wurde von Stephan Quint vorgeschlagen und unter seiner Aufsicht implementiert.

5.1. Theoretical support

In past decades, multiple studies were dedicated to RBCs morphology in stasis and in flow ((Tse and Lux 1999), (Park, Best, Badizadegan, et al. 2010), (Du, Diez-Silva, Kato, et al. 2015), (Dong, Chadwick, and Schechter 1992), (Lanotte, Mauer, Mendez, et al. 2016b), (Alaarg, Schiffelers, Solinge, et al. 2013)) in order to understand the role of RBCs shapes in physiological conditions as well as in disease. The detailed 3D analysis of cell morphology could be crucial for the diagnosis and treatment of blood disorders that are accompanied by RBCs shape change. In this study we focus on RBC shapes at stasis in contrast to different RBC shapes occurring in flow (Lanotte, Mauer, Mendez, et al. 2016b, Quint, Christ, Guckenberger, et al. 2017). Several techniques have been already proposed for the automated classification of RBCs shape (M. Xu, Papageorgiou, Abidi, et al. 2017, Kriegel, Köhler, Bayat-Sarmadi, et al. 2017). In our study we use confocal microscopy to image cells with a higher resolution and a superior border definition compared to bright field microscopy. We developed an ANN that identifies different cell shape types based on the radially averaged Fourier image of 3D confocal stacks. The main limitation of the employed ANN is a sufficient data set required for the learning process of the network. This dataset is composed of manually retrieved 3D stacks of single RBCs.

The concept of neural networks emerged from the studies of artificial intelligence, more precisely, in an attempt to recreate the ability of biological neural systems to learn by modeling low level structure of a brain (Patterson 1996). A brain is composed of a large number of neurons, interconnected by numerous liaisons, capable of transmitting electro-chemical signals. A neuron gets activated when a cumulative signal transmitted from neighboring cells overcomes a certain level (activation threshold). The intensity of a signal, received by a neuron (and, consequently, the potency of a neuron to be activated), depends on the activity of synaptic connections. In Hebb 1949 is suggested, that the learning process first of all consists in the adaptation of the potency of these synaptic junctions. In order to reflect the substance of its biological prototype, the artificial neuron is defined as:

1. The neuron receives multiple signals through several channels, each with its own activity (or *weight*).
2. Each neuron is assigned to its threshold. The weighted sum of the channels, entering a neuron, deducted by this threshold defines its activation (also know as *post-synaptic potential* or PSP).

3. The input signal is further transformed via an *activation function* resulting in the output signal.

This is a description of a single artificial neuron. The ANN is organized in layers. The architecture of the ANN used in this study is illustrated in the Fig.5.1. The first layer receives the input data. For the neurons of this layer $input=output$. After that the information is received by the neurons of the *hidden* (because it is an intermediate layer, a "black box", which has no interface with the end user) layer, (usually not more than three, one layer in our case). The non-linear information processing is conducted in this layer. Before leaving the node of this layer, the weighted sum of inputs is passed through a nonlinear mathematical function called a *sigmoid*. The outputs of the nodes in a hidden layer are applied to the output layer, consisting of one single neuron (in our case), to produce a sole final value.

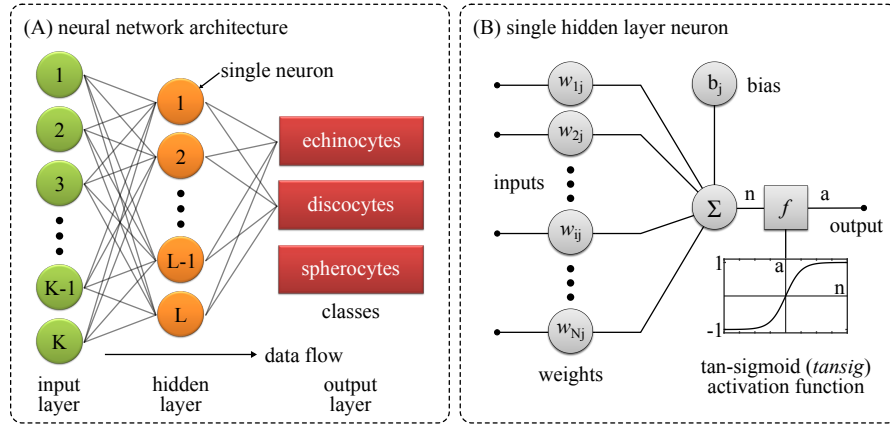


Figure 5.1. – Schematic representation of an ANN and a single neuron. **(A)** Artificial neural network architecture. The K input layer neurons are fully interconnected with the L neurons from the hidden layer. While the input layer serves as buffer for input data only, hidden layer neurons perform the non-linear information processing via *tan-sigmoid* activation function. The hidden layer is fully connected with the linear output layer. **(B)** Single hidden layer neuron architecture. The activation function is bounded within a range of $(-1,1)$.

The purpose of an ANN is to predict target values from input variables by processing a high dimensional input vector (\mathbb{R}^M) and mapping the result onto a low dimensional output space (\mathbb{R}^N with $N \ll M$). Based on the format of outputs, machine learning algorithms can be divided in two popular types: classification and regression. Classification algorithms are helpful when the desired answer to a problem falls under a finite set of possible outcomes: an object either belongs to a certain class or not. If the answer to a problem can not be confined to a finite number of possible classes and the outcome is meant to be continuous regression algorithms are used.

RBCs can take a spectrum of shapes on the SDE scale. To incorporate multitude of possible shapes into the output of neural network, we used a regression based classifi-

cation ANN. Different shapes from SDE sequence are mapped onto a linear scale where echinocytes correspond to a value of -1 , discocytes to 0 , and spherocytes to $+1$. Every number in between corresponds to a certain intermediate shape and we will show how it can be represented as a superposition of the neighboring extreme shapes.

As the input layer serves as a buffer for the input data, the number of neurons in it corresponds to the size of an input vector. The total number of neurons in the input and hidden layers determines the degrees of freedom of the system. The weight vector \vec{w} of the whole network is defined here as:

$$\vec{w} = \left(\dots, w_{1,j}^{(l)}, w_{2,j}^{(1)}, \dots, w_{i,j}^{(l)}, w_{i+1,j}^{(l)}, \dots, w_{N_{l-1},j}^{(l)}, \dots \right). \quad (5.1)$$

where $w_{i,j}^{(l)}$ is the weight factor of a connection between a neuron i in the $(l-1)$ th layer and a neuron j in the l th layer.

Assuming a full interconnection and $\vec{w}^{(l,j)}$ to be the weight vector of the j th neuron in the l th hidden layer, the input data is forward propagated through the hidden layers as follows:

$$z^l = \sum_{i=1}^{N_{l-1}} w_i^{(l,j)} x_i^{(l-1)} \quad (5.2)$$

The dot product z^l of the input data $\vec{x}^{(l-1)}$ and weights $\vec{w}^{(l,j)}$ (note that output from the $l-1$ hidden layer serves as an input data for l layer) from Equation 5.2 is being fed to the activation function f (Equation 5.3). For our purposes, f corresponds to a linear activation function in the input and output layer, and to a standard logistic (*tan*-sigmoid) function in the hidden layer. If the activation function in the hidden layers is linear, than no matter how many neurons and/or layers are used, the final out put is simply a linear combination of the input data. Ergo, the system is not able to solve non-linear problems like pattern recognition. Step-function has no useful derivative and because of that backpropagation learning algorithms couldn't be applied.

$$f_{\text{tan-sigmoid}} = \frac{2}{1 + e^{-2n}} - 1. \quad (5.3)$$

The ANN, employed in this study, consists of three layers: one input layer (256 neurons), one hidden layer (50 neurons), and one output layer (1 neuron).

5.2. Experimental support

5.2.1. Confocal imaging

The 3D images of RBCs were recorded by means of confocal microscopy. Labelled cells were placed in between two glass slides and visualised with a 60X objective (CFI Plan Apochromat Lambda 60X Oil, NA = 1.4, Nikon, Tokyo, Japan) mounted on an

inverted microscope (Nikon Eclipse Ti). A solid state laser ($\lambda = 647$ nm, Nikon LU-NV Laser Unit) was used as a light source for imaging. The 3D volume data was acquired via confocal z -stack scanning (CSU-W1, Yokogawa Electric Corporation, Tokyo, Japan) of samples in the range of $20\ \mu\text{m}$ at 300 nm step of piezo motors. Image sequences are acquired with a digital camera (Orca-Flash 4.0, Hamamatsu Photonics, Hamamatsu City, Japan).

5.2.2. Manual classification

In order to choose cells properly for training and for further testing the ANN, RBCs needed to be manually classified first. According to captured images, the cells were assigned into three main categories: (1) discocytes, meaning clear biconcave and symmetric discs; (2) sphero-stomatocytes, i.e. spherical cells; (3) echinocytes type III, meaning cells with more than 25 lobes. The cells that didn't fit the descriptions of these groups were classified as intermediate shapes and separated into two groups: one for stomatocytes type I and II and another for echinocytes type I and II.

5.2.3. Image processing and Fourier analysis

In order to compensate for the difference in resolution in x - y ($0.11\ \mu\text{m}/\text{px}$) and z directions ($0.3\ \mu\text{m}/\text{px}$), we adapted the scale in Z using a linear interpolation. The processed z -stack after that has the dimensions of $100\ \text{px} \times 100\ \text{px} \times 185\ \text{px}$ (XYZ).

Due to this large number of data points per cell, we pre-process our data to a reasonable extent by only taking the main features of cells into account. Making use of such procedure (Dosovitskiy, Springenberg, and Brox 2013; Krell and Kim 2017) yields some major benefits. This procedure includes:

1. Subtracting the mean intensity
In order to reduce background noise from the data, from each picture of a Z -stack we subtracted its mean intensity value and then re-mapped the intensity values.
2. Zero-padding the initial volume data
The Z -stack of $100\ \text{px} \times 100\ \text{px} \times 185\ \text{px}$ is "fit inside" a $256\ \text{px} \times 256\ \text{px} \times 256\ \text{px}$ blank picture.
3. 3D fast Fourier transform (FFT) and applying a high pass filter.
We shift the analysis from spacial to frequency domain and consider the spectral components of the volume data (Equation 5.4). We take into account only the magnitudes of a Fourier image $|F(u, v, q)|$ (Fig.5.2), and doing so allows us to work with the data invariant against XYZ-translations since phase information is ignored.

$$F(u, v, q) = \int_{-\infty}^{+\infty} \int_{-\infty}^{+\infty} \int_{-\infty}^{+\infty} f(x, y, z) e^{-j2\pi(ux+vy+qz)} dx dy dz, \quad (5.4)$$

Filtering the 3D image of a cell allows us to intensify transitions of contrast in the

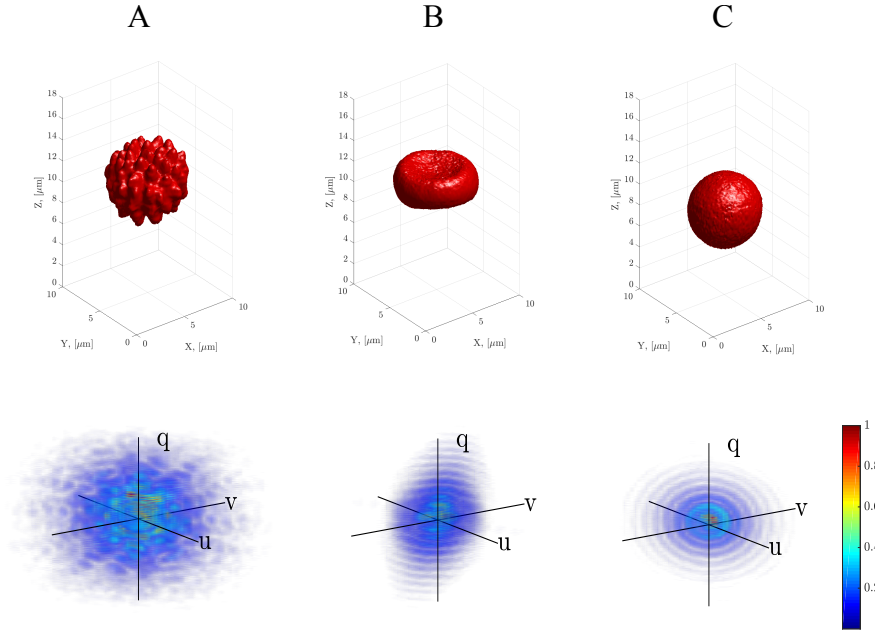


Figure 5.2. – Main shapes of RBCs, reconstructed from confocal images, and magnitudes of their corresponding 3D Fourier images. The spectra magnitudes are plotted in the Cartesian coordinate system, where the axes (u, v, q) are normalized spatial frequencies. **A** Echinocyte. **B** Discocyte. **C** Spherocyte.

image. It highlights the information of the contour of the cell and suppresses low frequencies in the image (e.g. offset). On the basis of homogeneity of spectral components within the passband, the second order Butterworth filter was chosen. In the complex frequency space the transfer function of the low-pass filter is defined through normalized coefficients as:

$$H(s) = \frac{1}{s^2 + \sqrt{2}s + 1}, \quad (5.5)$$

, where $s = j\omega$ is a complex frequency. This transfer function is used as a prototype to create a required high-pass filter $H(p)$ by assigning $p = \frac{\omega_c}{s}$, where ω_c is a cut-off frequency. After that, this transfer function is interpolated in spherical coordinates to create a 3D spacial high-pass filter $H(u, v, q)$. We applied a FFT to the zero-padded confocal Z-stack and multiply its Fourier image $F(u, v, q)$ by the transfer function $H(u, v, q)$.

4. Spherical integration of the spectral 3D images and obtaining a 1D data series for evaluation and training,

The spherical integration leads to further invariance against any rotations of the image stack since the dimensionality is reduced to a 1D spectrum.

The FFT of the confocal volume data results in a 3D matrix of complex numbers containing 256^3 data points. Due to the fact, that data points are located in the

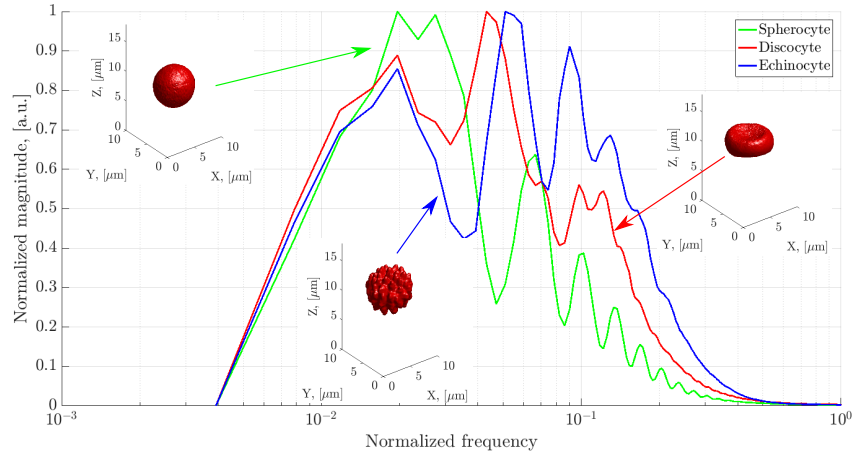


Figure 5.3. – Representative example of the spherical averaged 1D spectrum magnitude of the three RBC classes. Spherocytes (green) are radial symmetric and show a sinc-like behavior in the frequency domain with clearly pronounced maxima and minima. Discocytes (red) show a similar behaviour. However, due to their elliptic form, the spectrum is shifted towards higher frequencies compared to spherocytes. Echinocytes (blue) significantly differ from the other types. Their spiculated surface leads to a wide range of spectral components which slowly decreases.

grid of a finite size, the 'spherical integration' requires a non-trivial numerical method (Fig. 5.4). All the elements of Cartesian lattice that are located at the same euclidean distance from the center of a 3D matrix should be summed up. Those elements could be visualised as lying on a surface of sphere. For each sphere a different number of data points, allocated equidistantly from its center, exist (Fig. 5.5).

The Cartesian grid containing 256^3 data points provides us with 21027 different radii values (possible spheres of different radii). That means that 3D Fourier spectrum downgraded after spherical integration into 1D results in a vector of 21027 elements. To reduce the length of an input vector and by doing so to decrease the degrees of liberty of the ANN, the obtained one-dimensional spectrum is pooled to a histogram with 256 equidistant bins.

This procedure is applied to each cell. The resulting spectra are used as input data for the ANN. Our data pre-processing procedure results in a significant reduction of dimensionality. However, as we will demonstrate further, radially averaged spectrum magnitude is sufficient to express the substantial differences between different types of cells (Fig. 5.3). As the shape of an RBC changes from spherical to spiculated echinocyte, the average spectral magnitude gets enriched with high frequency components and a distinction between these categories becomes possible.

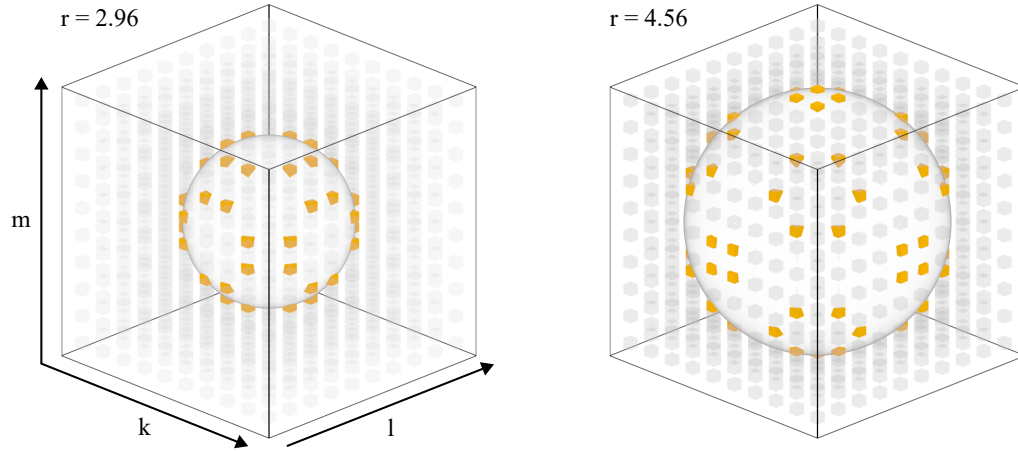


Figure 5.4. – Schematic representation of the idea behind spherical integration. Elements of the 3D matrix that have the same radius vector are coloured in yellow. As the size of a sphere increases the number of elements lying on its surface grows quadratically.

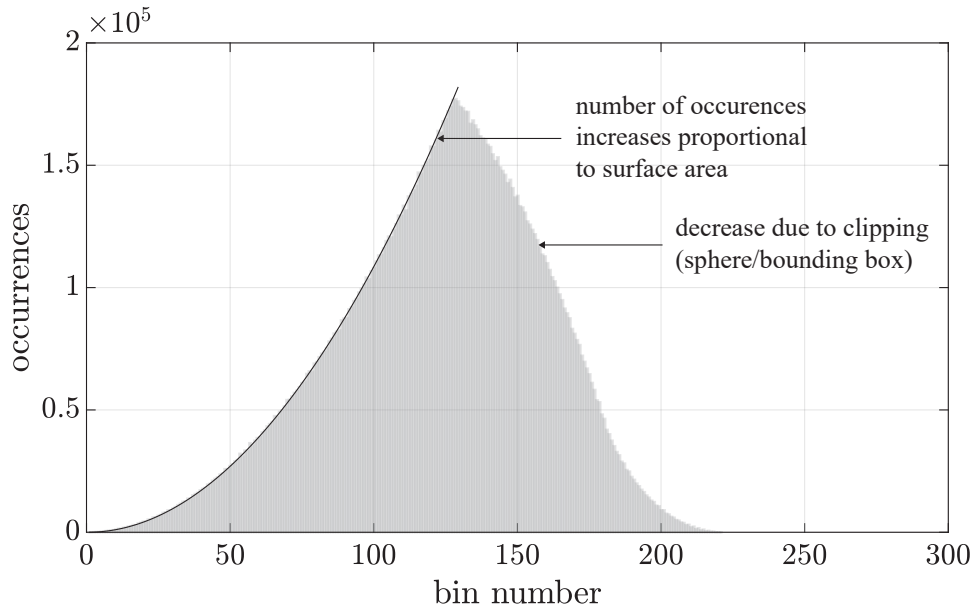


Figure 5.5. – Histogram showing the number of data points in a lattice of the size $256 \times 256 \times 256 \text{ px}^3$ occurring at different radii. The histogram is plotted against radius vector values gridded over 256 points.

5.2.4. Training of artificial neural network

Once a sufficient amount of 3D confocal scans of various RBCs shapes was acquired, we proceeded with the training of the ANN (Fig.5.6). The most important part using

5.2. EXPERIMENTAL SUPPORT

ANNs is the amount and composition of training data for the learning process of the system. For the present study, we retrieve the training data out of 100 cell stacks of the main cell shapes.

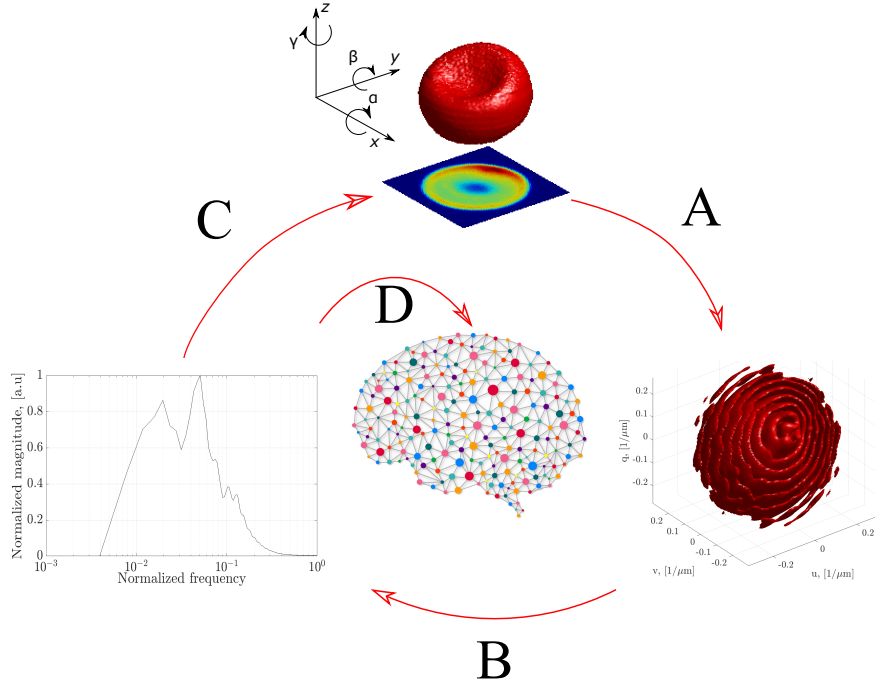


Figure 5.6. – Creation of a training data set elaborated on an dicsocyte. **(A)** FFT and applying high pass-filter to the Fourier image of a cell. **(B)** Spherical integration of a spectral magnitude (depicted in logarithmic scale). **(C)** Each new cell to be introduced to the ANN is positioned differently (slight rotations around axis) but our approach is robust against these rotations. **(D)** The obtained data-vector has a length of 256 and serves as an input for the ANN.

The training data for the intermediate cell shapes are obtained via superposition of the main shape cells spectra. We created a grid with "additional" five intermediate shapes on the SDE scale by mixing neighboring main shapes in corresponding proportions. For example, if a discocyte is assigned to "0" and a spherocyte is assigned to "1", then a first type stomatocyte is assigned to 0.1667 and the training data for such type is created as:

$$ST_1(f) = 0.1D(f) + 0.9S(f), \quad (5.6)$$

, where $ST_1(f)$ is a spectrum of a new type, $D(f)$ is a spectrum of a discocyte, $S(f)$ is a spectrum of a spherocyte and f is a normalized spacial frequency.

During the initialisation of the ANN, the weights and bias factors are randomly chosen. Aside from a sufficient amount of appropriate training data, also an optimization algorithm is mandatory to let the free parameters of the ANN converge to a state for which the performance function is minimized. As performance or cost function we use

5.3. RESULTS OF RED BLOOD CELL SHAPE CLASSIFICATION BY MEANS OF ARTIFICIAL NEURAL NETWORK

the mean squared error (MSE) which is calculated according to

$$\text{MSE} = \frac{1}{N} \sum_{i=0}^{N-1} (e_i)^2 = \frac{1}{N} \sum_{i=0}^{N-1} (t_i - a_i)^2, \quad (5.7)$$

where t_i denotes the target value of each cell, and a_i the actual system answer.

Our ANN uses Levenberg-Marquardt backpropagation algorithm for updating weight and bias values, i.e. the learning process (Equation 5.8).

$$w_j(k+1) = w_j(k) - [J^T J + \mu E] J^T e \quad (5.8)$$

Here w_j is a weigh vector of a j -neuron in the hidden layer, k is a an iteration, J is the Jacobian matrix that contains first derivatives of the network errors with respect to the weights, E is a unity matrix and e is a vector of network errors. The adaptive value μ is linearly increased by a certain value (10 by default) until its further increment does not result in a reduction in performance. In that case it's reduced (by 0.1 in each iteration).

The training data is randomly split into three parts:

1. A training data set (70 %) which is used to minimize the gradient of the cost function.
2. A validation data set (15 %) which is used to stop the training process if the network performance on the validation vectors fails to improve or remains the same for several iterations in a row.
3. A test data set is used (15 %) for system benchmarking but does not have any effect on training.

While training the system we passed the training data to the network and observed a continuous descend of the cost function. A premature abort due to the stagnation of the learning precess occurred at 128th iteration. The performance of the training process is shown in Fig 5.7.

5.3. Results of red blood cell shape classification by means of artificial neural network

Fig.5.8 demonstrates an output of trained ANN to new data. Qualitatively, the results reflect our initial assumptions and are in accordance with our expectations. Main RBCs shapes, i.e. echinocytes, discocytes and spherocytes, are grouped around their pre-trained positions on the SDE scale. Intermediate shapes, such as echinocytes type I and II and stomatocytes, are allocated in between main shapes. This result proves the idea, that intermediate shapes can be represented as a superposition of main RBCs shapes.

However, the output distributions of ANN are very broad. It makes such automated classification technique unreliable for practical applications. Nevertheless, as *prove of concept*, we demonstrated the potential of this approach. Improvement of the classification can be achieved by *tuning* parameters of ANN (number of neurons, activation

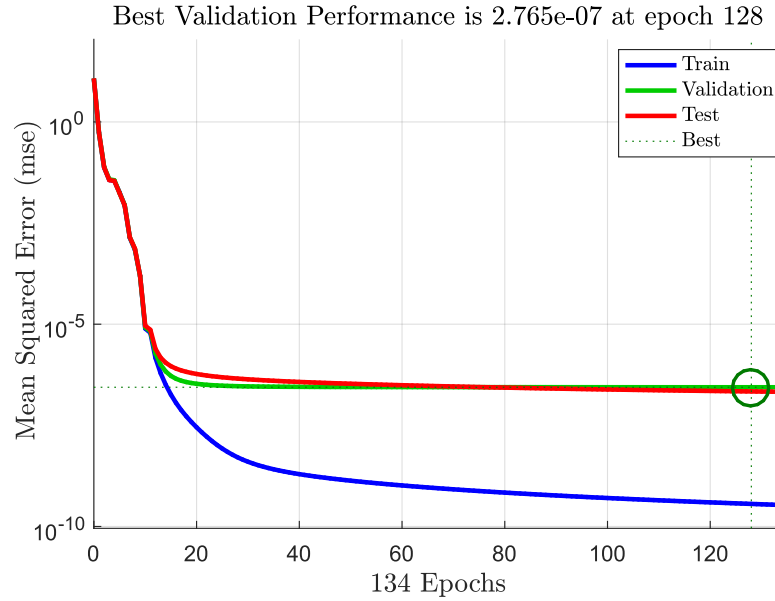


Figure 5.7. – Training performance of the ANN with respect to the number of training epochs.

function, learning algorithm and etc.), notably, its training process (using larger training base).

Our results show that a system based on the presented concept can be a alternative to the manual classification. Besides a more precise cell shape verification, our technique is highly time-effective and relinquishes a possible human error caused by any manual intervention into the process of data evaluation.

5.4. Classification of red blood cells using self-organizing map

In order to understand, whether it is possible to classify RBCs shapes, using their averaged 3D Fourier spectra, without any predisposed knowledge about cell type, we employed another type of neural network. Self-Organizing Map (SOM) is a data-analysis method that produces low-dimensional projection images of high-dimensional data distributions, in which the similarity relations between the data items are preserved. In other words, it is able to cluster the data, but at the same it orders the clusters (Kohonen 2014). This neural network undergoes unsupervised competitive learning, meaning finds similarities between vectors in the input data space without initial training (Kohonen 2001, Kohonen 2014).

A SOM is either a planar or linear type of neural network usually consisting of a single layer. Despite the fact, that a SOM creates a 2D projection of a high-dimensional input data, the map itself does not have to be a rectangular sheet. Since the examined physical problem suggests the solution to be a linear scale (SDE scale), the architecture

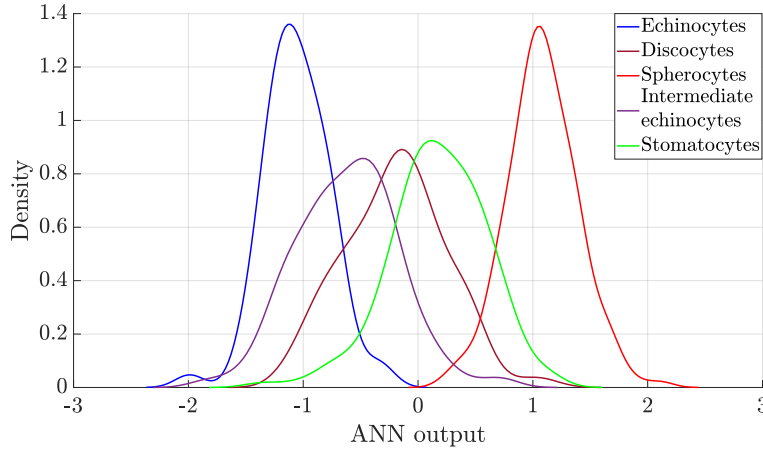


Figure 5.8. – Classification of RBCs shapes using ANN.

of the SOM is here based on a linear array. Our network consists of 1×21 neurons which are localized on a equidistant grid. Each neuron is fully connected to the input vector (average spectrum magnitude) and consequently represented by a weight vector of the same length. In total, a number of 256×21 weights exist, representing the degrees of freedom of the system.

Each neuron m_i is characterized by its weight vector \mathbf{w}_i that accepts an input data represented by a sequence of vectors $\{\mathbf{x}\}$. The length of weight and input vectors is 256. The weights of neurons are randomly initialized with small values. After an input vector \mathbf{x}_i is presented to the network, a neuron that exhibits the smallest Euclidean distance $d_{i,j} = \|\mathbf{w}_j - \mathbf{x}_i\|$ is claimed to be the ‘winner’. Suppose, the j neuron is found to be the closest to the input vector, i.e. wins (Fig.5.9). Instead of updating only the winning neuron, weights of all the neurons within a certain neighborhood will be corrected accordingly to Kohonen rule (Eqn.5.9). As a result, topologically neighboring neurons tend to group together in the input space and respond similarly to the similar stimuli.

$$\mathbf{w}_k(t+1) \leftarrow \mathbf{w}_k(t) + \Phi_{j,k}(t) (\mathbf{x}_i(t) - \mathbf{w}_k(t)), \quad (5.9)$$

Here $\Phi_{j,k}(t)$ is called the neighborhood function. There are several approaches to how it is defined. In our case however, the neighborhood function takes “bubble” form (Eqn. 5.10). It is equal one up to a certain radius from the winner, and zero otherwise.

$$\Phi_{j,k}(t) = \begin{cases} 1, & r_{j,k} \leq r(t) \\ 0, & r_{j,k} > r(t) \end{cases} \quad (5.10)$$

Training of SOM is performed in *batch mode*. All the training vectors $\{\mathbf{x}\}$ are intro-

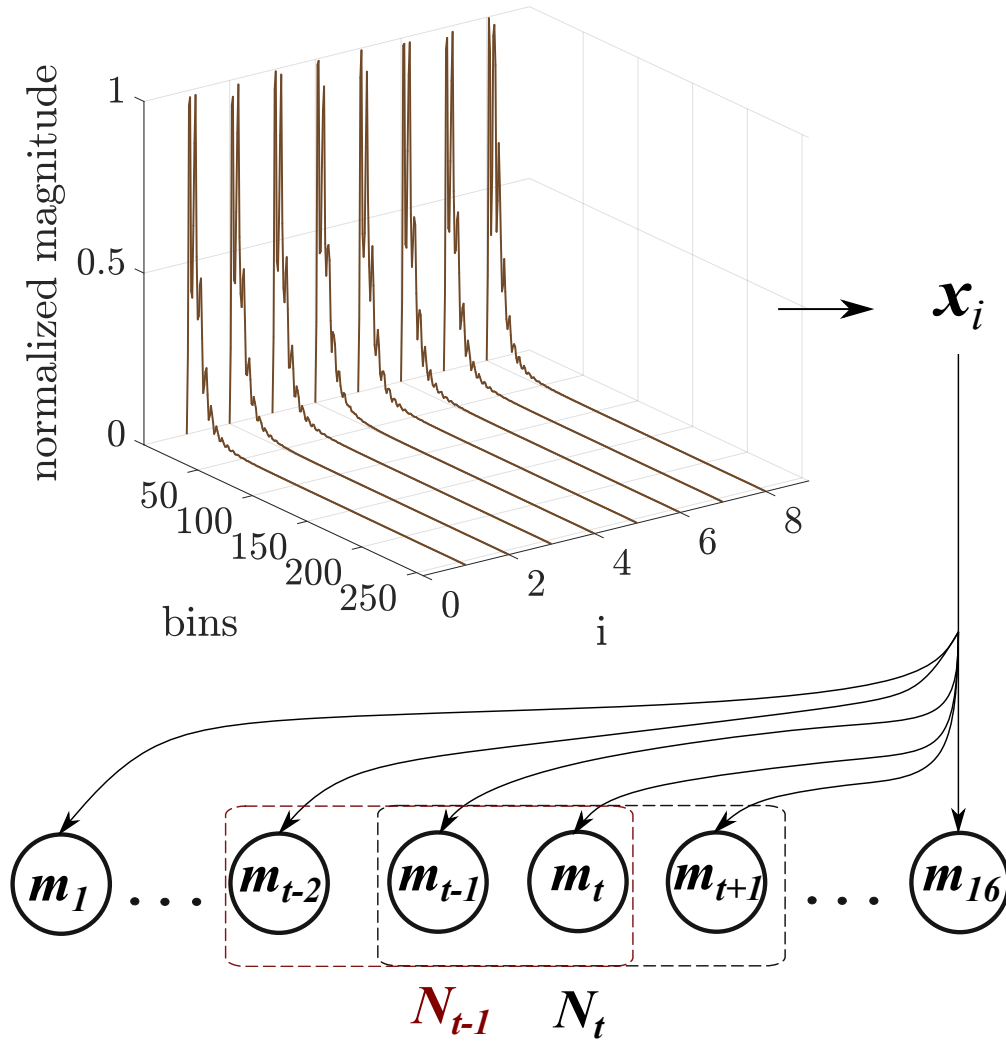


Figure 5.9. – Visual representation of a SOM. Each radial averaged spectrum is an input vector \mathbf{x}_i that is being broadcast into an array of neurons m_t . The weights of all neurons that are localised in the neighborhood N_t around the best matching one are updated together withing a training step.

duced to the neural network simultaneously. Each weight vector acquires average values of all the input vectors for which it is in the neighborhood N_t of a winner. The training cycle repeats, replacing old \mathbf{w}_i with the means over N_t , until the desired equilibrium is reached. The size of the neighborhood is altered during the training in two phases. First, the initial distance $r(t=0)=8$ linearly decreases over the period of 1000 epochs down to $r(t=1000)=1$. During this phase neurons weight vectors order them self in the input space accordingly to their topological order. After neighborhood size decreases below 1, only the weights of the wining vectors will be updated. The value of $r(t)$ is kept constant in this phase (Fig. 5.10).

5.5. RESULTS OF UNSUPERVISED CLASSIFICATION OF RED BLOOD CELL SHAPES

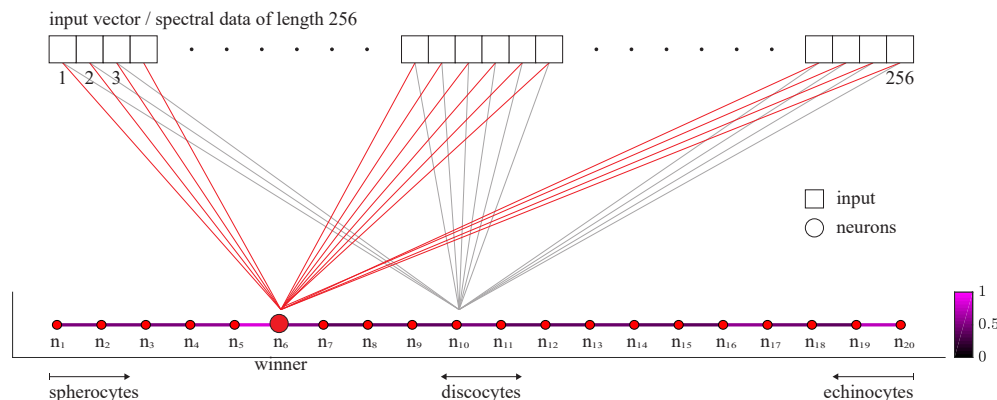


Figure 5.10. – Visual representation of the learning process. The euclidean distance between the weight vectors in the input space is represented in colour. As the system gets trained, neurons, initialized randomly, start to spread and cluster in the input space, responding to the similar stimuli.

The entirety of the manually classified dataset (spherocytes, discocytes, echinocytes, stomatocytes and intermediate echinocytes) is applied to the network simultaneously. We will show that intermediate shapes are automatically allocated in between main shape types. After 1000 iterations, the values within the weight matrices converge and the resulting distribution of system outputs is found to be the same or very similar amongst different runs.

5.5. Results of unsupervised classification of red blood cell shapes

The result of cell shape classification using the SOM is illustrated on the Fig.5.11. Unlike the ANN used in a previous section, the SOM does not require anticipatory training of the network. Before we used a limited data set to introduce to neural network as distinct classes and assigned certain values to them. SOM on the other hand, orders data automatically. Because of that, the result of cell shape classification may vary in multiple trials of SOM training. However, our neural network processes input data during 1000 iterations to ensure reproducibility of the output. And while cell classification is always performed in a similar manner, the distributions depicted on the Fig.5.11 may appear mirrored, depending on the values of neurons weight vectors which are initialised randomly.

All the input vector are allocated in distinct classes and intermediate shapes (i.e. echinocytes type I and II and stomatocytes) are distributed in between main shapes of RBCs. Overlap of distributions suggest, that this classification method can be improved. Additional steps in the image processing might highlight the specifics in the average spectra for distinct cell shape types. Applying more elaborate neighbouring function for training process might also improve the work of SOM. Despite the fact, that the cell

5.5. RESULTS OF UNSUPERVISED CLASSIFICATION OF RED BLOOD CELL SHAPES

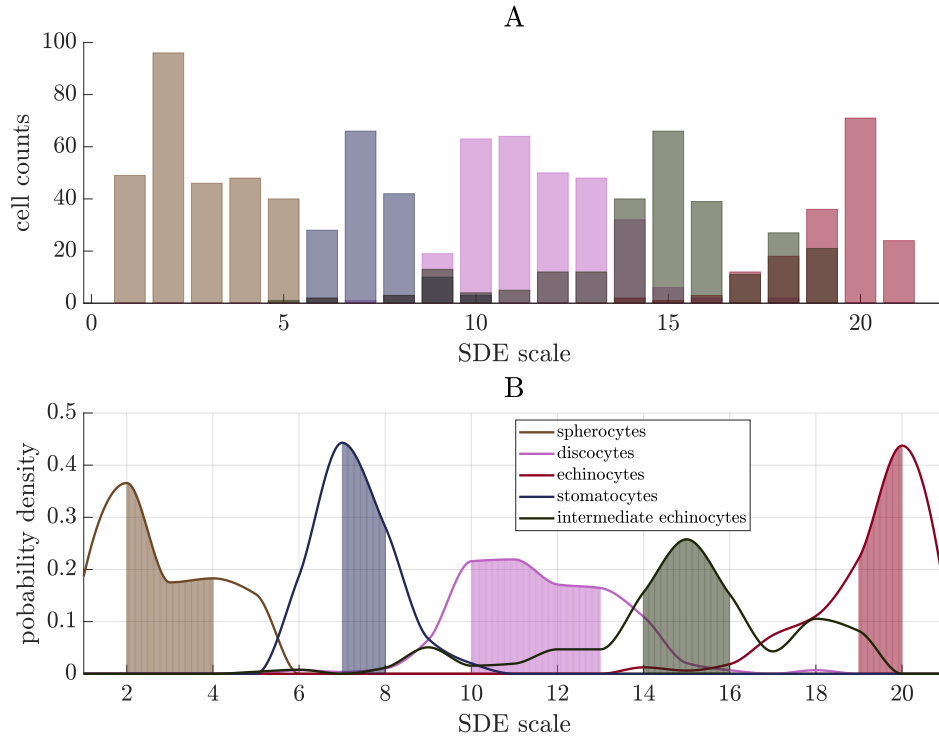


Figure 5.11. – Output of the SOM for automated cell shape classification. The SDE scale is represented in the form of 21 neurons. The SOM clusters input data without assigning values to the classes beforehand. **A** illustrates the histogram of neurons individual responses to a classified input data. Results withdrawn from this histogram are fitted with a smoothing function and normalized in order to create a probability density function depicted in **B**. Striped zones are the areas between first and fourth quantiles of the distributions.

classification produces overlapping distributions of RBCs shape types, the proposed approach for shape recognition based on the averaged 3D Fourier spectra shows promising results and might have opportunities for other applications.

6. Margination of rigid red blood cells

In this chapter, we study the phenomenon of margination in blood which is the segregation between stiff and soft cells flowing in a confined geometry. In the Stokes regime, the behavior of such a suspension depends on the many-body and wall-body hydrodynamic long-range interactions. This chapter is divided in three distinct studies in order to answer three groups of questions:

1. Does the way to confine suspension has an importance? Is the configuration of segregation depends on conduct shape? Can we expect complex patterns of cells distribution?
 2. Few studies (numerical or experimental) conducted so far in order to determine margination dependency on the flow velocity often provide contradictory results. We aim to shed light of this problem by overcoming limitations of previous works and performing first 3D margination study.
 3. Can we determine the characteristic entrance length to establish a stationary spatial configuration of soft and stiff cells?
-

Dans ce chapitre, nous étudions la ségrégation entre les cellules rigides et les cellules molles circulant dans une géométrie confinée l dans le sang, autrement connu come le phénomène de la margination. Dans le régime de stokes, le comportement d'une telle suspension dépend sur les interactions hydrodynamiques à longue distance entre plusieurs corps et les parois. Ce chapitre est séparée en trois études distinctes afin de répondre à trois groupes de questions:

1. Est-ce que la géométrie d'un canal a une importance? La configuration de la ségrégation dépend-elle de la forme du vaisseau? Peut-on s'attendre à des structures complexes de distributions des cellules?
 2. Peu d'études (numériques ou expérimentales) réalisées jusqu'à présent pour déterminer la dépendance de la margination sur la vitesse d'écoulement donnent souvent des résultats débats. Nous voulons éclairer ce problème en surpassant les limites des travaux antérieurs et en réalisant la première étude de margination 3D.
 3. Peut-on déterminer la longueur d'entrée caractéristique pour établir une configuration spatiale stationnaire de cellules molles et rigides?
-

Das folgende Kapitel widmet sich dem Phänomen der Margination, d.h. der Tren-

nung von steifen und weichen Zellen. Im Stokes-Regime hängt eine solche Suspension von langreichweitigen hydrodynamischen Vielkörper- und Wand-Körper-Wechselwirkungen ab. Dieses Kapitel befasst sich mit drei unabhängigen Studien, um Antworten auf drei wesentliche Fragen zu erhalten:

1. Hat die Art des Confinement eine Auswirkung auf die Suspension? Ist die Konfiguration der Trennung abhängig von der Form des Verhaltens? Können komplexe Muster der Zellverteilung erwartet werden?
2. Einige der bislang durchgeführten Untersuchungen (numerisch wie experimentell) zeigen sehr unterschiedliche Resultate. In dieser Arbeit sollen die experimentellen Beschränkungen durch 3D-Studien überwunden werden.
3. Kann eine charakteristische Eintrittslänge bestimmt werden, um weiche und steife Zellen räumlich zu trennen.

6.1. Margination paths of rigidified red blood cells in different geometries

In this section we will discuss the impact of the cross-sectional geometry of microchannels on the possible margination routes. We will describe margination patterns in pseudo two dimensional flow, rectangular channels and circular capillaries. Our results suggest that the trajectories of marginating rigid RBCs are significantly affected by geometry of microchannel. We will discuss previous works on this subject. Contradictions between current and earlier studies will be addressed and explained.

Dans ce chapitre, nous discuterons l'influence de la géométrie des microcanaux sur la margination. La margination pour un écoulement pseudo-2D, les canaux rectangulaires et les capillaires circulaires sont décrits dans ce chapitre. Nos résultats suggèrent que les trajectoires de particules marginant sont notablement affectées par la géométrie du microcanal. Nous considérerons donc les travaux précédents relatifs à ce sujet. Les contradictions entre notre étude et les travaux antérieurs seront traitées et expliquées.

In diesem Abschnitt wird der Einfluss der Querschnittsgeometrie der Mikro-Kanäle auf die möglichen Marginationsrouten besprochen. Wir beschreiben Marginationsmuster im Pseudo-zweidimensionalen Fluss, rechteckigen Kanälen und kreisförmigen Kappillaren. Unsere Ergebnisse legen nahe, dass die Trajektorien marginierter, starrer roter

Blutkörperchen signifikant durch die Geometrie der Mikrokanäle beeinflusst sind. Wir besprechen frühere Arbeiten zu diesem Thema und diskutieren Widersprüche zwischen aktuellen und früheren Studien.

6.1.1. Theoretical background

As we mentioned before, despite the lack of understanding about precise mechanisms involved in margination, it is believed that this cross-sectional migration of certain cells in blood flow is governed by RBCs. In physiological conditions, margination will result in the increased density of cells along vessel walls. It is reasonable to expect an increment of density to be homogeneous due to axial symmetry of the vessel. However, most *in vitro* experiments involve microfluidic chambers that usually have rectangular cross section. In [Yang, Forouzan, Burns, et al. 2011](#) was made a theoretical prediction on possible margination paths in microchannels with different cross-sections (Fig.6.1).

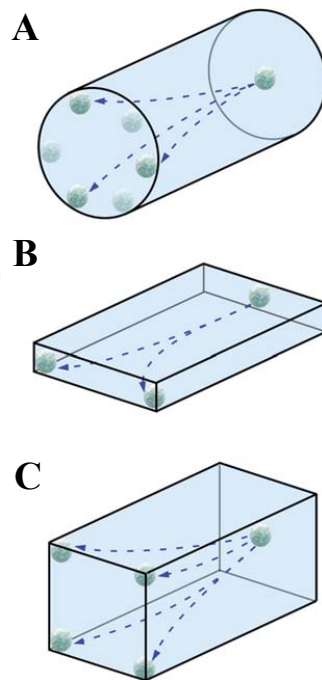


Figure 6.1. – Possible margination paths for leukocytes flowing with whole blood through channels with different cross-sections. The image was adopted from [Yang, Forouzan, Burns, et al. 2011](#). (A) Circular cross section. (B) Slit-like channels, imitating 2D flow. (C) Rectangular channels.

Authors suggested, that in channels with high width/height aspect ratio margination will occur preferentially at the sidewalls of a channel. In case of circular geometry of a cross-section, the margination profile will be equiprobable all along the perimeter of a channel wall. If width/height aspect ratio of a microfluidic chamber equals or close to

1 than the crosssection is not restricted to two dimensions. In such case, margination is likely to occur near the sidewalls as much as the top and the bottom walls of the channel, and would ultimately result in the increased density of marginating cells/particles in the corners. A recent study with stiffened RBCs (Y. Chen, D. Li, Y. Li, et al. 2017) claims to prove a rather different trend. According to these findings, margination in the channels with irregular geometries of a cross-section arises from acute angles in the microfluidic chamber. The margination region for rigid cells is defined by equilibrium of two forces acting on them: the wall-induced lift force (see Equation 2.12) and the first normal stress which can be expressed as:

$$F_N \sim \mu \lambda \nabla \dot{\gamma}^2 \quad (6.1)$$

, where λ is the relaxation time of the solution, μ is viscosity, $\dot{\gamma}$ is local shear rate. The normal stress is co-directed with the shear rate gradient $\nabla \dot{\gamma}$. The stiffened RBCs would perform margination when they are in the region where the normal stress is pointing to the wall. This study indicates that in circular geometry margination is not possible since the shear rate gradient is pointing to the center of a channel. To correlate these findings with the well known fact of margination taking place under physiological conditions, the authors show that the venules in fact have irregular geometry. Such irregularity is claimed to be the cause of platelets/WBCs margination. While these results contradict numerous numerical studies, no experiments were performed on margination in circular capillaries in case of 3D flow.

This section is dedicated to the study of rigidified cells marginating in channels with different cross-sections. To investigate cells distribution in rectangular channels microfluidic devices were fabricated by classic PDMS molding technique (see Section 3.1). To show the distribution of rigidified RBCs in 3D flow we used channels with section dimensions of 60 μm in width and 30 μm in height. To obtain mono-layer of cells and by doing so to imitate pseudo two dimensional flow we used 8 μm height and 60 μm wide channels. For margination experiments with circular cross section area glass capillaries with an inner diameter of 50 μm were used. RBCs were taken from a healthy donor, washed and suspended in the iohexanol based solution to prevent sedimentation and maintain a constant hematocrit level during experiment (see Section 4.1). A small portion of RBCs (<1%) was rigidified with glutaraldehyde, fluorescently labeled with CellMask™ Deep Red Plasma membrane stain (Molecular Probes Life Technologies) and then added to the sample to create a binary suspension with two populations of cells with different rigidities. The rigidity of hardened RBCs was measured with AFM (see Section 4.5.1).

6.1.2. Experimental setup

The distribution of rigidified RBCs (1% of glutaraldehyde) in rectangular microchannels was evaluated by means of high-speed confocal microscopy (CSU-W1 Andor Tech-

6.1. MARGINATION PATHS OF RIGIDIFIED RED BLOOD CELLS IN DIFFERENT GEOMETRIES

nology). In each focal plane cells passing through the section of a channel were tracked and their coordinated were calculated (Fig.6.2). Cells contribution to the final probability density function was corrected by the local velocity accordingly to Section 4.3. In other words, input of each cell to the probability density function is inversely proportional to the velocity field in that point. Individual in-plane distributions of rigid cells were further assembled together to recreate 3D concentration profile of marginating cells. A solid state laser ($\lambda = 647$ nm, Nikon LU-NV Laser Unit) was used as a light source for fluorescent imaging. The visualization of blood flow was implemented via inverted microscope (Nikon Eclipse Ti) equipped with an oil immersion 40x objective (1.3 N.A.). Image sequences were acquired with a sensible digital camera (Orca-Flash4.0 C11440 Hamamatsu) at the exit of microfluidic devices, making travelled distance of cells equal to 5 cm.

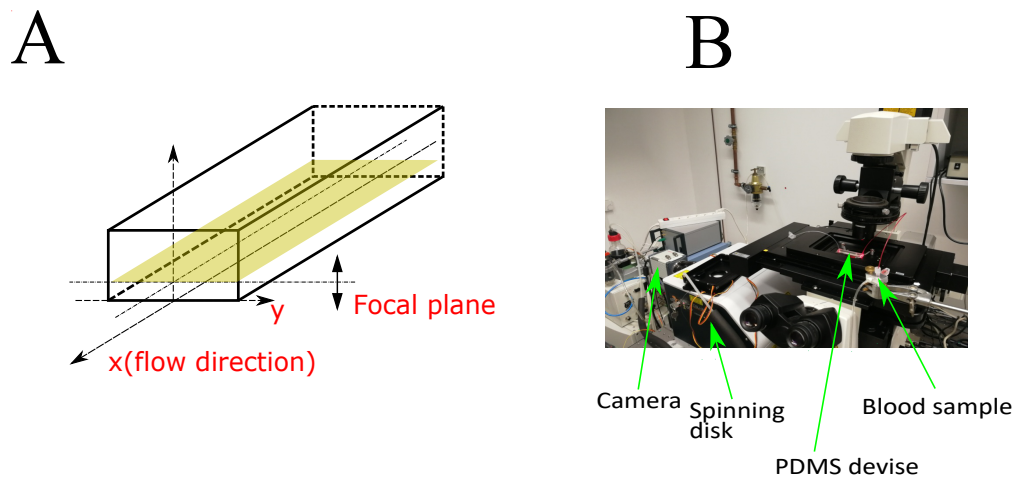


Figure 6.2. – Study of margination in microfluidic channels with rectangular cross-section. **(A)** General idea behind confocal imaging in microfluidics. In rectangular microfluidic channels, labeled RBCs were tracked in different planes along z axis by means of confocal microscopy. Further the data from different planes were assembled to reconstruct 3D distribution of rigidified cells. **(B)** Experimental setup.

Experiments with glass capillaries were performed without confocal microscope. The excitation of fluorescently labeled stiff cells was still conducted with a solid state laser. Glass capillaries were placed vertically making the observation view and the flow direction co-oriented (Fig.6.3). The free extremity of a capillary was immersed in the high density Optiprep solution in a small reservoir built on a cover glass. This was made in order to avoid the accumulation of RBCs on the bottom of reservoir once they leave the capillary and thus avoid the distortion of the image. Imaging was carried out via inverted microscope (Nikon Eclipse Ti) equipped with 20x objective (0.8 N.A., 1000 μ m WD). This approach allowed us to visualize flowing cells at the exit of a capillary and to estimate their 3D distribution without putting together individual 2D distributions. Conducting experiments in such manner limits our options for the velocity correction.

6.1. MARGINATION PATHS OF RIGIDIFIED RED BLOOD CELLS IN DIFFERENT GEOMETRIES

Since the focal plane is normal to the flow direction we can not estimate the velocity of individual labeled cells. Because of that, we had to restrict ourself to the theoretical flow velocity profile described in Section 4.3.

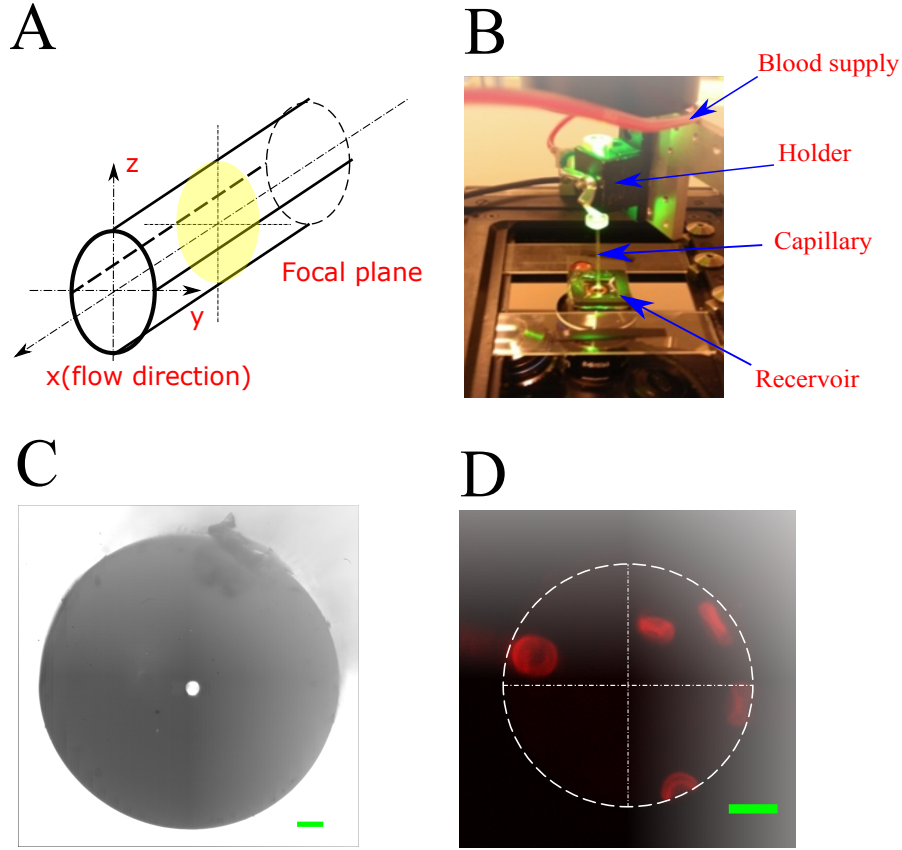


Figure 6.3. – Study of margination in glass capillaries. **(A)** General idea behind the original imaging technique. Directions of observation and flow in a capillary are co-oriented making the field of view orthogonal to the axis of symmetry. That allows us to detect rigid RBCs and obtain 3D distribution without confocal microscopy. **(B)** Experimental setup. **(C)** Image of the glass capillary extremity. Outer diameter 1 mm, inner diameter 50 μm . Scale bar 100 μm . **(D)** Example of the image obtained with our technique (scale bar 10 μm). The white outline designates the inner border of the glass capillary.

6.1.3. Results

First we will address to margination behaviour of rigidified RBCs in confined rectangular 8 μm high and 60 μm wide microchannels imitating 2D flow (Fig. 6.4 A). Rigid cells tend to marginate, namely migrate towards side walls of the channel, as would be expected. This representative image of rigid RBC distribution is showed without any velocity correction. Because of the high confinement of a channel labeled cells interact with walls making determination of velocity field profile problematic. Even without the

6.1. MARGINATION PATHS OF RIGIDIFIED RED BLOOD CELLS IN DIFFERENT GEOMETRIES

correction, one can observe significant level of cell segregation in these channels. While this geometry is far from physiological conditions, considerable margination degree and the flow composed of a mono-layer of cells, makes tempting studies of cell segregation in slit akin microchannels. In channels with lower aspect ratio (Fig.6.4 B) rigidified

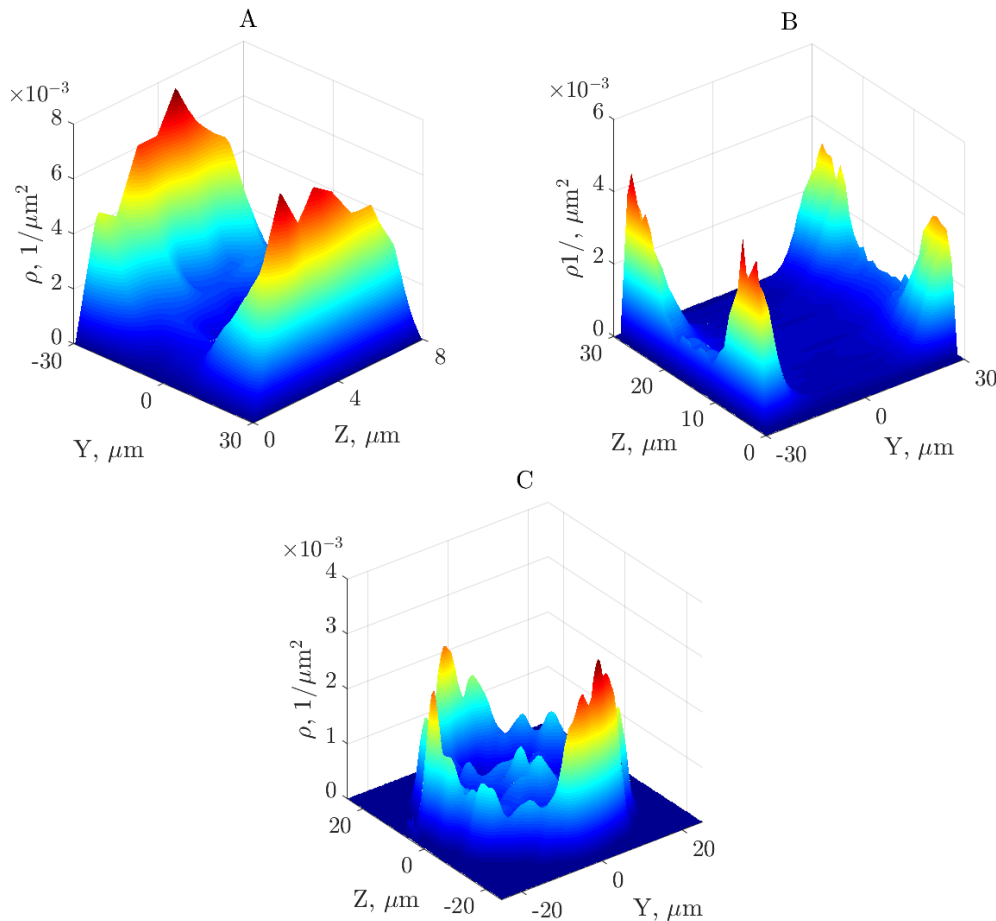


Figure 6.4. – Example of typical margination patterns in microchannels with different cross-sections. **(A)** Microchannels with high aspect ratio: to obtain pseudo-2D flow, 8 μm high and 60 μm wide channels were used. The distribution of rigidified RBCs was withdrawn from confocal image sequences. In this example distribution was not corrected by cells velocity and represents number of rigid RBCs passing per unit of cross section area. **(B)** Margination in a rectangular channels of 30 μm in height and 60 μm in width. **(C)** Distribution of rigidified cells in glass capillaries with inner diameter of 50 μm .

cells are not distributed equally along microchannel walls. Instead, rigid particles have tendency to marginate in the corners of microfluidic chamber. The reconstructed 3D distribution shows, however, that while the corners of microfluidic chamber are being preferential locations for rigidified cells, in the middle of the channel occurs an increment of concentration. We observed this trend mainly for hematocrit levels higher than

20%.

In glass capillaries rigid cells are allocated along side capillary wall without any favorable position at the periphery (Fig.6.4C). The concentration profile of rigid cells is visualized as a 2 dimensional kernel density distribution on a 256×256 grid based on a map of appearances (Botev, Grotowski, and Kroese 2010). Thus inhomogeneities in the distribution is simply a statistical error.

6.1.4. Discussion

A considerable margination level in confined channels with the respect to other studied geometries can be attributed to the shorter distances required for rigid cells to travel from the center of a channel to the periphery of the flow. Another explanation could be the difference in mechanisms causing margination: while cell segregation in 3D flow represents hydrodynamic collision induced lateral migration, margination in slit like channels is caused by volume exclusion. To separate these two effects additional studies must be performed.

The accumulation of cells in the corners of a microfluidic chamber is caused by the impairment of rotational symmetry of the velocity profile and demonstrates the fallacy of speculation that particles marginate towards regions with higher shear rate. The increased concentration of rigid cells in the center of a microchannel could be explained by a finite size of the vessel or in other words that not all cells had time to marginate. Although, as we will show later in this work, at all studied values of velocity and hematocrit the distribution of rigid cells can be considered saturated. Another possible explanation for the magnified rigid cells concentration in the center of a microchannel could be the "lift-off" mechanism that was demonstrated in D. A. Fedosov, Fornleitner, and Gompper 2012. In some cases healthy RBCs migrate in the gap downstream between a marginating particle and the border of a channel forcing it to move away from the wall. However, the origin of this phenomenon was not studied in present work. Another possible explanation can be found in Falcucci, Melchionna, Decuzzi, et al. 2018. In this numerical study marginating particles initially located in the capillary closer than $R/2$ to the axis do not experience any significant sensible velocity towards the outer part of the vessel. It could mean, that some particles are "trapped" in the bulk flow near the center line and can not marginate. As we observed this increment of rigid cells concentration near the centerline of a channel for hematocrits higher than 20%, it is worth noticing that in Falcucci, Melchionna, Decuzzi, et al. 2018 the concentration of RBCs was set to 40%.

This margination pattern in glass capillaries is guided by the rotational symmetry of the channel cross section and the velocity field. However, we observe an accumulation of labeled particles in the center of the channel as we had in case of rectangular microchannels. Our results contradict findings of Y. Chen, D. Li, Y. Li, et al. 2017. However, it that study theoretical analysis is not fully complemented with experimental results. *In vitro* measurements in Y. Chen, D. Li, Y. Li, et al. 2017 did not account distribution of stiffened RBCs in 3D flow (in rectangular microchannels focal plane was moved to the

bottom and in case of circular cross-section to the middle) and the distribution was not corrected by the velocity profile.

6.2. Dependence of margination on varying velocity and hematocrit

In this section we describe the quantitative analysis of a rigidity based margination as a function of the varying flow velocity and hematocrit. For this study we used straight 5 cm long rectangular microchannels. The cross section of a microchannel is 30 μm in height and 60 μm in width. The microfluidic devices were fabricated according to conventional PDMS molding technique described in Section 3.1. To force the solution at a requested flow velocity values through microchannel a pressure driven pump was used (see Section 3.2). Analogously to Section 6.1, the cross sectional distribution of rigid RBCs in the microchannels was evaluated by means of confocal microscopy. As was mentioned previously, working with stiffened RBCs allows us to focus only on rigidity based margination, excluding the impact of other particles properties. Due to the simplicity of replication of microfluidic devices, we restricted our quantitative analysis of margination to straight rectangular channels. Developing model experiment in such manner, enables us to investigate independently how different hematocrit levels and flow velocities influence margination in stable pressure driven flow.

Dans cette section, nous décrirons l'analyse quantitative de la margination induite par la rigidité en fonction de la vitesse d'écoulement et de l'hématocrite. Pour cette étude, nous avons utilisé des microcanaux rectangulaires avec une longueur de 5 cm, une hauteur de 30 μm et une largeur de 60 μm . Les dispositifs de microfluidique ont été fabriqués par moulage du PDMS (voir Section 3.1). Pour pousser la solution à travers un microcanal à la vitesse demandée, un contrôleur de pression a été utilisé (voir 3.2). Similairement à 6.1, la distribution des globules rouges rigides dans les microcanaux a été évaluée par microscopie confocale. Comme nous l'avons déjà mentionné, le fait de travailler avec des globules rouges rigidifiés nous permet de nous concentrer uniquement sur la margination induite par la rigidité. Nous avons limité notre analyse quantitative de la margination aux canaux droits rectangulaires pour des raisons qui sont liées à la facilité de fabrication de ces dispositifs PDMS. Ce modèle expérimental nous permet d'étudier de façon indépendante, l'influence des différents taux d'hématocrite et de la vitesse d'écoulement sur la margination.

Der folgende Abschnitt behandelt die quantitative Analyse der steifigkeitsabhängigen Margination als Funktion der Fließgeschwindigkeit und des Hämatokrites. Hierfür wurden 5 cm gerade Mikrokanäle verwendet, welche mittels PDMS-Abformung hergestellt wurden, wie es bereits in Abschnitt 3.1 beschrieben wurde. Eine druckgesteuerte Pumpe erlaubt es, die Flüssigkeiten mit den gewünschten Fließgeschwindigkeiten durch den Kanal zu bewegen (siehe hierzu Abschnitt 3.2). Analog zu Abschnitt 6.1 wurde die Verteilung der Zellen entlang des Querschnitts mittels Konfokal-Mikroskopie bestimmt. Wie bereits zuvor erörtert wurde, erlaubt die Verwendung versteifter Zellen die Untersuchung der steifigkeitsabhängigen Margination unabhängig vom Einfluss anderer Partikeleigenschaften. Um die Vervielfältigung der Mikrofluidik zu vereinfachen, wurden die Studien auf lineare, rechteckige Kanäle beschränkt. Modellexperimente dieser Art erlauben es, den Einfluss von Hämatokrit und Fließgeschwindigkeit auf die Margination unabhängig voneinander zu bestimmen.

6.2.1. Experimental setup

It is common understanding, that margination in blood flow is governed by deformable RBCs. From this perspective, margination of rigid particles in the flow is a collision based phenomenon. A higher concentration of RBCs and a higher flow rate result in more frequent collisions and therefore increase the degree of margination. However, in this chapter we will show that margination behaviour as a function of hematocrit and flow velocity is more complicated than this. Margination dependency on the velocity was investigated for 3 different discharge hematocrit (H_D) values 10, 20 and 40% (see Section 4.1) by adjusting volume concentration of healthy RBCs in the sample, used during the experiment. The necessary RBCs concentration was achieved by carefully pipetting a required volume of washed RBCs pellet. Hence, it is important to note, that we only controlled hematocrit of a blood sample and not the volumetric portion of RBCs in the microchannel. As well as in Section 6.1, less than 1% of RBCs volume was rigidified with 1% glutaraldehyde, fluorescently labeled with CellMask™ Deep Red Plasma membrane stain (Molecular Probes) and then added to the sample. The pressure pump was used in order to impose a wide range of flow rates (for more details see Section 3.2). As described in Section 4.1, both healthy and stiffened RBCs were suspended in the isodense solution to avoid sedimentation and, hence, keep the hematocrit constant during an experiment. Nevertheless, it is worth noticing, that the stiffened cells are denser than healthy RBCs. The increased density originates in the rigidification process as glutaraldehyde causes slight dehydration of cells. In our case, the sedimentation of rigid cells results in the decreasing with time sample rate. However, parameters of the flow are not affected by this.

Similarly to Section 6.1, Z-stack resolution was provided by confocal spinning disk (CSU-W1 Andor Technology). Before experiment, microchannels and outlets were filled with 20 mg/ml BSA in PBS solution to reduce adherence. The confocal imaging was performed from the bottom layers of a microchannel to the middle plane. The intensity

of the fluorescent signal is decreased when the spinning disc implemented. Because of that, at high flow velocities it is problematic to acquire quality images of moving cells more than $15 \mu\text{m}$ away from the bottom of the channel. For consistency, the image sequences throughout the entire range of studied flow velocities were acquired only from the bottom of the channel to the middle plane. The recording consists of 1000-3000 images in each plane and was carried out with $1 \mu\text{m}$ step of the piezo-motors. Once the middle plane was reached, an additional image sequences were recorded moving towards the bottom of microfluidic chamber along Z-axis. In that way, we compensate changes in the sample rate, caused by sedimentation of rigid RBCs. The taken images were processed and analysed with the custom written software (MATLAB, The Math-Works) to detect centroids of the labeled cells and reconstruct the 3D distribution across a microchannel (see Section 4.4). The image sequences were acquired with the sensible digital camera (Orca-Flash4.0 C11440 Hamamatsu). All the recordings were conducted at the exit of 5 cm long microfluidic channel.

6.2.2. Quantitative parameters of margination

In order to quantify the margination we kept track of three parameters. The first is the corner concentration of rigid cells. $8 \mu\text{m} \times 8 \mu\text{m}$ square zone in the corner of a microchannel was chosen as a characteristic margination area for rectangular channels. A portion of rigid cells concentrated in the corner zones relative to the total number of rigid cells passing through a cross-section of a channel was decided to be a quantitative margination parameter.

$$\begin{cases} M = \frac{\sum_{\phi} \xi(y, z) \delta_i(y, z)}{\sum_{\Phi} \xi(y, z) \delta_i(y, z)} \\ \sum_{\Phi} \delta_i(y, z) = N \end{cases} \quad (6.2)$$

Here M is a margination level, $\xi(y, z) = 1/v_x(y, z)$ is a weight function inversely proportional to local velocity, $\delta_i(y, z)$ is a Dirac's function that equals 1 wherever a rigid cell appears, ϕ represents $8 \mu\text{m} \times 8 \mu\text{m}$ margination zone, Φ is a whole area of a microchannel cross section and N is a total number of detected rigid cells. Further in the work, this approach will be referred to as *Method A*.

The second parameter that we use is the wall density of rigidified cells. The concept is schematically illustrated on Fig. 6.5. Here $h=60 \mu\text{m}$ and $w=8 \mu\text{m}$ are the height and the width of a microchannel respectively, $D \approx 33.54 \mu\text{m}$ is the half diagonal of a cross section. The density is estimated as a portion of cells within the green zone normalized by its area and further corrected by the velocity. In such manner, the density was estimated analogously to the circular channels. The near wall increment of a density function was fitted with a simple Gaussian function. The highest value of this fit is a characteristic value of margination (Fig. 6.5 B). This approach will be referred to as

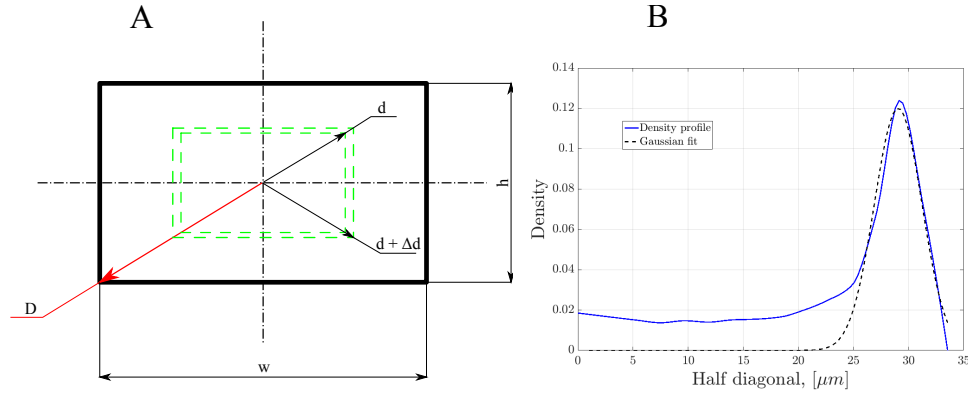


Figure 6.5. – The illustration of the general idea behind *Method B*. **A** A schematic representation of a microchannel cross-section. *Method B* allows us to calculate the density of rigid RBCs as a function of d . The stiff cells, passing through the cross-section in the rectangular region defined by d and the increment Δd are detected. The total number of cells that passed through this region, divided by its area, defines the density at a position d . The contribution of each cell to the result is corrected by the local velocity. The maximal number of steps (15) performed by the piezo limits the resolution in z to 16 different values of d . **(B)** The cross-sectional density of rigid RBCs estimated accordingly to *Method B*; the hematocrit $H_D=20\%$, mean flow velocity $v_{mean} \approx 900 \mu\text{m/s}$.

Method B.

Fitting the density profile with a Gaussian function, however, provides us with a floating result. To avoid that, a 3rd parameter was employed. We integrate the density curve (Fig. 6.5 A) and calculate a portion of cells laying in the range $[22.2;33.5] \mu\text{m}$, which are half diagonal values corresponding to $8 \mu\text{m} \times 8 \mu\text{m}$ corner zone. The results, obtained according to this approach will be further referred to as *Method C*.

Every experiment we performed resulted in a probability density function based on a certain number of events. If an experiment was considered successful (no asymmetry in the flow, no blockages formed in the channel during an experiment and etc.) the acquired sample rate was added to the accumulative data sample. Hence, every margination parameter calculated in the work, was withdrawn from one probability density function with high sample rate based on several experiments.

To calculate an error bar for evaluated parameters the final accumulative data sample was **randomly** separated in n groups ($n=6$) with an equal sample rate and for every group three margination parameters M_j^i were calculated. An array of M_j^i gives us the mean value for an iteration $\langle M \rangle_j$ and the deviation σ_j . The algorithm repeats the separation of the initial sample rate and the calculation of $\langle M \rangle_j$ and σ_j for $m = 500$ times. The final margination values are defined as:

$$\overline{M} = \frac{\sum_{j=1}^m \frac{1}{\sigma_j} \langle M \rangle_j}{\sum_{j=1}^m \frac{1}{\sigma_j}} \quad (6.3)$$

$$\overline{\sigma} = \frac{\sum_{j=1}^m \sigma_j}{m} \quad (6.4)$$

Using \overline{M} and $\overline{\sigma}$ we further calculated the confidence interval.

6.2.3. Results

Results for margination dependency on the flow velocity are depicted in Fig.6.6. Each experimental point is based on at least five experiments. Most experiments result in more than ten thousands events (detected rigid cells). Mean values and confidence intervals for margination are evaluated accordingly to Section 6.2.2. Measurement of the mean velocity is described in Section 4.3. As Fig.6.6 shows, the margination is more expressed at low velocities and in our model experiment reaches a pick around $v_{mean} \approx 1000 \mu\text{m/s}$. With the further increase of the velocity, the margination level is attenuated for all three studied hematocrits. The cell segregation is more expressed at $H_D = 20\%$. The range of velocities at which the margination is most pronounced is different for all studied hematocrits, notably at $H_D = 10\%$ the attenuation in margination level occurs very fast with an increasing velocity. Nevertheless, the margination is the most apparent at relatively low velocities for all cases. As the velocity increases, margination reaches stable values and at $v_{mean} > 4000 \mu\text{m/s}$ possibly disappears completely.

6.2.4. Discussion

The segregation of rigid cells was studied in a wide range of flow velocities. Our results show non-monotonic behaviour of margination as a function of the flow rate. A possible explanation for the drop of margination level at a high velocities could have been limitations of the experimental setup. As a flow velocity increases the rigid cells could require a longer travel distance to reach a stable distribution. To answer this question we performed series of experiments that will be discussed in the next section. While some works suggest an increase of margination with flow velocity (E. J. Carboni, Bognet, Bouchillon, Kadilak, Shor, Ward, and Ma 2016; Aarts, Broek, Prins, et al. 1988) we concluded that this trend is not inclusive. In the mean time, it is worth noticing, that according to Son 2007, values of shear rate studied in E. J. Carboni, Bognet, Bouchillon, Kadilak, Shor, Ward, and Ma 2016 belong mostly to the range of increasing margination in our experiments (the highest margination values correspond to $v_{mean} \approx 1000 \mu\text{m/s}$ or apparent shear rate $\dot{\gamma}_a \approx 100 \text{ s}^{-1}$). However, whether at a certain flow velocity margination reaches a constant value or disappears completely remains an open question. Our

6.2. DEPENDENCE OF MARGINATION ON VARYING VELOCITY AND HEMATOCRIT

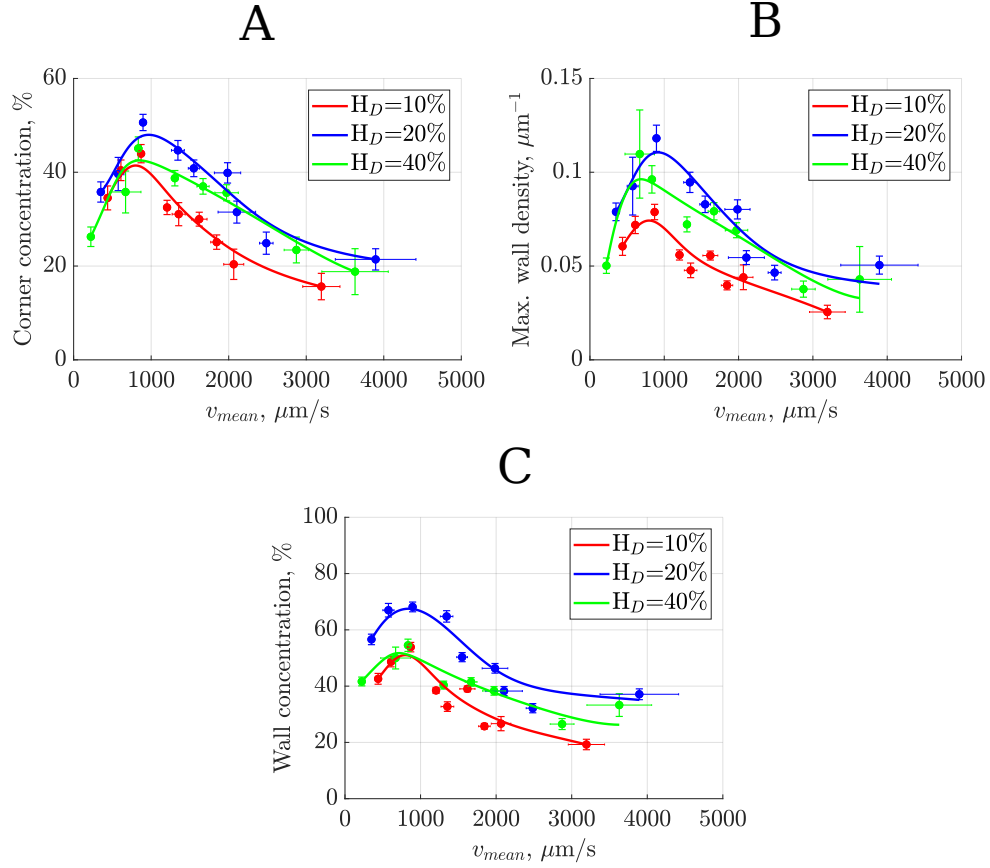


Figure 6.6. – Effect of a varying velocity on the margination. The solid lines are Bezier curves and serve as eye-guides for the figure. The confidence intervals are evaluated for $(1 - \alpha) = 95\%$. **(A)** Method A. **(B)** Method B. **(C)** Method C.

results are in qualitative agreement with previous experimental (Namdee, Thompson, Charoenphol, et al. 2013) and numerical (Müller, D. A. Fedosov, and Gompper 2016; D. A. Fedosov, Fornleitner, and Gompper 2012; Zhao, Shaqfeh, and Narsimhan 2012; Freund 2007) studies that showed an expressed margination in the regime of low flow rates. Yet, some of these studies (Namdee, Thompson, Charoenphol, et al. 2013) used particle adhesion to quantify margination, which depends on series of parameters and does not directly reflect margination behaviour, since with an increment of flow velocity adherent particles may detach from the wall. At the same time, some experimental studies were investigating the relation between margination and rouleaux formation, that occurs at low shear rates (A. Jain and Munn 2009; Pearson and Lipowsky 2000), hence drawing a link between aggregation and expressed margination. In our experiments aggregation is inhibited and has no impact on margination of rigid cells. Which allows us to conclude, that aggregation of RBCs is not required for the rigidity based margination.

6.3. Dependence of margination on the traveled distance at different hematocrits

We performed a series of experiments to evaluate the distance required to establish a fully developed margination in a microfluidic chamber. For this purpose we evaluated the distribution of rigidified cells at different positions from the entrance of a microchannel (Fig.6.7). Straight rectangular channels of 5 cm in length, 30 μm high and 60 μm wide we used for these experiments. Three different hematocrits values were studied and the applied pressure was adjusted to obtain the same flow velocity, corresponding to a highly pronounced segregation behaviour of cells, described in a previous section.

Nous avons effectué une série d'expériences pour évaluer la distance nécessaire à l'établissement d'une margination complètement développée dans une chambre microfluidique. Pour ce faire, nous avons évalué la distribution des cellules rigidifiées à différentes positions par rapport à l'entrée d'un microcanal. Des microcanaux rectangulaires avec une longueur de 5 cm, une hauteur de 30 μm et une largeur de 60 μm ont été utilisés. Trois différentes valeurs d'hématocrite ont été étudiées et la pression appliquée a été ajustée de manière à obtenir la même vitesse d'écoulement, correspondant à une forte ségrégation des cellules, décrite dans la section précédente.

Es wurden mehrere Experimente durchgeführt, um die notwendige Distanz zu ermitteln, sodass eine vollständig ausgebildete Margination in der Mikrofluidik zu beobachten ist. Zu diesem Zweck wurde die Verteilung von versteiften Zellen an verschiedene Stellen des Kanals bestimmt. Gerade, rechteckige Kanäle mit einer Länge von 5 cm und einem Querschnitt von 30 μm Höhe und 60 μm Breite wurden verwendet. Es wurden drei Messung mit jeweils unterschiedlichem Hämatokrit durchgeführt, wobei die Fließgeschwindigkeit entsprechend einer stark ausgeprägten Aufteilung eingestellt wurde, wie bereits an anderer Stelle beschrieben.

6.3.1. Experimental setup

The blood samples were prepared accordingly to 4.1. The confocal images were acquired analogously to 6.2. Additional image sequences were recorded at a different positions along a microfluidic channel in order to quantify evolution of margination parameters. The distance from the entrance at which images was taken was controlled by motorized stage.

6.3. DEPENDENCE OF MARGINATION ON THE TRAVELED DISTANCE AT DIFFERENT HEMATOCRITS

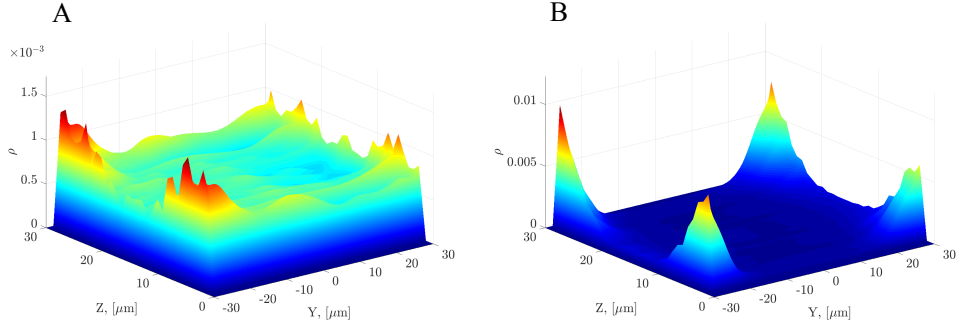


Figure 6.7. – Example of a 3D distribution of rigid RBCs passing through microfluidic channel. The hematocrit $H_D=20\%$, mean flow velocity $v_{mean} \approx 900 \mu\text{m/s}$. The distributions are corrected by the velocity field. **(A)** The entrance of a channel. **(B)** The distribution of rigid cells 5 cm away from the entrance.

6.3.2. Results

Acquired experimental results were fitted with an heuristic equation:

$$f(l) = \frac{f(0) - f(\infty)}{f(\infty)} (e^{-\frac{l}{d}} + 1) \quad (6.5)$$

Here $f(l)$ is a fitting function that depends exponentially on the distance from the channel entrance l and d is a fitting parameter. Following a trivial rule, we calculated distances necessary for margination to saturate:

$$d_s : \left| (f(d_s) - f(0)) - (f(\infty) - f(0)) \frac{1}{\sqrt{2}} \right| < \epsilon \quad (6.6)$$

The values of saturation distances d_s calculated in this simple manner (Equation 6.6) are presented in the capture of Fig. 6.8. The slowest evolution of margination is observed at $H_D=10\%$. Highest margination magnitude is achieved at $H_D=20\%$, however at $H_D=40\%$ the distribution of the rigid cells saturates notably faster.

Our results demonstrate, that the lengths of used microchannels is more than sufficient to obtain a stable distribution of rigidified RBCs. Interestingly, a distance required for a saturated margination profile to develop is in the order of centimetres. However, to determine whether margination decrease at high velocities is a result of a finite channel length or an actual velocity dependent trend (see Section 6.2) we performed additional experiments to determine the saturation distances for different pressure drops. Only one hematocrite value ($Ht_D=20\%$) was investigated at two additional different flow velocities, which correspond to lower and higher values respectively to the range of highly pronounced margination.

According to the obtained results (Fig. 6.9) margination level at all studied velocities can be considered saturated. Which brings us to the conclusion, that attenuation in cell segregation at high velocities is in fact an evidence of margination non-monotonous

6.3. DEPENDENCE OF MARGINATION ON THE TRAVELED DISTANCE AT DIFFERENT HEMATOCRITS

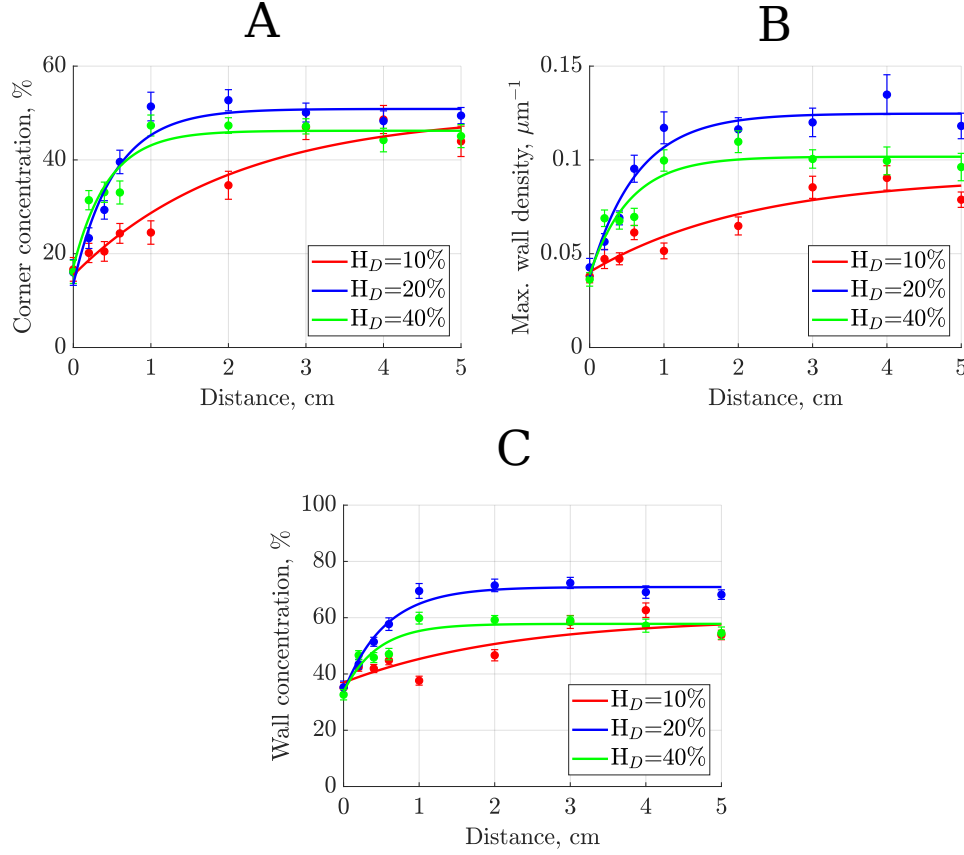


Figure 6.8. – The evolution of the margination alongside the microchannel at a different hematocrits. The confidence intervals are evaluated for $(1 - \alpha) = 95\%$ **(A)** Concentration of rigid RBCs in $8\mu\text{m} \times 8\mu\text{m}$ square zones in the corners of microfluidic device (*Method A*), d_s values are 2.54, 0.65 and 0.55 cm for H_D levels of 10, 20 and 40%, respectively. **(B)** The highest wall densities of rigid RBCs (*Method B*), d_s values are 2.65, 0.78 and 0.65 cm for H_D levels of 10, 20 and 40%, respectively. **(C)** The near wall concentration of stiff RBCs (*Method C*), d_s values are 2.72, 0.67 and 0.54 cm.

behaviour.

6.3.3. Discussion

Our results demonstrate, that margination saturates faster as hematocrit increases. Taking this into account we conclude that while in the range of physiological hematocrit values typical for microcirculation ($\sim 20\%$) margination is maximized, a higher concentration of RBCs leads to faster saturation of cells distribution. It supports the idea of margination being the result of heterogeneous collisions between deformable particles and rigid ones. According to the obtained results (Fig. 6.9) and our technique of d_s evaluation, the margination level at all studied velocities can be considered saturated. Which brings us to the conclusion, that the attenuation in rigid cell segregation at high

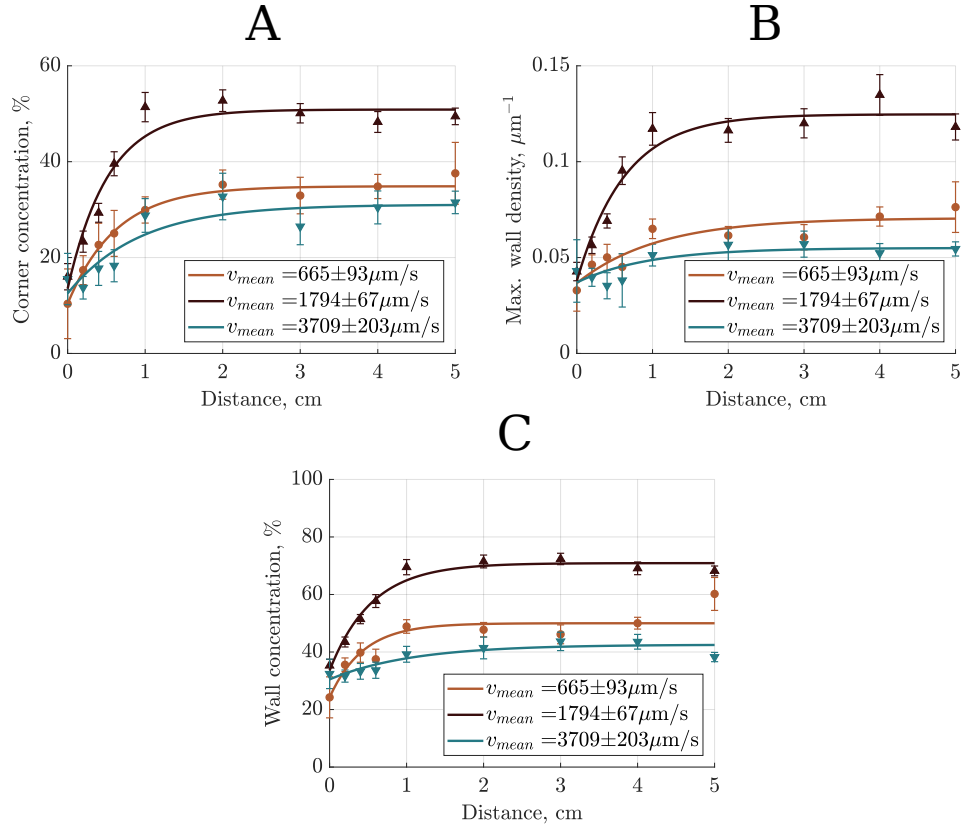


Figure 6.9. – The evolution of margination alongside a microchannel at different velocities. The confidence intervals are evaluated for $(1 - \alpha) = 95\%$. **(A)** Concentration of rigid RBCs in $8\mu\text{m} \times 8\mu\text{m}$ square zones in the corners of microfluidic device (*Method B*), d_s values are 0.71, 0.65 and 1.12 cm for increasing v_{mean} . **(B)** The highest wall densities of rigid RBCs (*Method B*), d_s values are 1.31, 0.78 and 1.16 cm for H_D levels of 10, 20 and 40% respectively. **(C)** The near wall concentration of stiff RBCs (*Method C*), d_s values are 0.53, 0.67 and 1.31 cm.

velocities, described in Section 6.2, is not related to the channel length but is in fact the evidence of margination non-monotonous behaviour. In our experiments, the saturation distance d_s is always in the order of centimetres. Such distances are much longer than one would expect in microcirculation without encountering a bifurcation. Hence we conclude, that in physiological conditions additional mechanisms are involved apart from the rigidity contrast in order to induce margination.

6.4. Comparison between experimental and numerical results

In collaboration with Dr. Othmane Aouane and Prof. Dr. Jens Harting from Helmholtz Institute Erlangen-Nürnberg for Renewable Energy, were performed series of numerical simulations in order to complement the experimental data. The results obtained *in silico*

were re-interpreted in such manner to be in accordance with experimental procedure. In the following section we are going to demonstrate the agreements and discrepancies between numerical results and experimental results described in previous sections.

En collaboration avec Dr.Othmane Aouane et Prof. Dr. Jens Harting de l'institut Helmholtz Erlangen-Nürnberg, ont été effectuées des séries de simulations numériques afin de compléter les données expérimentales. Les résultats obtenus ont été réinterprétés de manière à être en accord avec le processus expérimental. Dans la section suivante, nous allons montrer les accords et les divergences entre les résultats numériques et les résultats expérimentaux décrits dans les sections précédentes.

In Kollaboration mit Dr. Othmane Aouane und Prof. Jens Harting vom Helmholtz Institut für erneuerbare Energien in Erlangen-Nürnberg wurden numerische Simulationen durchgeführt, um die Ergebnisse der Messungen zu untermauern. Diese computergestützten Resultate wurden im Hinblick auf die experimentelle Methodik interpretiert. Im folgenden Abschnitt werden die Übereinstimmungen und Abweichungen zwischen den numerischen und experimentellen Resultaten beschrieben.

6.4.1. Numerical method

In the numerical simulations, a microfluidic chamber was presented as a rectangular duct channel of width $\hat{w} = 120\Delta x$, height $\hat{h} = 60\Delta x$, and length $\hat{l} = 800$ to $4800\Delta x$ where Δx is the lattice resolution (Fig. 6.10). Periodic boundary conditions were applied along the z -axis. In the yz and zx plans through were enforced no-slip boundary conditions. The length of a lattice unit is obtained from the analogy between the radius of the RBC chosen to be $4\text{ }\mu\text{m}$ and the numerical radius fixed to $\hat{r}=8$ leading to $\Delta x \equiv 0.5\text{ }\mu\text{m}$. The numerical experiments were conducted for a large range of the tube hematocrit (H_T) values between 2.73 and 43.73%. It is worth noting, that unlike in the experiments, in the simulations actual volumetric portion of RBCs withing the microchannel was controlled. Similar to microfluidic experiments, the rigid cells occupy 1% of the total volume of RBCs to neglect rigid cell-rigid cell interactions. Unfortunately, it also means a largely decreased sample rate at low hematocrits. The capillary number for each studied hematocrit value was fixed at $Ca=0.2$.

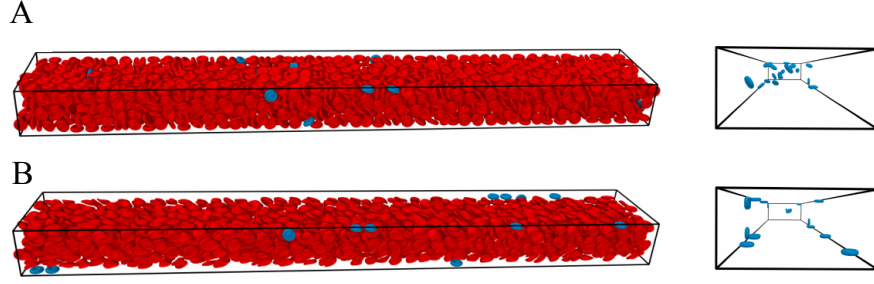


Figure 6.10. – A suspension of RBCs flowing through a rectangular duct channel. The blue cells represent the rigidified red blood cells. The capillary number $Ca = 0.2$ and the volumetric fraction of the cells $\phi = 0.3$ (A) The initial configuration. (B) The stationary configuration.

6.4.2. Data analysis in numerical simulations

In experiments density profiles acquired accordingly to *Method B* (Fig.6.5) consist of 16 points: 15 steps of piezo-motors in z -direction and zero density at the wall. In simulations we hold the total information about each cell. Therefore, we can obtain an actual cross-sectional distribution of rigid cells instead of assembling it out of 15 plane distribution profiles. Density profile of cells across microchannel section is obtained accordingly to *Method B*. Unlike the experiments, in simulations we are largely limited with the number of cells, therefore the density is very sensible to the choice of a binwidth. To account for this effect, 2D density is calculated through an adaptive kernel estimator (Botev, Gro-towski, and Kroese 2010) for 3 grids: 16×16 , 32×32 and 64×64 points. Margination values calculated for three 2D distributions are averaged. In the numerical simulations,

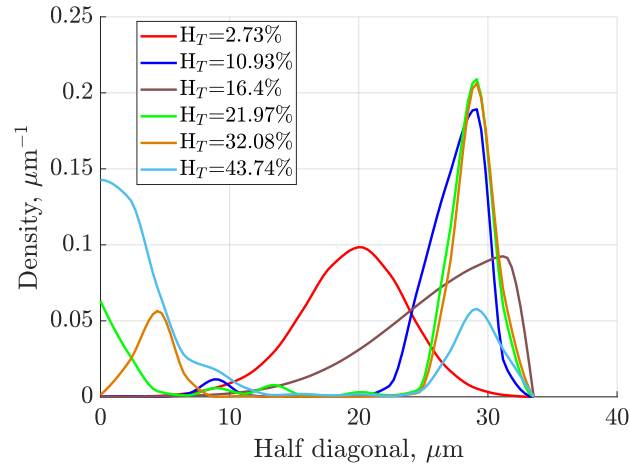


Figure 6.11. – The density profiles of rigid RBCs at mean flow velocity in simulations .

the density profiles of marginating rigid cells show shift of concentration pick at different hematocrits (Fig.6.11). As one could expect, rigidified cells migrate not to the wall of a channel exactly, but to the periphery of normal RBC bulk flow, in other words, to

the edge of CFL. For that purpose, the distribution of healthy RBCs needs to be taken in account and quantified. Using the same procedure as for rigid cells we calculated density of RBC across the channel in order to define the CFL. Fig. 6.12 demonstrates

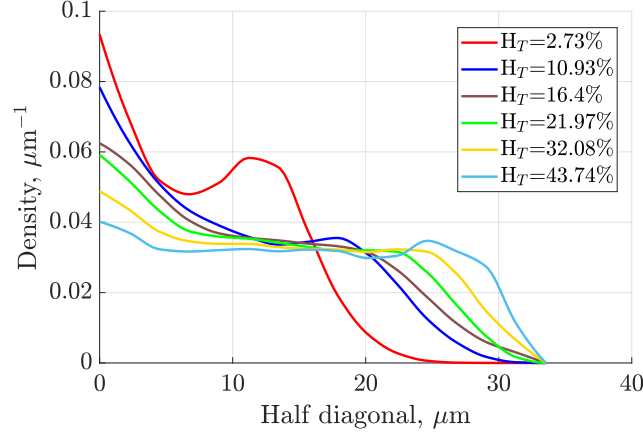


Figure 6.12. – The density profiles of normal RBC at mean flow velocity in simulations.

the reduction of CFL thickness with an increased concentration of RBC. However, it also means that a certain modifications must be made to estimate margination parameters in the numerical simulations. Instead of a stationary band, within which concentration of rigid RBC is calculated, the margination zone must vary for different hematocrit. At Fig.

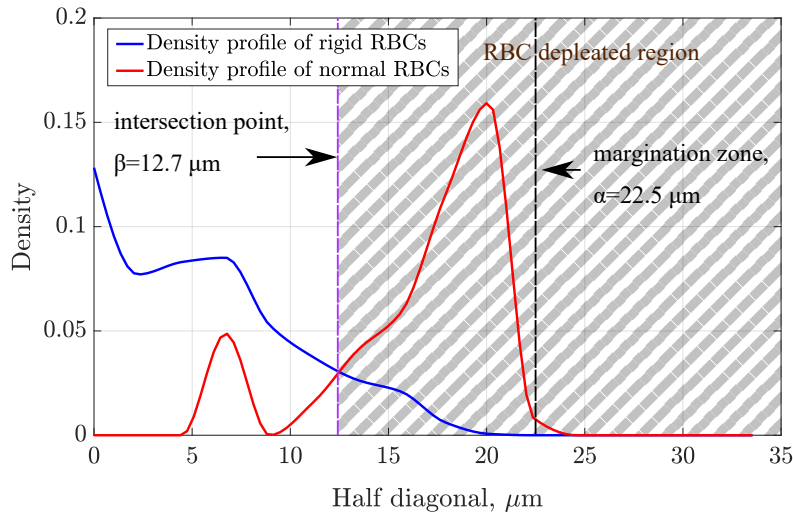


Figure 6.13. – The intersection of density profiles of normal and rigid RBCs at 2.73% hematocrit level and mean flow velocity $v_{mean} \approx 2000 \mu\text{m/s}$.

6.13 the density profiles of two subpopulations (normal RBCs and stiff cells) are plotted. This is an example, showing how the definition of the margination zone floats with the

changing thickness of CFL. Fig. 6.13 shows the intersection point of two concentration profiles at approximately $12.7 \mu\text{m}$. As Fig. 6.13 indicates, in order to obtain the margination value in accordance with *Method C*, the density profile must be integrated within much wider limits. To account for this effect, we employed a correction factor α/β for margination values obtained in the numerical simulations.

The numerical simulations provide us with information about travelled distances and velocities of individual cells at each time step of simulation. From the periodic boundary condition arises the problem of converting these data into a comprehensive analogy with experiments, i.e. the position along the channel. Travelled distance of the whole suspension for this reason is approximated as a multiplication of the time by the average velocity of cells.

6.4.3. Results

Rigid cells are shown to migrate towards equilibrium positions near the corners of the channel for each studied hematocrit value (Fig.6.14). An important similarity between experiments and simulations that we observed is the elevated concentration of the rigid cells in the middle of the channel at high hematocrit levels. This particular trend hasn't been reported in previous studies. Immediately brings attention the fact, that the margination values in simulations are much higher than in the experiments. Another observation is that, although in all the cases rigid cells tend to redistribute in channel forming concentration picks in the corners, at $H_T=40\%$ central pick is so high that the total margination level seems to be indifferent to this process. The central pick occurs at high hematocrit levels and doesn't seem to disappear with time, making it look like another equilibrium position for rigid cells similar to the corner zones.

Fig. 6.15 shows the evolution of margination in simulations for all studied hematocrits. Margination is estimated accordingly to *Method C* with a floating bandwidth, within which the concentration of rigid cells is calculated. Quantitatively, simulations show elevated margination in comparison to experimental results. Nevertheless, both in experiments and simulations we observe margination to be saturated in 1-2 centimeters from the entrance of the channel. H_T values 10.93% and 21.97% show arguably the same margination trends. With a further increment of RBC concentration a noticeable reduction in margination can be seen. The inconsistent behaviour of the margination curve at $H_T=16.5\%$ can be explained by a significantly lower amount of rigid cells upon which the statistics is built. Fig.6.16 depicts the comparison between margination values measured *in vitro* and corresponding numerical results. As we noticed before, the first distinction that we notice is the magnitude of margination. However, our numerical and experimental results clearly agree on the unusually long entrance distance required for margination to develop.

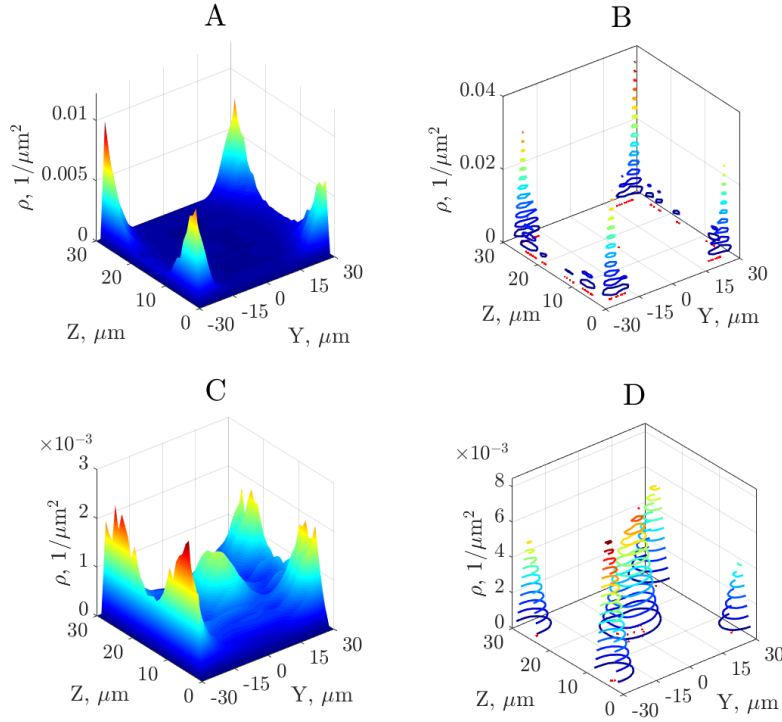


Figure 6.14. – The margination of rigid cells in rectangular channels in experiments and numerical simulations. **(A)** The distribution of rigid RBCs at $H_D=20\%$ hematocrit, with the mean flow velocity of $v_{mean} \approx 900 \mu\text{m/s}$ in experiments. **(B)** The distribution of rigid RBCs at $H_T=20\%$ hematocrit, with the mean flow velocity of $v_{mean} \approx 1300 \mu\text{m/s}$ in simulations. **(C)** The distribution of rigid RBCs at $H_D=40\%$ hematocrit, with the mean flow velocity of $v_{mean} \approx 2850 \mu\text{m/s}$ in experiments. **(D)** The distribution of rigid RBCs at $H_T=40\%$ hematocrit, with the mean flow velocity of $v_{mean} \approx 500 \mu\text{m/s}$ in simulations.

6.4.4. Discussion

The numerical simulations qualitatively reflect margination tendencies observed in experiments. Quantitatively, though, severe differences were revealed. The major contradictions between experimental and numerical results are: (1) the shift of the density peak of rigid cells concentration with increasing hematocrit; (2) the same saturation rate at $H_T < 40\%$. Both these features originate from the CFL. First of all, while in simulations we have a clearly defined zone entirely free of RBCs presence, in the experiments this is not the case. The near wall zone *in vitro* is highly depleted, but never free of cells. In [Lanotte, Mauer, Mendez, et al. 2016b](#) can be found the support for this claim. Authors reveal large spectrum of RBCs shapes in motion and suggest to re-evaluate *inter alia* the phenomenon of CFL in the light of their results. Differences in CFL in simulations and experiments is the reason why in experiments the density peak doesn't shift. Both simulations and experiments showed that rigidity based margination require a travel distance

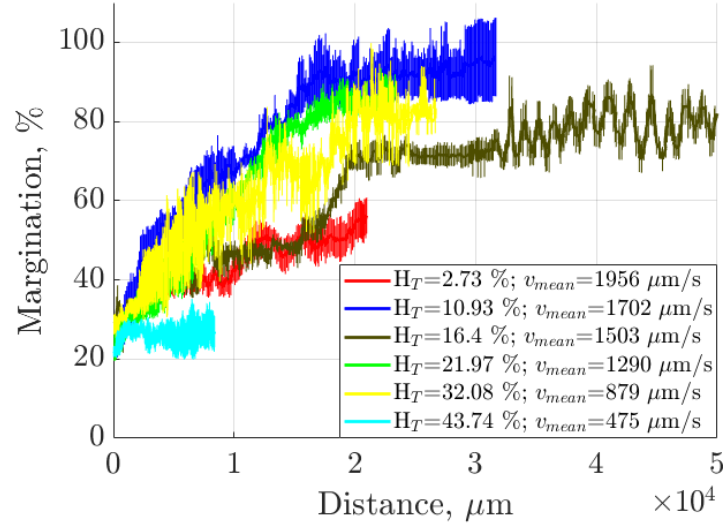


Figure 6.15. – The evolution of margination obtained from numerical simulations at various hematocrit levels. As a characteristic parameter of margination we chose near wall concentration (*Method C*)

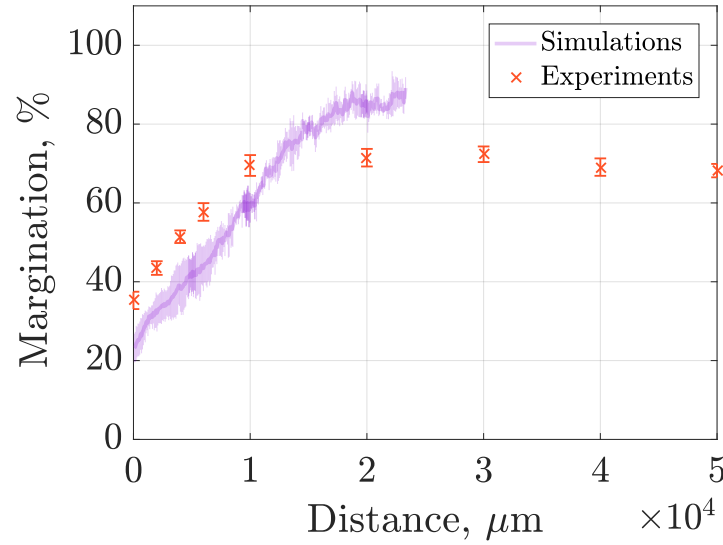


Figure 6.16. – Comparison between the experimental and the numerical results. Margination in experiments is measured for discharge hematocrit $H_D=20\%$ and the mean velocity of rigid cells $v_{mean}=897\pm33 \mu\text{m/s}$. The simulations were performed for tube hematocrit $H_T=21.97\%$ and the mean velocity of rigid cells $v_{mean}=1290 \mu\text{m/s}$. The margination values were obtained accordingly to (*Method C*)

in order of centimeters to saturate.

6.4. COMPARISON BETWEEN EXPERIMENTAL AND NUMERICAL RESULTS

There is a radical difference in how the margination level reacts to the variation of hematocrit in experiments and in simulations. At low concentration, RBCs spread out across the section freeing a significant amount of space in between them. Stiff cells fill these "vacancies" resulting in a flattened density profile. As the hematocrit increases, stiff cells are pushed into a cell depleted zone on the periphery of blood flow, commonly referred to as CFL in the literature. With the further increase of hematocrit, the size of this cell depleted region is decreased, thus reducing possible space for marginating cells. However, the drop in margination at elevated hematocrit levels is effectuated not through the flattening of distribution profile, but through the increment of stiff cell concentration in the middle of the channel. This particular trend was captured by our simulations.

Conclusions

Conclusions

This thesis is mainly dedicated to the study of collective phenomena in blood suspensions occurring in microcirculation. The central point of our research is the phenomenon of margination. The elaborated model experiment we developed allows us to study margination caused exclusively by rigidity and to precisely control other experimental parameters. We developed an experimental setup that allowed us to perform a qualitative analysis of rigidity based margination.

A part of this research is dedicated to the analysis of individual RBCs in steady state. We hypothesised, that different shapes of RBCs on the SDE scale are related and intermediate shapes can be considered as a superposition of main RBCs shapes: spherocytes, discocytes and echinocytes. We created a new approach to RBCs classification, opposite to classic technique, based on the assumption that SDE scale is a continuum and not a several distinct shape types. Our technique for 3D shape analysis confirmed the initial hypothesis. This new approach offers an unbiased method for RBCs shape classification and could be used as a diagnostic tool.

Our margination research was separated in three distinct studies. First we revealed margination patterns in the channels with different geometries. While some studies suggest that margination occurs in the zones with the lowest shear stress we showed that rigid particles marginate towards the regions most depleted from RBCs. It supports the idea that margination is mediated by distribution of RBCs. However, we also observed that in 3D flow, in some cases rigid cells are also found in equilibrium position along the centerline of a channel. We studied dependency of margination on the distance from the entrance to a channel. We concluded that to achieve fully developed margination profile cells need to travel larger distances than are usually found in microcirculation. It means that there are other mechanism apart from the rigidity contrast that induce margination. We found that the saturation rate for margination increases with the hematocrit which additionally support the idea of margination being collision induced phenomenon. Our study of margination as a function of the flow velocity revealed two interesting observations. First, we found that there is an optimal range of hematocrit values for highest margination rates. Second, we concluded that margination dependency on the flow rate is non monotonous.

This work opens a numerous perspective for future studies. Our technique for RBCs shape analysis could be applied for sickle cells. This could allow to find correlation between subpopulations of certain shape type and gravity of the disease. Next logical step in margination studies should be the dependence of margination cell rigidity. Several methods provide an opportunity for "tuning" rigidity contrast between margination cells and normal RBCs. With a model experiment, developed in this work, margination as a function of rigidity contrast can be studied.

Our experimental method reveals some interesting leads from the point of view of the physics of suspensions. It allows to explore the range of parameters of highly deformable particles. Varying the concentration of rigid particles allows the exploring of the spatial configuration of two populations in channel or Couette flow. A limitation of such experiments is the lack of variability in RBCs size. This would require the use of artificial capsule suspensions.

Conclusions

Cette thèse est principalement consacrée à l'étude des phénomènes collectifs dans les suspensions de sang qui se manifestent dans la microcirculation. Le sujet principal de notre recherche est le phénomène de margination. Notre approche nous permet d'étudier la margination causée exclusivement par le contraste de rigidité et de contrôler avec précision d'autres paramètres expérimentaux. Nous avons développé un système expérimental qui nous a permis d'effectuer une analyse qualitative de la margination induite par la rigidité.

La partie de cette recherche est consacrée à l'analyse de la forme des globules rouges, individuellement, en état d'équilibre. Nous avons émis l'hypothèse que différentes formes de globules rouges sur l'échelle SDE sont reliées et que les formes intermédiaires peuvent être considérées comme une superposition de formes principales: sphérocytes, disco-cytes et échinocytes. Nous avons créé une nouvelle approche de classification des RBCs, contrairement aux techniques classiques, basée sur l'hypothèse que l'échelle SDE est un continuum et non pas une succession de formes distinctes. Notre technique d'analyse en 3D nous a permis de confirmer l'hypothèse initiale. Cette nouvelle approche offre une méthode impartiale pour la classification des formes RBCs et pourrait être utilisée comme outil de diagnostique.

Notre recherche de margination a été séparée en trois études distinctes. Nous avons d'abord mis en évidence des parcours de margination dans des canaux ayant des géométries différentes. De plus, alors que certaines études suggèrent une margination induite dans les zones où la contrainte de cisaillement est la plus faible, nous avons montré que les particules rigides marginent vers les régions où la concentration de globules rouges est réduite. Cela supporte l'idée que la margination est régie par la distribution des RBCs. Cependant, nous avons aussi observé que dans un écoulement 3d, dans certains cas, des cellules rigides sont également situées en position d'équilibre au centre de canal. Nous avons étudié la dépendance de margination pour une certaine distance à l'entrée d'un canal. Nous avons conclu que pour obtenir un profil de margination pleinement développé, les cellules doivent parcourir des distances plus grandes que celles que l'on trouve normalement dans la microcirculation. Cela signifie qu'il existe un autre mécanisme en dehors du contraste de rigidité qui induit la margination. Nous avons également trouvé que le taux de saturation de la margination augmente avec l'hématocrite, ce qui

appuie également l'idée que la margination est un phénomène induit par les collisions entre les cellules rigides et les RBCs. Notre étude de margination en fonction de la vitesse d'écoulement a révélé deux observations intéressantes. Tout d'abord, nous avons montré qu'il existe une gamme de valeurs optimale d'hématocrites pour les taux de margination les plus élevés. Deuxièmement, nous avons conclu que la dépendance de la margination sur le débit n'est pas monotone.

Ce travail ouvre de nombreuses perspectives pour des études ultérieures. Notre technique d'analyse de formes des RBCs pourrait être appliquée pour des cellules drépanocytaires. Cela pourrait permettre de trouver une corrélation entre les sous-populations d'un certain type de forme et la gravité de la maladie. La prochaine étape logique dans la recherche relative au phénomène de margination devrait être l'étude de la dépendance de la margination sur la rigidité des cellules. Plusieurs méthodes permettent d'ajuster le contraste de rigidité entre les cellules de margination et les RBCs normaux dans une manière contrôlée. Avec le système expérimental développé dans ce travail, la margination en fonction du contraste de rigidité peut être étudiée.

Notre méthode expérimentale relève des pistes intéressantes au point de vue de la physique des suspensions. Ainsi, il permet d'explorer la gamme de paramètres de particules très déformables. La variation de la concentration des particules rigides ouvre la possibilité d'explorer la configuration spatiale des deux populations dans des géométries de Couette ou en canal. Une limite de telles expériences est l'absence de variabilité de la taille des globules rouges. Pour cela, il faudrait se tourner vers des suspensions de capsules artificielles.

Schlußfolgerung

Die vorliegende Arbeit befasst sich hauptsächlich mit der Untersuchung kollektiver Phänomene in Blutsuspensionen, die in der Mikrozirkulation vorkommen. Der Fokus unserer Forschung ist hierbei auf das Phänomen der Margination gerichtet. Das von uns entwickelte Modellexperiment erlaubt es, die ausschließlich von der Steifigkeit verursachte Margination zu untersuchen sowie die präzise Kontrolle anderer experimenteller Parameter. Wir entwickelten einen experimentellen Aufbau, der es uns erlaubt, eine qualitative Analyse steifigkeitsbasierter Margination zu erhalten.

Ein Teil dieser Arbeit ist der Analyse einzelner roter Blutzellen im stationären Zustand gewidmet. Wir nahmen an, dass unterschiedliche Formen roter Blutzellen auf XXX-Ebene verwandt sind und Zwischenzustände als Superposition von Hapterscheinungsformen der roten Blutzellen dargestellt werden können: Spherozyten, Diskozyten und Echinozyten. Wir entwickelten eine neue Technik der Klassifikation roter Blutzellen im Gegensatz zur klassischen Methode, basierend auf der Annahme, dass SDS scale ein Kontinuum darstellt und sich nicht aus mehreren diskreten Zellformen zusammensetzt. Unser Verfahren der 3D-Analyse bestätigte die anfängliche Hypothese. Diese neue Herange-

hensweise bietet eine unvoreingenommene Methode zur Klassifikation der Formen roter Blutzellen und könnte als diagnostisches Werkzeug verwendet werden.

Unsere Forschung im Bereich der Margination war unterteilt in drei verschiedene Studien. Als erstes haben wir Marginationsmuster in den Kanälen mit unterschiedlichen Geometrie untersucht. Während einige Untersuchungen nahelegen, dass Margination in den Zonen mit niedrigsten Scherraten auftritt, konnten wir zeigen, dass steife Partikel zu den Zonen marginieren, die am ärmsten an roten Blutzellen sind. Dies untermauert die Idee, dass Margination von der Verteilung der roten Blutzellen beeinflusst ist. Jedoch konnten wir auch zeigen, dass im dreidimensionalen Fluss in manchen Fällen auch steife Zellen in einer Gleichgewichtsposition entlang der Kanalachse vorkommen. Wir untersuchten die Abhängigkeit der Margination von der Distanz zum Kanaleingang. Wir schlussfolgerten hieraus, dass, um ein voll entwickeltes Marginationsprofil zu erhalten, die Zellen größere Strecken zurücklegen müssen als typischerweise in der Mikrozirkulation anzutreffen sind. Das bedeutet, dass andere Mechanismen als Steifigkeitskontrast für die Margination verantwortlich sind. Wir haben entdeckt, dass die Sättigungsquote der Margination mit wachsendem Hämatokrit steigt, was zusätzlich die Idee der Margination als durch Kollisionen verursachtes Phänomen stärkt. Unsere Untersuchungen der Margination als Funktion der Fließgeschwindigkeit hat zu zwei interessanten Beobachtungen geführt. Zum einen fanden wir heraus, dass es einen optimalen Bereich der Hämatokritwerte gibt, die zu den höchsten Marginationsquoten führten. Zum anderen konnten wir schlussfolgern, dass die Abhängigkeit der Margination von der Fließrate nichtmonoton ist.

Diese Arbeit eröffnet zahlreiche Perspektiven für zukünftige Forschungsprojekte. Unsere Technik zur Analyse der Formen könnte auf Sichelzellen angewandt werden. Dies könnte es erlauben, Korrelationen zwischen Subpopulationen bestimmter Formen und entsprechender Schwere der Krankheit zu finden. Der nächste logische Schritt in Marginationsstudien sollte die Abhängigkeit der Margination von der Zellsteifigkeit sein. Mehrere Methoden bieten eine Möglichkeit, um den Steifigkeitskontrast zwischen Marginationzellen und normalen roten Blutzellen zu beeinflussen. Mit einem Modellexperiment, das in dieser Arbeit entwickelt wurde, kann die Margination als Funktion dieses Steifigkeitskontrasts untersucht werden.

Unsere experimentelle Methode enthüllt einige interessante Entdeckungen vom Standpunkt der Physik der Suspensionen. Es erlaubt, den Parameterbereich von stark deformierbaren Partikeln zu untersuchen. Durch Variation der Konzentration steifer Partikel ist es möglich, die räumliche Konfiguration zweier Populationen im Kanal oder Couette-Fluss zu untersuchen. Eine Limitierung solcher Experimente ist die fehlende Variabilität der Größe der roten Blutzellen. Dies würde die Verwendung von künstlichen Kapselsuspensionen erfordern.

Bibliography

- [] <https://www.brukerafmprobes.com/p-3444-mlct.aspx> (cit. on p. 37).
- [Aar+88] P A Aarts, S A van den Broek, G W Prins, et al. “Blood platelets are concentrated near the wall and red blood cells, in the center in flowing blood.” In: *Arteriosclerosis, Thrombosis, and Vascular Biology* 8.6 (1988), pp. 819–824 (cit. on p. 83).
- [ALV02] Manouk Abkarian, Colette Lartigue, and Annie Viallat. “Tank Treading and Unbinding of Deformable Vesicles in Shear Flow: Determination of the Lift Force”. In: *Phys. Rev. Lett.* 88 (6 2002), p. 068103. DOI: [10.1103/PhysRevLett.88.068103](https://doi.org/10.1103/PhysRevLett.88.068103). URL: <https://link.aps.org/doi/10.1103/PhysRevLett.88.068103> (cit. on p. 22).
- [Ala+13] Amr Alaarg, Raymond Schiffelers, Wouter van Solinge, et al. “Red blood cell vesiculation in hereditary hemolytic anemia”. In: *Frontiers in Physiology* 4 (2013), p. 365. ISSN: 1664-042X. DOI: [10.3389/fphys.2013.00365](https://doi.org/10.3389/fphys.2013.00365). URL: <https://www.frontiersin.org/article/10.3389/fphys.2013.00365> (cit. on p. 57).
- [AHS95] R. Alon, D. A. Hammer, and T. A. Springer. “Lifetime of the P-selectin-carbohydrate bond and its response to tensile force in hydrodynamic flow”. In: *Nature* 374 (1995), pp. 539–542 (cit. on p. 22).
- [Alv+15] Ofelia Alvarez, Naomi S. Montague, Marta Marin, et al. “Quantification of Sick Cells in the Peripheral Smear as a Marker of Disease Severity”. In: *Fetal and Pediatric Pathology* 34.3 (2015). PMID: 25517885, pp. 149–154. DOI: [10.3109/15513815.2014.987937](https://doi.org/10.3109/15513815.2014.987937). eprint: <https://doi.org/10.3109/15513815.2014.987937>. URL: <https://doi.org/10.3109/15513815.2014.987937> (cit. on p. 6).
- [Anc+17] Thomas J Anchordoquy, Yechezkel Barenholz, Diana Boraschi, et al. “Mechanisms and Barriers in Cancer Nanomedicine: Addressing Challenges, Looking for Solutions”. In: *ACS nano* 11.1 (Jan. 2017), pp. 12–18. ISSN: 1936-0851. DOI: [10.1021/acsnano.6b08244](https://doi.org/10.1021/acsnano.6b08244). URL: <http://europepmc.org/articles/PMC5542883> (cit. on p. 24).
- [AM00] Ulrich H. von Andrian and Charles R. Mackay. “T-Cell Function and Migration — Two Sides of the Same Coin”. In: *New England Journal of Medicine* 343.14 (2000). PMID: 11018170, pp. 1020–1034. DOI: [10.1056/NEJM200010053431407](https://doi.org/10.1056/NEJM200010053431407). eprint: <http://dx.doi.org/10.1056/NEJM200010053431407>. URL: <http://dx.doi.org/10.1056/NEJM200010053431407> (cit. on p. 23).
- [BK80] U. Bagge and R. Karlson. “Maintenance of White Blood Cell Margination at the Passage through Small Venular Junctions”. In: *Microvasc Res* 20 (1980), pp. 92–95 (cit. on p. 22).

- [BE03] Ingolf Bernhardt and J. Clive Ellory. “Red Cell Membrane Transport in Health and Disease”. In: Springer, Berlin, Heidelberg, 2003. ISBN: 9783642079207. DOI: [10.1007/978-3-662-05181-8](https://doi.org/10.1007/978-3-662-05181-8). URL: <https://doi.org/10.1007/978-3-662-05181-8> (cit. on p. 5).
- [BWL73] Marcel Bessis, Robert Weed. I., and Pierre Leblond F. “Red cell shape. Physiology, pathology, ultrastructure”. In: Springer Verlag New York, 1973 (cit. on p. 6).
- [BRG95] D. C. Betticher, W. H. Reinhart, and J. Geiser. “Effect of RBC shape and deformability on pulmonary O₂ diffusing capacity and resistance to flow in rabbit lungs”. In: *Journal of Applied Physiology* 78.3 (1995). PMID: 7775318, pp. 778–783. DOI: [10.1152/jappl.1995.78.3.778](https://doi.org/10.1152/jappl.1995.78.3.778). eprint: <https://doi.org/10.1152/jappl.1995.78.3.778>. URL: <https://doi.org/10.1152/jappl.1995.78.3.778> (cit. on p. 7).
- [Bet+09] Timo Betz, Martin Lenz, Jean-François Joanny, et al. “ATP-dependent mechanics of red blood cells”. In: *Proceedings of the National Academy of Sciences* 106.36 (2009), pp. 15320–15325. ISSN: 0027-8424. DOI: [10.1073/pnas.0904614106](https://doi.org/10.1073/pnas.0904614106). eprint: <http://www.pnas.org/content/106/36/15320.full.pdf>. URL: <http://www.pnas.org/content/106/36/15320> (cit. on p. 9).
- [BQG86] G. Binnig, C. F. Quate, and Ch. Gerber. “Atomic Force Microscope”. In: *Phys. Rev. Lett.* 56 (9 Mar. 1986), pp. 930–933. DOI: [10.1103/PhysRevLett.56.930](https://doi.org/10.1103/PhysRevLett.56.930). URL: <https://link.aps.org/doi/10.1103/PhysRevLett.56.930> (cit. on p. 35).
- [BGK10] Z. I. Botev, J. F. Grotowski, and D. P. Kroese. “Kernel density estimation via diffusion”. In: *Ann. Statist.* 38.5 (Oct. 2010), pp. 2916–2957. DOI: [10.1214/10-AOS799](https://doi.org/10.1214/10-AOS799). URL: <https://doi.org/10.1214/10-AOS799> (cit. on pp. 78, 90).
- [BR04] P.C. Braga and D. Ricci. *Atomic Force Microscopy: Biomedical Methods and Applications*. Biomed Protocols. Humana Press, 2004. ISBN: 9781592596478. URL: <https://books.google.de/books?id=Kd0tR6j5RucC> (cit. on pp. 35, 36).
- [Bru+13] M. Brust, C. Schaefer, R. Doerr, et al. “Rheology of Human Blood Plasma: Viscoelastic Versus Newtonian Behavior”. In: *Phys. Rev. Lett.* 110 (7 Feb. 2013), p. 078305. DOI: [10.1103/PhysRevLett.110.078305](https://doi.org/10.1103/PhysRevLett.110.078305). URL: <https://link.aps.org/doi/10.1103/PhysRevLett.110.078305> (cit. on p. 11).
- [BCK05] H.-J. Butt, B. Cappella, and M. Kappl. “Force measurements with the atomic force microscope: Technique, interpretation and applications”. In: *Surface Science Reports* 59 (Oct. 2005), pp. 1–152. DOI: [10.1016/j.surfrep.2005.08.003](https://doi.org/10.1016/j.surfrep.2005.08.003) (cit. on pp. 38, 39).

- [BW17] James R. Byrnes and Alisa S. Wolberg. “Red blood cells in thrombosis”. In: *Blood* 130.16 (2017), pp. 1795–1799. ISSN: 0006-4971. DOI: [10.1182/blood-2017-03-745349](https://doi.org/10.1182/blood-2017-03-745349). eprint: <http://www.bloodjournal.org/content/130/16/1795.full.pdf>. URL: <http://www.bloodjournal.org/content/130/16/1795> (cit. on p. 6).
- [Can70] P.B. Canham. “The minimum energy of bending as a possible explanation of the biconcave shape of the human red blood cell”. In: *Journal of Theoretical Biology* 26.1 (1970), pp. 61–81. ISSN: 0022-5193. DOI: [https://doi.org/10.1016/S0022-5193\(70\)80032-7](https://doi.org/10.1016/S0022-5193(70)80032-7). URL: <http://www.sciencedirect.com/science/article/pii/S0022519370800327> (cit. on pp. 8, 9).
- [Car+16a] Erik J. Carboni, Brice H. Bognet, Grant M. Bouchillon, Andrea L. Kadilak, Leslie M. Shor, Michael D. Ward, and Anson. “Direct Tracking of Particles and Quantification of Margination in Blood Flow”. In: *Biophys. J.* 111 (2016), pp. 1487–1495 (cit. on p. 26).
- [Car+16b] Erik J. Carboni, Brice H. Bognet, Grant M. Bouchillon, Andrea L. Kadilak, Leslie M. Shor, Michael D. Ward, and Anson W.K. Ma. “Direct Tracking of Particles and Quantification of Margination in Blood Flow”. In: *Biophys. J.* 111.7 (2016), pp. 1487–1495 (cit. on pp. 24–26, 83).
- [CJ14] Erik Carboni and Katherine Tschudi and Jaewook Nam and Xiuling Lu and Anson W. K. Ma. “Particle Margination and Its Implications on Intravenous Anticancer Drug Delivery”. In: *AAPS PharmSciTech* 15.3 (2014), pp. 762–771 (cit. on pp. 24, 25).
- [Che+17] Yuanyuan Chen, Donghai Li, Yongjian Li, et al. “Margination of Stiffened Red Blood Cells Regulated By Vessel Geometry”. In: *Scientific Reports* volume 7 (Nov. 2017), p. 15253. DOI: [10.1038/s41598-017-15524-0](https://doi.org/10.1038/s41598-017-15524-0) (cit. on pp. 26, 74, 78).
- [CHE05] Garrott W. Christoph, James Hofrichter, and William A. Eaton. “Understanding the Shape of Sickled Red Cells”. In: *Biophysical Journal* 88.2 (2005), pp. 1371–1376. ISSN: 0006-3495. DOI: <https://doi.org/10.1529/biophysj.104.051250>. URL: <http://www.sciencedirect.com/science/article/pii/S0006349505732033> (cit. on p. 6).
- [Cia+15] Gabriele Ciasca, Massimiliano Papi, Simone Di Claudio, et al. “Mapping Viscoelastic properties of healthy and pathological red blood cells at the nanoscale level”. In: 7 (Sept. 2015) (cit. on p. 40).
- [Cra+17] Emanuela Fabiola Craparo, Rosa D’Apolito, Gaetano Giammona, et al. “Margination of Fluorescent Polylactic Acid–Polyaspartamide based Nanoparticles in Microcapillaries In Vitro: the Effect of Hematocrit and Pressure”. In: *Molecules* 22.11 (2017). ISSN: 1420-3049. DOI: [10.3390/molecules22111845](https://doi.org/10.3390/molecules22111845). URL: <http://www.mdpi.com/1420-3049/22/11/1845> (cit. on p. 26).

- [Del95] Jean Delaunay. “Genetic disorders of the red cell membranes”. In: *FEBS Letters* 369.1 (1995), pp. 34–37. ISSN: 0014-5793. DOI: [https://doi.org/10.1016/0014-5793\(95\)00460-Q](https://doi.org/10.1016/0014-5793(95)00460-Q). URL: <http://www.sciencedirect.com/science/article/pii/S001457939500460Q> (cit. on p. 6).
- [Del04] Jean Delaunay. “The hereditary stomatocytoses: genetic disorders of the red cell membrane permeability to monovalent cations”. In: *Seminars in Hematology* 41.2 (2004). Erythrocyte Membrane Proteins and Their Diseases, pp. 165–172. ISSN: 0037-1963. DOI: <https://doi.org/10.1053/j.seminhematol.2004.02.005>. URL: <http://www.sciencedirect.com/science/article/pii/S0037196304000332> (cit. on p. 6).
- [DD90] Claude Desjardins and Brian R. Duling. “Heparinase treatment suggests a role for the endothelial cell glycocalyx in regulation of capillary hematocrit.” In: *Am J Physiol.* 258 (1990), H647–54 (cit. on p. 12).
- [Di +09] Dino Di Carlo, Jon F. Edd, Katherine J. Humphry, et al. “Particle Segregation and Dynamics in Confined Flows”. In: *Phys. Rev. Lett.* 102 (9 Mar. 2009), p. 094503. DOI: [10.1103/PhysRevLett.102.094503](https://doi.org/10.1103/PhysRevLett.102.094503). URL: <https://link.aps.org/doi/10.1103/PhysRevLett.102.094503> (cit. on p. 21).
- [Die+10a] Monica Diez-Silva, Ming Dao, Jongyoon Han, et al. “Shape and Biomechanical Characteristics of Human Red Blood Cells in Health and Disease”. In: *MRS Bulletin* 35.5 (2010), pp. 382–388. DOI: [10.1557/mrs2010.571](https://doi.org/10.1557/mrs2010.571) (cit. on p. 6).
- [Die+10b] Monica Diez-Silva, Ming Dao, Jongyoon Han, et al. “Shape and Biomechanical Characteristics of Human Red Blood Cells in Health and Disease”. In: *MRS Bulletin* 35.5 (2010), pp. 382–388. DOI: [10.1557/mrs2010.571](https://doi.org/10.1557/mrs2010.571) (cit. on p. 8).
- [Dim+02] Emiliós K. Dimitriadis, Ferenc Horkay, Julia Maresca, et al. “Determination of Elastic Moduli of Thin Layers of Soft Material Using the Atomic Force Microscope”. In: *Biophysical Journal* 82.5 (2002), pp. 2798–2810. ISSN: 0006-3495. DOI: [https://doi.org/10.1016/S0006-3495\(02\)75620-8](https://doi.org/10.1016/S0006-3495(02)75620-8). URL: <http://www.sciencedirect.com/science/article/pii/S0006349502756208> (cit. on p. 53).
- [DCS92] C. Dong, R.S. Chadwick, and A.N. Schechter. “Influence of sickle hemoglobin polymerization and membrane properties on deformability of sickle erythrocytes in the microcirculation”. In: *Biophysical Journal* 63.3 (1992), pp. 774–783. ISSN: 0006-3495. DOI: [https://doi.org/10.1016/S0006-3495\(92\)81655-7](https://doi.org/10.1016/S0006-3495(92)81655-7). URL: <http://www.sciencedirect.com/science/article/pii/S0006349592816557> (cit. on p. 57).
- [Dos+10] Nishit Doshi, Balabhaskar Prabhakarpanthian, Angela Rea-Ramsey, et al. “Flow and adhesion of drug carriers in blood vessels depend on their shape:

- A study using model synthetic microvascular networks”. In: *J. Control Release* 146.2 (2010), pp. 196–200 (cit. on p. 25).
- [DSB13] Alexey Dosovitskiy, Jost Tobias Springenberg, and Thomas Brox. “Unsupervised feature learning by augmenting single images”. In: *CoRR abs/1312.5242* (2013). arXiv: 1312.5242. URL: <http://arxiv.org/abs/1312.5242> (cit. on p. 60).
- [Du+15] E Du, Monica Diez-Silva, Gregory J. Kato, et al. “Kinetics of sickle cell biorheology and implications for painful vasoocclusive crisis”. In: *Proceedings of the National Academy of Sciences* 112.5 (2015), pp. 1422–1427. DOI: 10.1073/pnas.1424111112. eprint: <http://www.pnas.org/content/112/5/1422.full.pdf>. URL: <http://www.pnas.org/content/112/5/1422.abstract> (cit. on p. 57).
- [Duf+98] David C. Duffy, J. Cooper McDonald, Olivier J. A. Schueller, et al. “Rapid Prototyping of Microfluidic Systems in Poly(dimethylsiloxane)”. In: *Analytical Chemistry* 70.23 (1998). PMID: 21644679, pp. 4974–4984. DOI: 10.1021/ac980656z. eprint: <http://dx.doi.org/10.1021/ac980656z>. URL: <http://dx.doi.org/10.1021/ac980656z> (cit. on p. 29).
- [Dul+06] Ida Dulińska-Molak, Marta Targosz, Wojciech Strojny, et al. “Stiffness of normal and pathological erythrocytes studied by means of atomic force microscopy”. In: 66 (Apr. 2006), pp. 1–11 (cit. on p. 53).
- [Eva+17] Arthur A. Evans, Basanta Bhaduri, Gabriel Popescu, et al. “Geometric localization of thermal fluctuations in red blood cells”. In: *Proceedings of the National Academy of Sciences* (2017). ISSN: 0027-8424. DOI: 10.1073/pnas.1613204114. eprint: <http://www.pnas.org/content/early/2017/02/22/1613204114.full.pdf>. URL: <http://www.pnas.org/content/early/2017/02/22/1613204114> (cit. on p. 8).
- [EJC15] Randy H. Ewoldt, Michael T. Johnston, and Lucas M. Caretta. “Experimental Challenges of Shear Rheology: How to Avoid Bad Data”. In: *Complex Fluids in Biological Systems: Experiment, Theory, and Computation*. Ed. by Saverio E. Spagnolie. New York, NY: Springer New York, 2015, pp. 207–241. ISBN: 978-1-4939-2065-5. DOI: 10.1007/978-1-4939-2065-5_6. URL: https://doi.org/10.1007/978-1-4939-2065-5_6 (cit. on p. 115).
- [FL31] R. Fåhræus and T. Lindqvist. “The viscosity of the blood in narrow capillary tubes.” In: *Am J Physiol.* 96 (1931), pp. 562–568 (cit. on p. 17).
- [Fåh29] Robin Fåhræus. “THE SUSPENSION STABILITY OF THE BLOOD”. In: *Physiological Reviews* 9.2 (1929), pp. 241–274. eprint: <http://physrev.physiology.org/content/9/2/241.full.pdf>. URL: <http://physrev.physiology.org/content/9/2/241> (cit. on p. 16).

- [Fal+18] Giacomo Falcucci, Simone Melchionna, Paolo Decuzzi, et al. “Simulating Soft-Sphere Margination in Arterioles and Venules”. In: (Jan. 2018) (cit. on p. 78).
- [FFG12] Dmitry A. Fedosov, Julia Fornleitner, and Gerhard Gompper. “Margination of White Blood Cells in Microcapillary Flow”. In: *Phys. Rev. Lett.* 108 (2 2012), p. 028104 (cit. on pp. 26, 78, 84).
- [FG14] Dmitry A. Fedosov and Gerhard Gompper. “White blood cell margination in microcirculation”. In: *Soft Matter* 10 (17 2014), pp. 2961–2970. DOI: [10.1039/C3SM52860J](https://doi.org/10.1039/C3SM52860J). URL: <http://dx.doi.org/10.1039/C3SM52860J> (cit. on p. 24).
- [FDS14] Dmitry Fedosov, M. Dao, and G.E. Karniadakis and S. Suresh. “Computational biorheology of human blood flow in health and disease”. In: *Ann. Biomed. Eng.* 42.2 (2014), pp. 368–387 (cit. on p. 25).
- [Fer05] M. Ferrari. “Cancer nanotechnology: opportunities and challenges”. In: *Nat. Rev. Cancer* 5 (2005), pp. 161–171 (cit. on p. 24).
- [Fit+15] Sean Fitzgibbon, Andrew P. Spann, Qin M. Qi, et al. “In Vitro Measurement of Particle Margination in the Microchannel Flow: Effect of Varying Hematocrit”. In: *Biophys. J.* 108 (2015), pp. 2601–2608 (cit. on p. 26).
- [For18] Amir Forouzandehmehr Mohamadamin and Shamloo. “Margination and adhesion of micro- and nanoparticles in the coronary circulation: a step towards optimised drug carrier design”. In: *Biomechanics and Modeling in Mechanobiology* 17.1 (Feb. 2018), pp. 205–221. ISSN: 1617-7940. DOI: [10.1007/s10237-017-0955-x](https://doi.org/10.1007/s10237-017-0955-x). URL: <https://doi.org/10.1007/s10237-017-0955-x%22> (cit. on pp. 25, 26).
- [Fre07] Jonathan B. Freund. “Leukocyte margination in a model microvessel.” In: *Phys. Fluids* 19 (2007), p. 023301 (cit. on pp. 26, 84).
- [GF14] Thomas M. Geislinger and Thomas Franke. “Hydrodynamic lift of vesicles and red blood cells in flow — from Fåhræus Lindqvist to microfluidic cell sorting”. In: *Advances in Colloid and Interface Science* 208 (2014). Special issue in honour of Wolfgang Helfrich, pp. 161–176. ISSN: 0001-8686. DOI: <https://doi.org/10.1016/j.cis.2014.03.002>. URL: <http://www.sciencedirect.com/science/article/pii/S000186861400102X> (cit. on p. 21).
- [Gen+08] F. Gentile, C. Chiappini, D. Fine, et al. “The effect of shape on the margination dynamics of non-neutrally buoyant particles in two-dimensional shear flows”. In: *J. Biomech* 41.10 (2008), pp. 2312–2318 (cit. on p. 25).

- [GCB67] A.J. Goldman, R.G. Cox, and H. Brenner. “Slow viscous motion of a sphere parallel to a plane wall—I Motion through a quiescent fluid”. In: *Chemical Engineering Science* 22.4 (1967), pp. 637–651. ISSN: 0009-2509. DOI: [https://doi.org/10.1016/0009-2509\(67\)80047-2](https://doi.org/10.1016/0009-2509(67)80047-2). URL: <http://www.sciencedirect.com/science/article/pii/0009250967800472> (cit. on p. 19).
- [GS84] H Goldsmith and S Spain. “Margination of leukocytes in blood flow through small tubes.” In: *Microvasc Res* 27 (2 1984), pp. 204–222 (cit. on p. 22).
- [Gre+96] R. Greger, U. Windhorst (auth.), Prof. Dr. Rainer Greger, et al. *Comprehensive Human Physiology: From Cellular Mechanisms to Integration*. 1st ed. Springer-Verlag Berlin Heidelberg, 1996. URL: <http://gen.lib.rus.ec/book/index.php?md5=af1db5756388be3488ea5d3dd4b2e94b> (cit. on p. 12).
- [GG17] A. Guckenberger and S. Gekle. “Theory and algorithms to compute Helfrich bending forces: a review”. In: *Journal of Physics Condensed Matter* 29.20, 203001 (Mar. 2017), p. 203001. DOI: [10.1088/1361-648X/aa6313](https://doi.org/10.1088/1361-648X/aa6313) (cit. on p. 9).
- [Gut+18] Mario Gutierrez, Margaret Fish B, Alexander Golinski W., et al. “Presence of Rigid Red Blood Cells in Blood Flow Interferes with the Vascular Wall Adhesion of Leukocytes”. In: *Langmuir* 34.6 (2018), pp. 2363–2372. DOI: [10.1021/acs.langmuir.7b03890](https://doi.org/10.1021/acs.langmuir.7b03890) (cit. on p. 26).
- [HR00] Vink Hans and Duling Brian R. “Capillary endothelial surface layer selectively reduces plasma solute distribution volume”. In: *American Journal of Physiology - Heart and Circulatory Physiology* 278.1 (2000), H285–H289. ISSN: 0363-6135. eprint: <http://ajpheart.physiology.org/content/278/1/H285.full.pdf>. URL: <http://ajpheart.physiology.org/content/278/1/H285> (cit. on p. 12).
- [Heb49] D.O. Hebb. *The organization of behavior: a neuropsychological theory*. A Wiley book in clinical psychology. Wiley, 1949. URL: <https://books.google.de/books?id=lKcaAAAAMAAJ> (cit. on p. 57).
- [Hel73] W. Helfrich. “Elastic Properties of Lipid Bilayers: Theory and Possible Experiments.” In: *Zeitschrift für Naturforschung C* 28 (1973), pp. 693–703 (cit. on pp. 9, 21).
- [Hel74] W. Helfrich. “Blocked lipid exchange in bilayers and its possible influence on the shape of vesicles”. In: *Zeitschrift für Naturforschung C*. 29 (9-10 1974), pp. 510–515. ISSN: 1865-7125. DOI: [10.1515/znc-1974-9-1010](https://doi.org/10.1515/znc-1974-9-1010) (cit. on p. 9).
- [HD99] Charmaine B. S. Henry and Brian R. Duling. “Permeation of the luminal capillary glycocalyx is determined by hyaluronan.” In: *Am J Physiol*. 277 (1999), H508–H514 (cit. on p. 12).

- [Her96] H Hertz. “Miscellaneous papers.” In: *London Macmillan* (1896), p. 146 (cit. on p. 39).
- [HL74] B. P. Ho and L. G. Leal. “Inertial migration of rigid spheres in two-dimensional unidirectional flows”. In: *Journal of Fluid Mechanics* 65.2 (1974), pp. 365–400. DOI: [10.1017/S0022112074001431](https://doi.org/10.1017/S0022112074001431) (cit. on p. 20).
- [Hou+10] Han Wei Hou, Ali Asgar S. Bhagat, Alvin Guo Lin Chong, et al. “Deformability based cell margination-A simple microfluidic design for malaria-infected erythrocyte separation”. In: *Lab Chip* 10 (19 2010), pp. 2605–2613 (cit. on p. 25).
- [Hwa+10] Sung Hwan Cho, Jessica M Godin, Chun-Hao Chen, et al. “Review Article: Recent advancements in optofluidic flow cytometer”. In: 4 (Dec. 2010), p. 43001 (cit. on p. 21).
- [Jaf+15] I. H. Jaffer, J. C. Fredenburgh, J. Hirsh, et al. “Medical device-induced thrombosis: what causes it and how can we prevent it?” In: *Journal of Thrombosis and Haemostasis* 13 (2015), S72–S81. ISSN: 1538-7836. DOI: [10.1111/jth.12961](https://doi.org/10.1111/jth.12961). URL: <http://dx.doi.org/10.1111/jth.12961> (cit. on p. 10).
- [JM09] Abhishek Jain and Lance L. Munn. “Determinants of Leukocyte Margination in Rectangular Microchannels”. In: *PLOS ONE* 4.9 (2009), pp. 1–8 (cit. on pp. 25, 84).
- [JS10] R. K. Jain and T. Stylianopoulos. “Delivering nanomedicine to solid tumors”. In: *Nat. Rev. Clin. Oncol.* 7 (2010), pp. 653–664 (cit. on p. 24).
- [KLJ14] Eric K Sackmann, Anna L Fulton, and David J Beebe. “The present and future role of microfluidics in biomedical research”. In: 507 (Mar. 2014), pp. 181–9 (cit. on p. 29).
- [KBM09] Badr Kaoui, George Biros, and Chaouqi Misbah. “Why Do Red Blood Cells Have Asymmetric Shapes Even in a Symmetric Flow?” In: *Phys. Rev. Lett.* 103 (18 Oct. 2009), p. 188101. DOI: [10.1103/PhysRevLett.103.188101](https://doi.org/10.1103/PhysRevLett.103.188101). URL: <https://link.aps.org/doi/10.1103/PhysRevLett.103.188101> (cit. on p. 21).
- [KLG63] A Karnis, H L. Goldsmith, and S G. Mason. “Axial Migration of Particles in Poiseuille Flow”. In: 200 (Sept. 1963), pp. 159–160 (cit. on p. 21).
- [Koh01] Teuvo Kohonen. *Self-Organizing Maps*. Berlin, Heidelberg: Springer Berlin Heidelberg, 2001. ISBN: 978-3-642-56927-2. DOI: [10.1007/978-3-642-56927-2](https://doi.org/10.1007/978-3-642-56927-2). URL: <https://doi.org/10.1007/978-3-642-56927-2> (cit. on p. 66).
- [Koh14] Teuvo Kohonen. *MATLAB Implementations and Applications of the Self-Organizing Map*. Helsinki, Finland: Unigrafia Oy, 2014. ISBN: 978-952-60-3678-6 (cit. on p. 66).

- [KK17] M. M. Krell and S. K. Kim. “Rotational data augmentation for electroencephalographic data”. In: *2017 39th Annual International Conference of the IEEE Engineering in Medicine and Biology Society (EMBC)*. July 2017, pp. 471–474. DOI: [10.1109/EMBC.2017.8036864](https://doi.org/10.1109/EMBC.2017.8036864) (cit. on p. 60).
- [Kri+17] Fabian L. Kriegel, Ralf Köhler, Jannike Bayat-Sarmadi, et al. “Cell shape characterization and classification with discrete Fourier transforms and self-organizing maps”. In: *Cytometry Part A* (2017), n/a–n/a. ISSN: 1552-4930. DOI: [10.1002/cyto.a.23279](https://doi.org/10.1002/cyto.a.23279). URL: <http://dx.doi.org/10.1002/cyto.a.23279> (cit. on p. 57).
- [Krü16] Timm Krüger. “Effect of tube diameter and capillary number on platelet margination and near-wall dynamics”. In: *Rheol Acta* 55.6 (2016), pp. 511–526 (cit. on p. 22).
- [KG12a] Amit Kumar and Michael D. Graham. “Margination and segregation in confined flows of blood and other multicomponent suspensions”. In: *Soft Matter* 8 (41 2012), pp. 10536–10548 (cit. on p. 24).
- [KG12b] Amit Kumar and Michael D. Graham. “Mechanism of Margination in Confined Flows of Blood and Other Multicomponent Suspensions”. In: *Phys. Rev. Lett.* 109 (10 2012), p. 108102 (cit. on p. 24).
- [Lan+16a] Luca Lanotte, Johannes Mauer, Simon Mendez, et al. “Red cells’ dynamic morphologies govern blood shear thinning under microcirculatory flow conditions”. In: *Proceedings of the National Academy of Sciences* 113.47 (2016), pp. 13289–13294. DOI: [10.1073/pnas.1608074113](https://doi.org/10.1073/pnas.1608074113). eprint: <http://www.pnas.org/content/113/47/13289.full.pdf>. URL: <http://www.pnas.org/content/113/47/13289.abstract> (cit. on p. 10).
- [Lan+16b] Luca Lanotte, Johannes Mauer, Simon Mendez, et al. “Red cells’ dynamic morphologies govern blood shear thinning under microcirculatory flow conditions”. In: *Proceedings of the National Academy of Sciences* 113.47 (2016), pp. 13289–13294. DOI: [10.1073/pnas.1608074113](https://doi.org/10.1073/pnas.1608074113). eprint: <http://www.pnas.org/content/113/47/13289.full.pdf>. URL: <http://www.pnas.org/content/113/47/13289.abstract> (cit. on pp. 57, 93).
- [LT95] K Ley and T F Tedder. “Leukocyte interactions with vascular endothelium. New insights into selectin-mediated attachment and rolling”. In: *J Immunol* 155 (1995), pp. 525–528 (cit. on p. 22).
- [Li+07] Ju Li, George Lykotrafitis, Ming Dao, et al. “Cytoskeletal dynamics of human erythrocyte”. In: *Proceedings of the National Academy of Sciences* 104.12 (2007), pp. 4937–4942. DOI: [10.1073/pnas.0700257104](https://doi.org/10.1073/pnas.0700257104). eprint: <http://www.pnas.org/content/104/12/4937.full.pdf>. URL: <http://www.pnas.org/content/104/12/4937.abstract> (cit. on p. 8).

- [LWM09] Gerald Lim H. W., Michael Wortis, and Ranjan Mukhopadhyay. “Red Blood Cell Shapes and Shape Transformations: Newtonian Mechanics of a Composite Membrane: Sections 2.5–2.8”. In: *Soft Matter*. Wiley-VCH Verlag GmbH & Co. KGaA, 2009, pp. 139–204. ISBN: 9783527623372. DOI: [10.1002/9783527623372.ch2b](https://doi.org/10.1002/9783527623372.ch2b). URL: <http://dx.doi.org/10.1002/9783527623372.ch2b> (cit. on p. 6).
- [Liu+18] Zixiang Liu, Yuanzheng Zhu, Rekha R. Rao, et al. “Nanoparticle Transport in Cellular Blood Flow”. In: (Jan. 2018) (cit. on p. 25).
- [LCL11] S. Lorthois, F. Cassot, and F. Lauwers. “Simulation study of brain blood flow regulation by intra-cortical arterioles in an anatomically accurate large human vascular network. Part II: Flow variations induced by global or localized modifications of arteriolar diameters”. In: *NeuroImage* 54.4 (2011), pp. 2840–2853. ISSN: 1053-8119. DOI: <https://doi.org/10.1016/j.neuroimage.2010.10.040>. URL: <http://www.sciencedirect.com/science/article/pii/S1053811910013327> (cit. on p. 13).
- [Lux16] Samuel E. Lux. “Anatomy of the red cell membrane skeleton: unanswered questions”. In: *Blood* 127.2 (2016), pp. 187–199. ISSN: 0006-4971. DOI: [10.1182/blood-2014-12-512772](https://doi.org/10.1182/blood-2014-12-512772). eprint: <http://www.bloodjournal.org/content/127/2/187.full.pdf>. URL: <http://www.bloodjournal.org/content/127/2/187> (cit. on p. 8).
- [Lyn90] E.C. Lynch. “Peripheral blood smear”. In: *Clinical Methods: The History, Physical, and Laboratory Examinations*. H.K. Walker, W.D. Hall & J.W. Hurst, 1990, pp. 732–734 (cit. on p. 6).
- [Mak+16] Asya Makhro, Rick Huisjes, Liesbeth P. Verhagen, et al. “Red Cell Properties after Different Modes of Blood Transportation”. In: *Frontiers in Physiology* 7 (2016), p. 288. ISSN: 1664-042X. DOI: [10.3389/fphys.2016.00288](https://doi.org/10.3389/fphys.2016.00288). URL: <https://www.frontiersin.org/article/10.3389/fphys.2016.00288> (cit. on p. 42).
- [Med14] Blausen.com staff Medical gallery of Blausen Medical. 2014. DOI: [10.15347/wjm/2014.010](https://doi.org/10.15347/wjm/2014.010). URL: https://commons.wikimedia.org/wiki/File:Blausen_0425_Formed_Elements.png (cit. on p. 6).
- [MKA16] Marmar Mehrabadi, David N. Ku, and Cyrus K. Aidun. “Effects of shear rate, confinement, and particle parameters on margination in blood flow”. In: *Phys. Rev. E* 93 (2 2016), p. 023109 (cit. on pp. 23, 24).
- [Mis12] Chaouqi Misbah. “Vesicles, capsules and red blood cells under flow”. In: *Journal of Physics: Conference Series* 392.1 (2012), p. 012005. URL: <http://stacks.iop.org/1742-6596/392/i=1/a=012005> (cit. on pp. 9, 10).
- [MFG14] Kathrin Müller, Dmitry A. Fedosov, and Gerhard Gompper. “Margination of micro- and nano-particles in blood flow and its effect on drug delivery”. In: *Sci. Rep.* 4.4871 (2014) (cit. on pp. 24, 25).

- [MFG16] Kathrin Müller, Dmitry A. Fedosov, and Gerhard Gompper. “Understanding particle margination in blood flow – A step toward optimized drug delivery systems”. In: *Med.Eng.Phys.* 38.1 (2016), pp. 2–10 (cit. on pp. 24–26, 84).
- [Mul50] L. J. Mullins. “Hemolysis and Related Phenomena. Eric Ponder”. In: *The Quarterly Review of Biology* 25.2 (1950), pp. 241–241. DOI: [10.1086/397649](https://doi.org/10.1086/397649). eprint: <https://doi.org/10.1086/397649>. URL: <https://doi.org/10.1086/397649> (cit. on p. 6).
- [Nam+13] Katawut Namdee, Alex J. Thompson, Phapanin Charoenphol, et al. “Margination Propensity of Vascular-Targeted Spheres from Blood Flow in a Microfluidic Model of Human Microvessels”. In: *Langmuir* 29.8 (2013), pp. 2530–2535 (cit. on pp. 25, 26, 84).
- [Nam+17] Bumseok Namgung, Yan Cheng Ng, Hwa Liang Leo, et al. “Near-Wall Migration Dynamics of Erythrocytes in Vivo: Effects of Cell Deformability and Arteriolar Bifurcation”. In: *Frontiers in Physiology* 8 (2017), p. 963. ISSN: 1664-042X. DOI: [10.3389/fphys.2017.00963](https://doi.org/10.3389/fphys.2017.00963). URL: <https://www.frontiersin.org/article/10.3389/fphys.2017.00963> (cit. on p. 26).
- [Pal67] A.A. Palmer. “Platelet and leukocytes skimming.” In: *Bibl. Anat.* 9 (1967), pp. 300–303 (cit. on p. 22).
- [Par+10] YongKeun Park, Catherine A. Best, Kamran Badizadegan, et al. “Measurement of red blood cell mechanics during morphological changes”. In: *Proceedings of the National Academy of Sciences* 107.15 (2010), pp. 6731–6736. DOI: [10.1073/pnas.0909533107](https://doi.org/10.1073/pnas.0909533107). eprint: <http://www.pnas.org/content/107/15/6731.full.pdf> (cit. on p. 57).
- [Pat96] Dan W. Patterson. *Artificial Neural Networks: Theory and Applications*. Prentice-Hall Series in Advanced Communications. Prentice Hall, 1996. ISBN: 9780132953535. URL: <https://books.google.de/books?id=tJokAQAIAAJ> (cit. on p. 57).
- [PL00] Mark J. Pearson and Herbert H. Lipowsky. “Influence of erythrocyte aggregation on leukocyte margination in postcapillary venules of rat mesentery.” In: *Am. J. Physiol.* 279 (2000), H1460–H1471 (cit. on p. 84).
- [PWS88] J. Perkkio, L.J. Wurzing, and H. Schmid-Schonbein. “Fåhræus-Vejlens effect: Margination of platelets and leukocytes in blood flow through branches”. In: *Microvasc Res* 50 (3 1988), pp. 357–364 (cit. on p. 22).
- [Phi66] R.H. Phibbs. “Distribution of leukocytes in blood flowing through arteries.” In: *Am. J. Physiol.* 210 (1966), pp. 919–925 (cit. on p. 22).
- [Poi30] Jean-Louis-Marie Poiseuille. “Recherches sur les causes du mouvement du sang dans les veins.” In: *J Physiol Exp Pathol.* 10 (1830), pp. 277–295 (cit. on p. 14).
- [PJ05] Aleksander S. Popel and Paul C. Johnson. “Microcirculation and Hemorheology”. In: *Annual Rev Fluid Mechanics* 37 (2005), pp. 43–69 (cit. on pp. 11, 13).

- [Pri+90] A R Pries, T W Secomb, P Gaehtgens, et al. "Blood flow in microvascular networks. Experiments and simulation." In: *Circulation Research* 67.4 (1990), pp. 826–834. ISSN: 0009-7330. DOI: [10.1161/01.RES.67.4.826](https://doi.org/10.1161/01.RES.67.4.826). eprint: <http://circres.ahajournals.org/content/67/4/826.full.pdf>. URL: <http://circres.ahajournals.org/content/67/4/826> (cit. on p. 17).
- [PSG00] A.R. Pries, T.W. Secomb, and P. Gaehtgens. "The endothelial surface layer". In: *Pflügers Archiv* 440 (2000), pp. 653–666 (cit. on p. 12).
- [PNG92] Axel R. Pries, D. Neuhaus, and P. Gaehtgens. "Blood viscosity in tube flow: dependence on diameter and hematocrit". In: *American Journal of Physiology-Heart and Circulatory Physiology* 263.6 (1992). PMID: 1481902, H1770–H1778. DOI: [10.1152/ajpheart.1992.263.6.H1770](https://doi.org/10.1152/ajpheart.1992.263.6.H1770). eprint: <https://doi.org/10.1152/ajpheart.1992.263.6.H1770>. URL: <https://doi.org/10.1152/ajpheart.1992.263.6.H1770> (cit. on pp. 17, 18).
- [Qui+17] S. Quint, A. F. Christ, A. Guckenberger, et al. "3D tomography of cells in micro-channels". In: *Applied Physics Letters* 111.10 (2017), p. 103701. DOI: [10.1063/1.4986392](https://doi.org/10.1063/1.4986392). eprint: <https://doi.org/10.1063/1.4986392>. URL: <https://doi.org/10.1063/1.4986392> (cit. on p. 57).
- [Rud10] Sergey V. Rudenko. "Erythrocyte morphological states, phases, transitions and trajectories". In: *Biochimica et Biophysica Acta (BBA) - Biomembranes* 1798.9 (2010), pp. 1767–1778. ISSN: 0005-2736. DOI: <https://doi.org/10.1016/j.bbamem.2010.05.010>. URL: <http://www.sciencedirect.com/science/article/pii/S0005273610001598> (cit. on p. 6).
- [Sch+80] Geert W. Schmid-Schönbein, Shunichi Usami, Richard Skalak, et al. "The interaction of leukocytes and erythrocytes in capillary and postcapillary vessels". In: *Microvasc Res* 19 (1 1980), pp. 45–70 (cit. on p. 22).
- [SS61] G. SEGRÉ and A. SILBERBERG. "Radial Particle Displacements in Poiseuille Flow of Suspensions". In: *Nature* 189 (1961). DOI: [10.1038/189209a0](https://doi.org/10.1038/189209a0). URL: <http://dx.doi.org/10.1038/189209a0> (cit. on p. 20).
- [She+05] Sergey S. Shevkoplyas, Tatsuro Yoshida, Lance L. Munn, et al. "Biomimetic Autoseparation of Leukocytes from Whole Blood in a Microfluidic Device". In: *Analytical Chemistry* 77.3 (2005). PMID: 15679363, pp. 933–937. DOI: [10.1021/ac049037i](https://doi.org/10.1021/ac049037i). URL: <http://dx.doi.org/10.1021/ac049037i> (cit. on p. 25).
- [Sne65] Ian N. Sneddon. "The relation between load and penetration in the axisymmetric boussinesq problem for a punch of arbitrary profile". In: *International Journal of Engineering Science* 3.1 (1965), pp. 47–57. ISSN: 0020-7225. DOI: [https://doi.org/10.1016/0020-7225\(65\)90019-4](https://doi.org/10.1016/0020-7225(65)90019-4). URL: <http://www.sciencedirect.com/science/article/pii/S0020722565900194> (cit. on p. 39).

- [Son07] Younggon Son. "Determination of shear viscosity and shear rate from pressure drop and flow rate relationship in a rectangular channel". In: *Polymer* 48 (2007), pp. 632–637 (cit. on p. 83).
- [TDL08] Ronald F. Tuma, Walter N. Durán, and Klaus Ley, eds. *Microcirculation (Second Edition)*. Second Edition. San Diego: Academic Press, 2008, pp. 931–949. ISBN: 978-0-12-374530-9. DOI: <https://doi.org/10.1016/B978-0-12-374530-9.00024-3>. URL: <https://www.sciencedirect.com/science/article/pii/B9780123745309000243> (cit. on pp. 10, 13–16).
- [Tan+13] Jifu Tan, Samar Shah, Antony Thomas, et al. "The influence of size, shape and vessel geometry on nanoparticle distribution". In: *Microfluid Nanofluidics* 14.1-2 (2013), pp. 77–87 (cit. on p. 25).
- [Tan+16] Shaoheng Tang, Chuanqi Peng, Jing Xu, et al. "Tailoring Renal Clearance and Tumor Targeting of Ultrasmall Metal Nanoparticles with Particle Density". In: *Angewandte Chemie International Edition* 55.52 (2016), pp. 16039–16043. ISSN: 1521-3773. DOI: [10.1002/anie.201609043](https://doi.org/10.1002/anie.201609043). URL: <http://dx.doi.org/10.1002/anie.201609043> (cit. on p. 25).
- [TM13] Marine Thiébaud and Chaouqi Misbah. "Rheology of a vesicle suspension with finite concentration: A numerical study". In: 88 (Dec. 2013), p. 062707 (cit. on p. 21).
- [TE87] A.W. Tilles and E.C. Eckstein. "Tile near-wall excess of platelet-sized particles in blood flow: Its dependence on hematocrit and wall shear rate." In: *Microvasc Res* 33 (1987), pp. 211–223 (cit. on p. 22).
- [Toy+11] Randall Toy, Elliott Hayden, Christopher Shoup, et al. "Effect of Particle Size, Density and Shape on Margination of Nanoparticles in Microcirculation". In: *Nanotechnology* 22 (11 2011) (cit. on pp. 24–26).
- [TL99] William T. Tse and Samuel E. Lux. "Red blood cell membrane disorders". In: *British Journal of Haematology* 104.1 (1999), pp. 2–13. ISSN: 1365-2141. DOI: [10.1111/j.1365-2141.1999.01130.x](https://doi.org/10.1111/j.1365-2141.1999.01130.x). URL: <http://dx.doi.org/10.1111/j.1365-2141.1999.01130.x> (cit. on p. 57).
- [Vej38] G Vejens. "The distribution of leukocytes in the vascular system." In: *Acta Pathol. Microbiol. Scand. (Suppl.)* 33 (1938), pp. 11–239 (cit. on p. 23).
- [Ves07] Pavel Vesely. "Handbook of Biological Confocal Microscopy, 3rd ed. By James B. Pawley, Editor. Springer Science + Business Media, LLC, New York (2006). ISBN 10: 0-387-25921-X; ISBN 13: 987-0387-25921-5; hardback; 28 + 985 pages". In: *Scanning* 29.3 (2007), pp. 91–91. ISSN: 1932-8745. DOI: [10.1002/sca.20059](https://doi.org/10.1002/sca.20059). URL: <http://dx.doi.org/10.1002/sca.20059> (cit. on p. 34).

- [VPM09] Petia M. Vlahovska, Thomas Podgorski, and Chaouqi Misbah. “Vesicles and red blood cells in flow: From individual dynamics to rheology”. In: *Comptes Rendus Physique* 10.8 (Nov. 2009), pp. 775–789. ISSN: 1631-0705. DOI: [10.1016/j.crhy.2009.10.001](https://doi.org/10.1016/j.crhy.2009.10.001) (cit. on p. 21).
- [WH04] Mulivor A. W. and Lipowsky H. H. “Inflammation- and ischemia-induced shedding of venular glycocalyx”. In: *American Journal of Physiology - Heart and Circulatory Physiology* 286.5 (2004), H1672–H1680. ISSN: 0363-6135. DOI: [10.1152/ajpheart.00832.2003](https://doi.org/10.1152/ajpheart.00832.2003). eprint: <http://ajpheart.physiology.org/content/286/5/H1672.full.pdf>. URL: <http://ajpheart.physiology.org/content/286/5/H1672> (cit. on p. 13).
- [Whi06] G.M. Whitesides. “The origins and the future of microfluidics”. In: 442 (Jan. 2006) (cit. on p. 29).
- [WKM98] H. W. Wu, T. Kuhn, and V. T. Moy. “Mechanical properties of L929 cells measured by atomic force microscopy: Effects of anticytoskeletal drugs and membrane crosslinking”. In: *Scanning* 20.5 (1998), pp. 389–397. ISSN: 1932-8745. DOI: [10.1002/sca.1998.4950200504](https://doi.org/10.1002/sca.1998.4950200504). URL: <http://dx.doi.org/10.1002/sca.1998.4950200504> (cit. on p. 38).
- [Wu+17] Wei-Tao Wu, Nadine Aubry, Mehrdad Massoudi, et al. “Transport of platelets induced by red blood cells based on mixture theory”. In: *International Journal of Engineering Science* 118 (2017), pp. 16–27 (cit. on pp. 10, 23).
- [XW98] Younan Xia and George M. Whitesides. “Soft Lithography”. In: *Angewandte Chemie International Edition* 37.5 (1998), pp. 550–575. ISSN: 1521-3773. DOI: [10.1002/\(SICI\)1521-3773\(19980316\)37:5<550::AID-ANIE550>3.0.CO;2-G](https://doi.org/10.1002/(SICI)1521-3773(19980316)37:5<550::AID-ANIE550>3.0.CO;2-G). URL: [http://dx.doi.org/10.1002/\(SICI\)1521-3773\(19980316\)37:5%3C550::AID-ANIE550%3E3.0.CO;2-G](http://dx.doi.org/10.1002/(SICI)1521-3773(19980316)37:5%3C550::AID-ANIE550%3E3.0.CO;2-G) (cit. on p. 29).
- [Xu+17] Mengjia Xu, Dimitrios P. Papageorgiou, Sabia Z. Abidi, et al. “A deep convolutional neural network for classification of red blood cells in sickle cell anemia”. In: *PLOS Computational Biology* 13.10 (Oct. 2017), pp. 1–27. DOI: [10.1371/journal.pcbi.1005746](https://doi.org/10.1371/journal.pcbi.1005746). URL: <https://doi.org/10.1371/journal.pcbi.1005746> (cit. on p. 57).
- [Yan+11] Xiaoxi Yang, Omid Forouzan, Jennie M. Burns, et al. “Traffic of leukocytes in microfluidic channels with rectangular and rounded cross-sections”. In: *Lab Chip* 11 (19 2011), pp. 3231–3240. DOI: [10.1039/C1LC20293F](https://doi.org/10.1039/C1LC20293F). URL: <http://dx.doi.org/10.1039/C1LC20293F> (cit. on p. 73).
- [Zha+16] Jun Zhang, Sheng Yan, Dan Yuan, et al. “Fundamentals and applications of inertial microfluidics: a review”. In: *Lab Chip* 16 (1 2016), pp. 10–34. DOI: [10.1039/C5LC01159K](https://doi.org/10.1039/C5LC01159K). URL: <http://dx.doi.org/10.1039/C5LC01159K> (cit. on p. 29).

- [ZSN12] Hong Zhao, Eric S. G. Shaqfeh, and Vivek Narsimhan. “Shear-induced particle migration and margination in a cellular suspension.” In: *Phys. Fluids* 24 (2012), p. 011902 (cit. on pp. [26](#), [84](#)).

Appendix

A. ANTON Paar MCR 702 rheometer low-torque resolution limit

The minimum torque is typically the most important limitation for soft biological systems (Ewoldt, Johnston, and Caretta 2015). We use it to define theoretical resolution limit of the rheometer MCR 702. The viscosity in terms of the measured quantities and conversion factors is defined from the steady shear stress τ_{21} and the steady shear-rate $\dot{\gamma}$ as:

$$\mu(\dot{\gamma}) = \frac{\tau_{21}(\dot{\gamma})}{\dot{\gamma}} \quad (.7)$$

The CC20 Taylor-Couette geometry used in rheological experiments in this work is depicted in the Fig. .17. In case of Taylor-Couette system, the measured quantity torque M is connected to the steady shear stress as:

$$\tau_{21} = \frac{1 + \delta^2}{2\delta} \cdot \frac{M}{2\pi L \cdot r_i^2 \cdot C_L} \quad (.8)$$

, where $\delta = 1.099$ is radius ratio, $L = 29.999mm$ is a gap length, $r_i = 10.001mm$ is a measuring bob radius and $C_L = 1.10$ is a end effect correction factor. We state the condition for acceptable data that measured torque is above some minimum limit, $M > M_{min}$. The minimal measurable torque $M_{min} = 1nNm$ is provided in ANTON Paar MCR 702 rheometer technical specifications. Consequently, the low-torque resolution limit is defined as:

$$\mu(\dot{\gamma}) > \frac{1}{\dot{\gamma}} \cdot \frac{1 + \delta^2}{2\delta} \cdot \frac{M_{min}}{2\pi L \cdot r_i^2 \cdot C_L} \quad (.9)$$

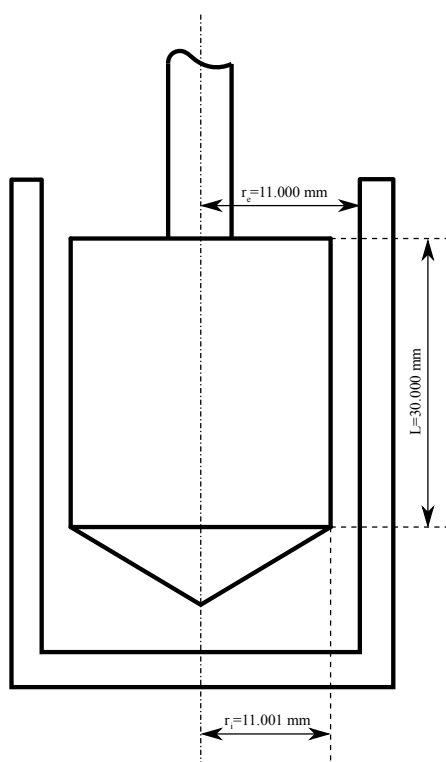


Figure .17. – Measuring system CC20